Ion beam induced damage in porphyrins

de Jong, M.P.

Award date:
1996

Ion beam induced damage in porphyrins

Michel de Jong

June 1996

VDF/NK 96-09

Cyclotron laboratory
Eindhoven University of Technology
P.O. Box 513
5600 MB Eindhoven
The Netherlands

Prof. dr. M.J.A. de Voigt
Dr. S.S. Klein
Drs. A.J.H. Maas

Abstract

In the Nuclear Physics Techniques group at Eindhoven University of Technology (EUT), various ion beam analysis techniques for materials research are practised. One of these techniques is Elastic Recoil Detection Analysis (ERDA), which is suitable for the profiling of light elements such as H, C and O.
The applicability of ERDA for the characterisation of organic materials is limited by ion beam induced damage. The electronic energy deposition by the impinging ions leads to molecular bond cleavage, which results in rearrangements of the molecular structure and the emission of small volatile molecules, especially H_2. Concerning the feasibility of ERDA for hydrogen quantification in organic materials, it is important to achieve insight in the process of hydrogen release and how this can be minimized by adjusting the irradiation conditions.
The hydrogen loss from porphyrins (organic solar cells) in ERDA experiments has been investigated using 2, 4, 7.6, and 12.1 MeV ^{4}He beams (EUT, cyclotron lab) and 4 and 10 MeV ^{12}C beams (Utrecht University, R. v.d. Graaff lab).
A theoretical model has been developed that adequately describes the measured hydrogen loss as a function of deposited ion fluence. According to this model, the released H_2 molecules are formed by the combination of free hydrogen radicals, which are produced through molecular bond cleavage in the ion "track". The process evolves by the mechanisms of direct combination, diffusion and trapping of radicals.
The "track" consists of a cylindrical region surrounding the ion's path, where secondary electrons distribute the energy deposited by the impinging ion. The width of this cylinder and the bond cleavage probability within are influenced by the ion's kinetic energy.

Contents

Abstract i

Contents ii

Chapter 1: Introduction 1

Chapter 2: RBS and ERDA 2

2.1 General description 2
2.2 Collision kinematics 6
2.2.1 Elastic collisions 6
2.2.2 Inelastic collisions 10
2.2.3 Nuclear reaction kinematics 11
2.3 Scattering and recoil cross sections 13
2.3.1 Definition of the differential cross section 13
2.3.2 The Rutherford window 15
2.3.3 Rutherford cross sections 15
2.3.4 Resonant scattering 17
2.4 Stopping of ions in matter 18
2.4.1 Stopping powers 18
2.4.2 Nuclear stopping 21
2.4.3 Electronic stopping 22
2.5 PSD ERDA and CERDA-TOF 24
2.5.1 The pulse shape discrimination (PSD) technique 24
2.5.2 CERDA-TOF 24

Chapter 3: Ion beam induced damage in solids 26

3.1 Damage creation mechanisms qualitatively 26
3.1.1 Atomic and nuclear collisions 26
3.2.1 Ion-electron interactions 27
3.2 Energy density distribution in the electronic system 28
3.3 Theoretical models on track formation 34
3.3.1 The Coulomb explosion model 34
3.3.2 Thermal spike theory 36
3.4 Ion irradiation damage in organic materials 38
3.5 Hydrogen loss model 39
3.5.1 Bond cleavage in the ion track 39
3.5.2 Hydrogen release 40
3.5.2.1 Direct combination of hydrogen radicals 41
3.5.2.2 Hydrogen molecules formed by diffusing radicals 43
3.5.2.3 Hydrogen content as a function of ion fluence 44

Chapter 4: Experiments 48

4.1 Sample composition 48
4.2 The cyclotron laboratory at EUT 49
4.2.1 Overview of the laboratory 49
4.2.2 The RBS/ERDA/CERDA-TOF setup 50
4.2.3 Hydrogen and carbon evolution measurements 51
4.3 The van der Graaff laboratory at UU 53
4.3.1 The magnetic spectrograph 53
4.3.2 Hydrogen loss experiments 54

Chapter 5: Results 55

5.1 Hydrogen loss from porphyrin layers under 2, 4, 7.6 and 12.1 MeV ^{4}He irradiation 55
5.1.1 Hydrogen-ERDA measurements 55
5.1.2 Simultaneous RBS experiments 60
5.1.3 The normalization procedure and calculation of the ion fluence 65
5.1.4 The hydrogen contents as a function of ion fluence 66
5.1.5 Background subtraction 76
5.1.6 The background in the 12.1 MeV ^{4}He H-ERDA experiments 77
5.2 Possible carbon loss from porphyrin layers subjected to 4 and 12.1 MeV ^{4}He beams 82
5.3 Hydrogen loss induced by 4 and 10 MeV ^{12}C bombardment 85
5.4 Hydrogen loss versus detection sensitivity 87

Chapter 6: Conclusions and recommendations 88

References 89

Appendix 1: Beamspot area measurements 92

Appendix 2: Beam current measurements 94

Appendix 3: Fitting with the hydrogen loss formula 96

CHAPTER 1: Introduction

Electrically conducting organic materials are being developed which have promising properties for a wide variety of applications. Among these applications are semiconductor devices, light emitting diodes and solar cells. Since exact knowledge of the composition of these organic materials is desired, the feasibility of ion beam analysis techniques for organic materials research is under investigation.

A limit is set by the structural modifications under ion irradiation, to which organic materials are especially sensitive. Such structural changes include scissioning of molecules, molecular bond rearrangements, crosslinking and loss of small volatile molecules. Optimal conditions have to be created to minimize the damaging effects while maintaining sufficient detection sensitivity. This work deals with ion beam induced damage in porphyrins, which are considered potential candidates for the fabrication of solar cells. The porphyrins were submitted to ion beam irradiation in Elastic Recoil Detection Analysis (ERDA) and Rutherford BackScattering (RBS) experiments, providing simultaneous analysis and damaging of the material. The loss of elements from the samples under ion bombardment could thus be monitored as a function of irradiation dose.

Hydrogen loss experiments were performed using ^{4}He beams with various energies at the Eindhoven University of Technology (EUT) cyclotron facility. Additional measurements with ^{12}C ions have been done at the Robert van der Graaff laboratory at Utrecht University (UU).

A theoretical hydrogen loss model has been developed in order to describe the experimental results. In chapter 2 the RBS and ERDA techniques are discussed. Chapter 3 contains a discussion on ion beam induced damage in solids, including the hydrogen loss model. The various experimental setups are described in chapter 4. Chapter 5 contains all experimental results and a comparison with the theoretical model. Finally, conclusions and recommendations are given in chapter 6.

CHAPTER 2: RBS and ERDA

Rutherford Backscattering Spectroscopy (RBS) and Elastic Recoil Detection Analysis (ERDA) are ion beam analysis techniques for materials research. The material to be investigated is probed by a beam of monoenergetic ions produced by a particle accelerator. These ions penetrate the surface of the material and collide with resident atoms. Detection of the particles which have participated in a collision provides a means for the profiling of elements present in the sample.
A general description of RBS and ERDA is presented in paragraph 2.1. The theoretical backgrounds of the techniques are given in paragraphs 2.2 to 2.4. Paragraph 2.5 contains a brief description of two specific ERD analysis techniques: PSD ERDA and CERDA-TOF.

2.1 General description

Ion scattering techniques rely on the kinetic energy transfer in a binary collision between the nuclei of an incident ion and a target atom (see paragraph 2.2). The amount of transferred energy depends on the mass ratio of the colliding nuclei and is maximal when the masses of the projectile and the target atom are equal. This mass ratio dependent energy transfer gives rise to two detection techniques:

- RBS, the detection of backscattered projectiles;
- ERDA, in which recoiling target nuclei are detected.

The kinetic energy of a detected particle not only depends on the energy transfer in the binary collision, but also on the depth at which the collision took place. This is due to the fact that a particle travelling through matter loses kinetic energy (see paragraph 2.4). The energy loss scales with the pathlength and follows a well behaved pattern. Hence, depth profiling of elements is possible with ion scattering techniques.
A typical setup of an RBS experiment is depicted schematically in figure 2.1.1.

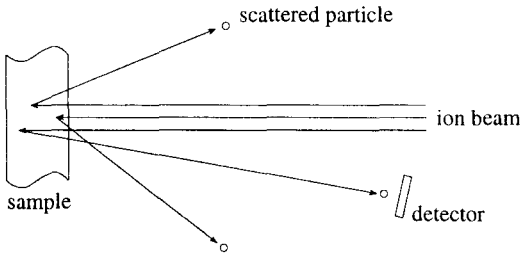

Figure 2.1.1: *schematic configuration of an RBS experiment.*

In general RBS is practiced using beams of light projectiles, such as protons or α particles. Projectiles scattered from the surface of the sample will have relatively high kinetic energy if they collided with a relatively heavy element (i.e. low energy transfer). Suppose that one is

interested in detecting a certain element (for instance an impurity) which is present in the surface region of a sample. If this element is relatively heavy (w.r.t. substrate elements) the corresponding peak in the energy spectrum of backscattered particles will appear at high energy, separate from the substrate background (see figure 2.1.2).

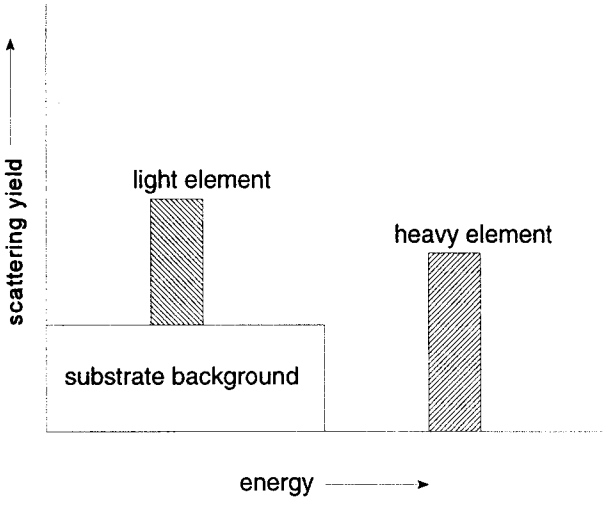

Figure 2.1.2: *schematic representation of an RBS spectrum of a sample in which a heavy and a light element are present in the surface region.*

However, a peak arising from a relatively light element will be masked by this background. Therefore, RBS is most suitable for the detection of heavy elements in a light matrix. For the profiling of light elements in a heavy matrix, ERDA will often prove to be more suitable.
In ERDA, one detects recoiled particles that have been ejected from the material by a collision with an impinging ion. As stated before, the kinetic energy of the recoils depends on the mass ratio μ of the collision partners. However, the same recoil energy results when μ is replaced by $1/\mu$. For example, O and H atoms recoiling after collisions with α particles will have the same kinetic energy at the same recoil angle.
When practicing ERD analysis, one must always discriminate between recoils and scattered beam particles. If the projectiles are heavier than the heaviest element present in the sample, there is a critical angle θ_{crit} for scattering: no beam particles can be scattered at an angle $\theta>\theta_{crit}$. The critical angle is given by $\theta_{crit}=\arcsin(m_2/m_1)$, where m_1 is the projectile mass and m_2 is the mass of the (heaviest) target atom. Detection of recoils alone can be accomplished by placing the detector at an angle greater than θ_{crit} (see figure 2.1.3).

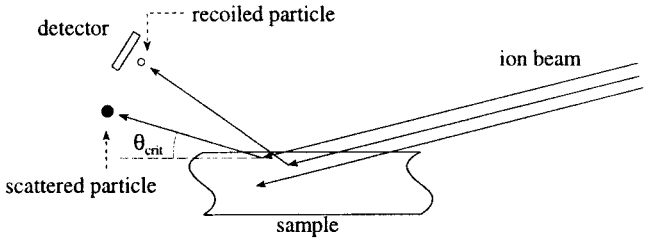

Figure 2.1.3: *when the beam particles are heavier than all elements in the sample, they cannot reach the detector when it is placed at an angle greater than* θ_{crit}

If the projectile mass is smaller than that of the heaviest element in the sample, scattered beam particles have to be discriminated from recoils in a different way. Several techniques have been developed to accomplish this.
When the recoils of interest are relatively light, a stopper foil placed in front of the detector is sufficient (see figure 2.1.4).

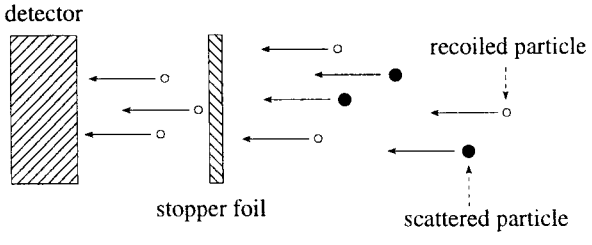

Figure 2.1.4: *the scattered beam particles are prevented from reaching the detector by a stopper foil.*

The heavy scattered beam particles are stopped in the foil, whereas the lighter recoils can pass through. Some examples of more sophisticated methods to establish the identity of the detected particles are:

- ΔE-E ERDA, in which a detected particle is labeled by two signals, from a thin ΔE and a conventional E detector respectively. The combination of these signals provides a way to identify the particle unambigiously.
- Pulse Shape Discrimination (PSD) ERDA. A special detector with a very thin sensitive layer is used which generates a pulse with properties that differ considerably for particles with different masses. A more detailed description of this technique is presented in

paragraph 2.5.1.

- Coincident ERD analysis (CERDA). In a collision between two particles, there is an angular correlation between the recoiling and scattered particle. Recoils can thus be identified by detecting both particles in coincidence, using two detectors placed at the appropriate angles. In paragraph 2.5.2, CERDA combined with a time-of-flight measurement (CERDA-TOF) is discussed.

By means of ERDA or RBS, the abundance of the various elements in a material can be calculated from the cross section σ for a given collision process, which determines the probability of a collision to occur (see paragraph 2.3).

In the following paragraphs of this chapter, the theoretical backgrounds of the RBS and ERDA techniques will be discussed step by step:

1. collision kinematics, providing a means to identify the various elements in the material;
2. scattering and recoil cross sections, from which the abundance of an element can be calculated;
3. energy loss of ions in solid matter, which is the key to depth resolution.

2.2 Collision kinematics

2.2.1 Elastic collisions

Classical kinematics of elastic collisions has been discussed extensively in literature, see for example [FEL86]. Therefore, only a brief outline is included in this text.
Consider a collision between a projectile m_1 with initial kinetic energy E_0 and a stationairy particle m_2 (see figure 2.2.1).

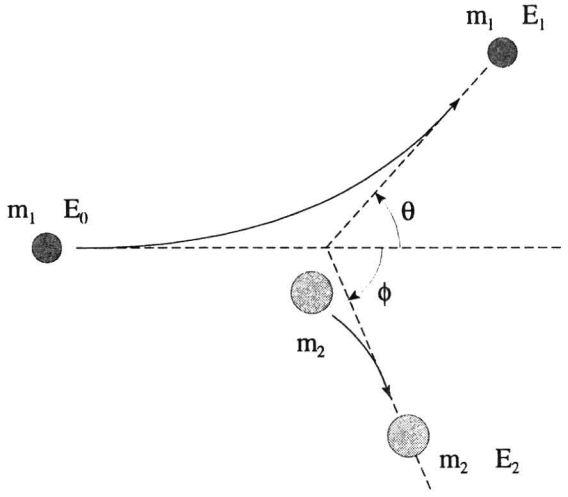

Figure 2.2.1: *a collision between two particles.*

The scattering and recoil angles are θ and ϕ respectively. The energy transfer from the projectile to the recoiled particle is described by the recoil kinematic factor $K_2=E_2/E_0$, where E_2 is the final kinetic energy of the recoiled particle. The kinematic factor $K_1=E_1/E_0$ indicates the energy fraction remaining to the scattered projectile.
The kinematic factors can easily be obtained from a calculation in center of mass (CM) coordinates (see figure 2.2.2).

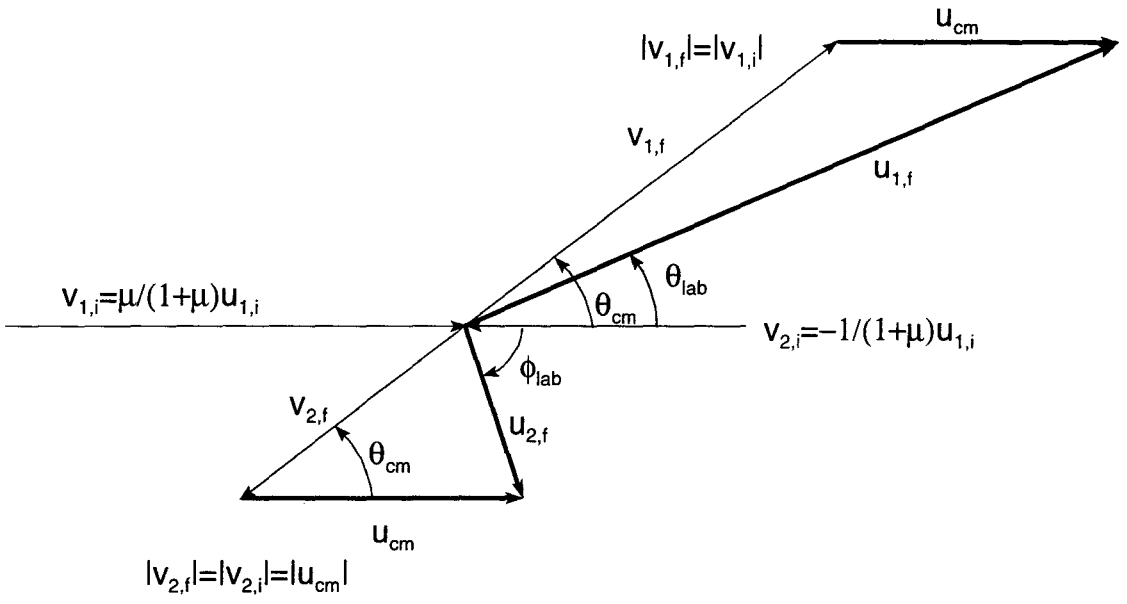

Figure 2.2.2: *vectordiagram of the velocities of the colliding particles. The symbols are explained in the text.*

The velocities of the particles in the CM system are represented by the thin vectors labeled with the letter v, the thick vectors with letter u are velocities in the laboratory frame. The subscripts 1 and 2 indicate the projectile and recoiling particle, respectively, the subscripts i and f represent initial and final velocities. In the CM frame, the velocity vectors of the colliding particles must allways point in opposite directions because the net momentum has to be zero. The collision does not change the length of these vectors due to conservation of mass and momentum. Furthermore, the velocity of the center of mass in the laboratory frame u_{cm} is constant and equal in magnitude to the initial velocity $v_{2,i}$ of the recoiling particle in the CM frame.
The initial velocities of the particles in the CM frame can be calculated from the initial velocity of the projectile in the laboratory frame and the mass ratio $\mu=m_2/m_1$ (see figure 2.2.2). We can now calculate the recoil kinematic factor by applying the cosine rule to the triangle formed by the vectors $v_{2,f}$, u_{cm} and $u_{2,f}$:

$$K_2 = \frac{\frac{1}{2}m_2\left|u_{2,f}\right|^2}{\frac{1}{2}m_1\left|u_{1,i}\right|^2} = \frac{\mu}{\left|u_{1,i}\right|^2}\left(\frac{2\left|u_{1,i}\right|^2}{(1+\mu)^2} - \frac{2\left|u_{1,i}\right|^2}{(1+\mu)^2}\cos\theta_{cm}\right) = \frac{2\mu}{(1+\mu)^2}(1-\cos\theta_{cm}) \qquad (2.2.1)$$

K_1 is obtained in a similar way:

$$K_1 = \frac{\mu^2+1+2\mu\cos\theta_{cm}}{(1+\mu)^2} \qquad (2.2.2)$$

These expressions can now be transformed to laboratory coordinates according to [BRA93]:

$$\tan\theta_{lab} = \frac{\mu \sin\theta_{cm}}{\mu\cos\theta_{cm} + 1} \Rightarrow$$

$$\cos\theta_{cm} = -\frac{\sin^2\theta_{lab}}{\mu} \pm \cos\theta_{lab}\sqrt{1-\left(\frac{\sin\theta_{lab}}{\mu}\right)^2} \qquad (2.2.3)$$

$$\phi_{lab} = \tfrac{1}{2}(\pi - \theta_{cm})$$

In laboratory coordinates, the recoil kinematic factor K_2 is given by:

$$K_2 = \frac{4\mu}{(1+\mu)^2}\cos^2\phi_{lab} \qquad (2.2.4)$$

Note that K_2 is symmetric under the substitution $\mu \rightarrow 1/\mu$, as was already mentioned in paragraph 2.1.
The kinematic factor for scattering K_1 in laboratory coordinates is:

$$K_1 = \left(\frac{\cos\theta_{lab} \pm \sqrt{\mu^2 - \sin^2\theta_{lab}}}{1+\mu}\right)^2 \qquad (2.2.5)$$

When the mass ratio μ is smaller than unity, there are two possible kinematic factors K_1 (corresponding to the $\pm$ sign) for the scattered particle at the same laboratory angle θ_{lab}. This can be understood by considering figure 2.2.3.

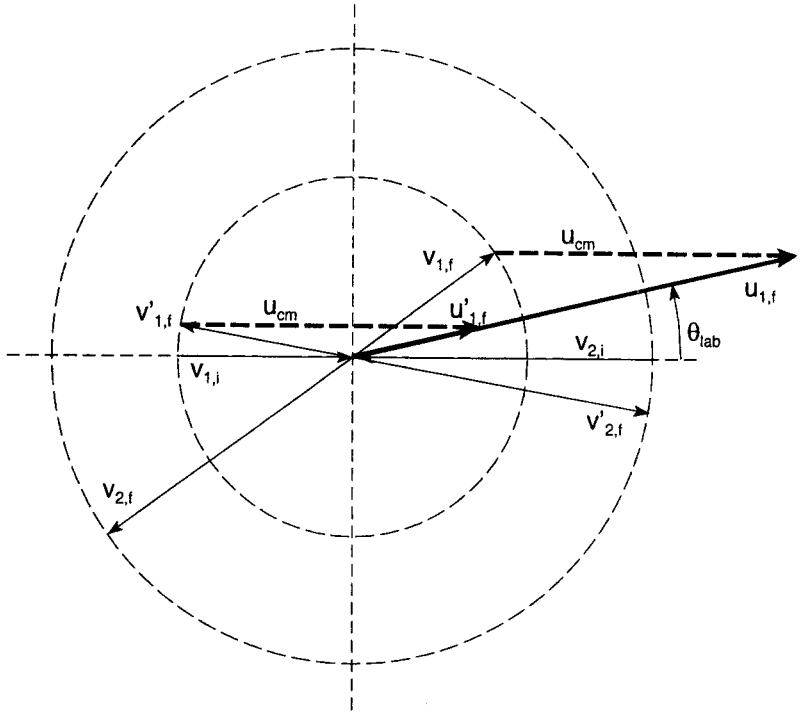

Figure 2.2.3: *when the mass ratio μ is smaller than 1 an elastically scattered particle can have two different energies at the same scattering angle. The symbols have the same meaning as those in figure 2.2.2.*

We see that when $\mu<1$ and hence $|v_1|<|u_{cm}|$, there are two possible vectors $u_{1,f}$ and $u'_{1,f}$ with the same laboratory scattering angle θ_{lab}. In this case there are two solutions for the kinematic factor K_1.

2.2.2 Inelastic collisions

A collision between an energetic ion and a target atom may leave the target nucleus in an excited state, which subsequently decays rapidly under emission of γ radiation. In such a collision, an extra amount (compared to the energy transfer in an elastic collision) of energy Q is absorbed by the recoiling particle. The excitation of a nucleus is an endoergic process, which means that Q must be positive.
The kinematic factors for inelastic collisions can be calculated from conservation of energy and momentum and are represented by:

$$K_{1i} = \frac{E_{1i}}{E_0} = \left(\frac{\cos\theta \pm \sqrt{\cos^2\theta - (1+\mu)(1-\mu+\mu Q/E_0)}}{(1+\mu)} \right)^2 \qquad (2.2.6)$$

for scattered particles and:

$$K_{2i} = \frac{E_{2i}}{E_0} = \frac{\mu}{(1+\mu)^2}\cos^2\varphi \left[1 \pm \sqrt{1 - \frac{(\mu+1)Q}{\mu E_0 \cos^2\varphi}} \right]^2 \qquad (2.2.7)$$

for recoils.
An inelastic collision is only possible when the kinetic energy in the center of mass frame exceeds Q, hence when $\mu E_0/(1+\mu) > Q$. Under this condition, the square root in equation 2.2.6 is real. There is only one solution for K_{1i} when $Q \leq (\mu-1)E_0/\mu$, since the numerator of equation 2.2.6, which represents the momentum of the scattered particle, must be positive. Similar to the elastic scattering case, the condition for two solutions is allways fulfilled when $\mu < 1$.
There are allways two possible recoil energies for inelastic scattering. This is due to the fact that when there is an inelastic loss Q, the final velocity of the recoiling particle in the CM frame is less than the velocity of the center of mass in laboratory coordinates.
A physically meaningful solution for K_{2i} with a positive argument of the square root is obtained when:

$$\frac{\mu E_0 \cos^2\varphi}{(\mu+1)} \geq Q \qquad (2.2.8)$$

which sets a limitation to the recoil angle φ.

2.2.3 Nuclear reaction kinematics

A collision between two particles can lead to a nuclear reaction. A nuclear reaction obeys conservation of nucleons, charge, mass-energy and momentum.
Consider the collision depicted in figure 2.2.4 which involves a nuclear reaction.

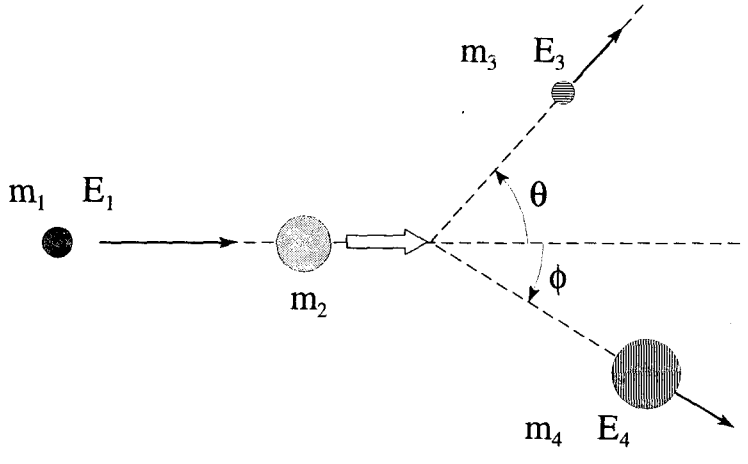

Figure 2.2.4: *a nuclear reaction triggered by the collision between projectile m_1 and target nucleus m_2.*

The projectile m_1 reacts with the target nucleus m_2 to give a residual nucleus m_4 and an emitted nuclear particle m_3. Sometimes no nuclear particle is emitted and the reaction produces γ radiation instead. The reaction can either be endoergic or exoergic with a Q value given by:

$$Q = (m_3 + m_4)c^2 - (m_1 + m_2)c^2 \qquad (2.2.9)$$

The residual nucleus can be left in an excited state, which increases the Q value by the excitation energy. The energy spectrum of the emitted particle is therefore characteristic of the possible excited states of the residual nucleus.

The energy E_3 of the emitted particle can be calculated by [FEL86]:

$$\sqrt{E_3} = A \pm \sqrt{A^2 + B} \tag{2.2.10}$$

$$A = \frac{\sqrt{m_1 m_3 E_1}}{m_3 + m_4}\cos\theta \qquad \text{and} \qquad B = \frac{E_1(m_4 - m_1) - m_4 Q}{m_3 + m_4}$$

These equations can be regarded as universal for any given scattering process, whether it is a nuclear reaction, an inelastic collision or an elastic scattering process. The equations for inelastic scattering result when m_3=m_1 and m_4=m_2. When Q is additionally set equal to zero, one finds the expressions for elastic collisions.

2.3 Scattering and recoil cross sections

2.3.1 Definition of the differential cross section

The cross section σ for a collision determines the probability of that particular collision to occur. Consider the scattering of a beam of particles through collisions with a certain element that is present with atomic coverage N at/cm^2. Suppose a detector is placed at an angle θ w.r.t. the beam. The probability P that a particle will be detected is:

$$P = \frac{d\sigma}{d\Omega}\Omega_{det}N \tag{2.3.1}$$

in which $d\sigma/d\Omega(\theta)$ is, by definition, the differential cross section and Ω_{det} is the solid angle occupied by the detector. When the differential cross section is known, the atomic coverage N of a certain element can be calculated from:

$$N = \frac{Y}{\frac{d\sigma}{d\Omega}\Omega_{det}M} \tag{2.3.2}$$

where Y is the detection yield (i.e. the number of detected particles) and M the number of projectiles.
Consider a collision between a projectile with mass m_1 and a target nucleus with mass m_2. The initial kinetic energy of the projectile is E_0. The scattering cross section can be calculated from the relation between the impact parameter b and the scattering angle θ which is determined by the force acting on the colliding particles during the collision. The impact parameter is defined as the perpendicular distance between the path of the projectile and the parallel line through the target nucleus. In the case of an elastic collision in a central potential V(r), the relation between b and the center of mass scattering angle θ_{cm} can be derived to be [ZIE85]:

$$\theta_{cm} = \pi - 2\int_{r_{min}}^{\infty} bdr\left[r^2\sqrt{1-\frac{V(r)}{E_{cm}}-\frac{b^2}{r^2}}\right]^{-1}, \qquad E_{cm} = \frac{m_2}{m_1+m_2}E_0 \tag{2.3.3}$$

where r is the distance between the two particles and E_{cm} is the initial center of mass energy. Equation 2.3.3 is known as the scattering integral.

Particles with impact parameters between b and db will be scattered into an angular region between θ_{cm} and $d\theta_{cm}$ (see figure 2.3.1). The impact parameters cover an area $2\pi bdb$, the angular region forms a solid angle $2\pi \sin\theta_{cm}\, d\theta_{cm}$. The proportionality constant is the differential cross section $d\sigma/d\Omega$:

$$\frac{d\sigma}{d\Omega} = -\frac{bdb}{\sin\theta_{cm} d\theta_{cm}} \qquad (2.3.4)$$

The minus sign indicates that a larger impact parameter results in less force acting on the particles and hence in a smaller scattering angle.

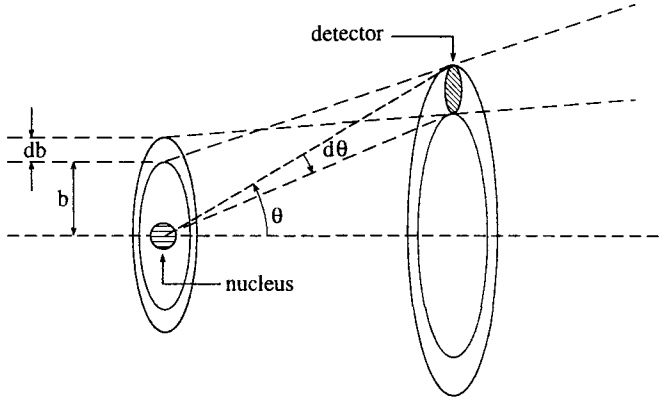

Figure 2.3.1: *particles that aproach the target nucleus between impact parameters b and b+db are scattered between angles θ and θ-dθ.*

In order to solve the scattering integral, we must now find an expression for the central potential V(r). Roughly, three energy regions have to be considered.

1. At low energy, the nuclei of the colliding ion and atom are screened by their electron clouds (or just the atom's electron cloud in the case of a fully stripped projectile). This leads to a modification of the Coulomb potential of the nuclear charge in the form of a screening function (see paragraph 2.4.2).
2. For high energies the Coulomb barrier can be overcome and nuclear forces will participate in the interaction between the colliding nuclei. This can lead to inelastic collisions (excited nuclei) or nuclear reactions.
3. In the intermediate region, Rutherford scattering takes place: a collision between two nuclei in the Coulomb potential.

We will solve equation 2.3.3 in the case of Rutherford scattering (see paragraph 2.3.3). The energy region for Rutherford scattering is defined next.

2.3.2 The Rutherford window

To determine the relevant energy region for a collision between two particles, we define a so-called Rutherford window in the following manner. Consider the distance of closest approach d for a collision in a Coulomb potential:

$$d = \frac{Z_1 Z_2 e^2}{4\pi\varepsilon_0 E} \tag{2.3.5}$$

in which E is the kinetic energy of the beam particle with atomic number Z_1 and Z_2 is the atomic number of the target atom. As a rule of thumb, we say that a collision falls in the Rutherford window when d is smaller than the K-shell radius r_K but considerably larger than the nuclear radius r_n [DAV93]:

$$r_K > d > 3r_n, \qquad r_K \approx \frac{0.5}{Z_2}, \qquad r_n \approx 1.4 \cdot 10^{-5} Z_2^{1/3} \tag{2.3.6}$$

where r_K and r_n are given in Å. The resulting lower and upper energy limits for Rutherford scattering are then given by $0.03 Z_1 Z_2^2$ keV and $0.3 Z_1 Z_2^{2/3}$ MeV respectively. In the case of a beam of α particles the lower limit for heavy elements (Pb and U) is about 0.5 MeV and the upper limit for light elements (C) is approximately 2 MeV. Hence, a 1-2 MeV α beam is suitable for the RBS analysis of most elements.

2.3.3 Rutherford cross sections

In the case of Rutherford scattering (Coulomb potential) the scattering integral can be solved analytically resulting in:

$$V(r) = \frac{Z_1 Z_2 e^2}{4\pi\varepsilon_0 r} \quad \rightarrow \quad b = \frac{Z_1 Z_2}{2E_{cm}} \frac{e^2}{4\pi\varepsilon_0} \cot\frac{\theta_{cm}}{2} \tag{2.3.7}$$

The Rutherford differential scattering cross section in center of mass coordinates is thus given by:

$$\frac{d\sigma}{d\Omega} = \left(\frac{Z_1 Z_2 e^2}{4\pi\varepsilon_0 4E_{cm}} \right)^2 \frac{1}{\sin^4\left(\frac{1}{2}\theta_{cm}\right)} \tag{2.3.8}$$

We now transform this equation to laboratory coordinates to give:

$$\frac{d\sigma}{d\Omega_{scat}} = \left(\frac{Z_1 Z_2 e^2}{4\pi\varepsilon_0 4E_0} \right)^2 \frac{4}{\sin^4\left(\theta_{lab}\right)} \frac{\left[\sqrt{1-\mu^{-2}\sin^2\theta_{lab}} + \cos\theta_{lab}\right]^2}{\sqrt{1-\mu^{-2}\sin^2\theta_{lab}}} \tag{2.3.9}$$

Comparing these two equations, it can be seen by applying standard goneometry that when μ is large ($m_2 >> m_1$), scattering in the laboratory frame becomes very similar to scattering in center of mass coordinates. The differential recoil cross section in the laboratory frame can be obtained in a similar way, by realizing that the amount of recoiled particles in a certain solid angle $d\Omega_{rec}$ must equal the amount of scattered particles in the solid angle $d\Omega_{scat}$:

$$\frac{d\sigma}{d\Omega_{rec}} = \left(\frac{Z_1 Z_2 e^2}{4\pi\varepsilon_0 4E_0}\right)^2 \frac{4(1+\mu)^2}{\mu^2 \cos^3 \varphi_{lab}} \qquad (2.3.10)$$

The scattering cross section σ can also be given in terms of an energy transfer T by Thompson's formula [GOL93]:

$$T = \frac{4m_1 m_2}{(m_1 + m_2)^2} E_0 \sin^2 \frac{\theta_{cm}}{2}$$

$$d\sigma = 2\pi b db = -\pi \left(\frac{Z_1 Z_2 e^2}{4\pi\varepsilon_0}\right)^2 \left(\frac{1}{2E_{cm}}\right)^2 \frac{\cos\left(\frac{1}{2}\theta_{cm}\right)}{\sin^3\left(\frac{1}{2}\theta_{cm}\right)} d\theta$$

$$dT = \frac{4m_1 m_2}{(m_1 + m_2)^2} E_0 \sin\left(\tfrac{1}{2}\theta_{cm}\right)\cos\left(\tfrac{1}{2}\theta_{cm}\right) d\theta_{cm} \qquad (2.3.11)$$

$$d\sigma = \pi \left(\frac{Z_1 Z_2 e^2}{4\pi\varepsilon_0}\right)^2 \frac{m_1}{m_2 E_0} \frac{dT}{T^2}$$

For a collisions between an ion and an electron (mass m_e and charge $Z_2 = 1$), Thompson's equation takes the form:

$$d\sigma = \frac{2\pi}{m_e v_1^2} \left(\frac{Z_1 e^2}{4\pi\varepsilon_0}\right)^2 \frac{dT}{T^2} \qquad (2.3.12)$$

where v_1 is the initial velocity of the ion. This equation will be used later-on (see paragraph 3.2) to calculate the number of electrons liberated from their parent atoms upon the passage of an energetic ion.

2.3.4 Resonant scattering

When the kinetic energy of the projectile exceeds the upper limit of the Rutherford window, the cross section for elastic scattering can deviate dramatically from the Rutherford value. This is due to the possibility of forming a compound nucleus, which has a high probability of formation at certain resonant energies. These resonances occur when the wave functions representing the colliding nucluei are much alike inside and outside the nuclear potential (see [KRA88]). Resonant scattering can be used beneficially to increase the detection sensitivity for a certain element in a sample, by tuning the ion beam energy to a resonance energy.
An example of resonant scattering behaviour is given in figure 2.3.2 [LEA86]:

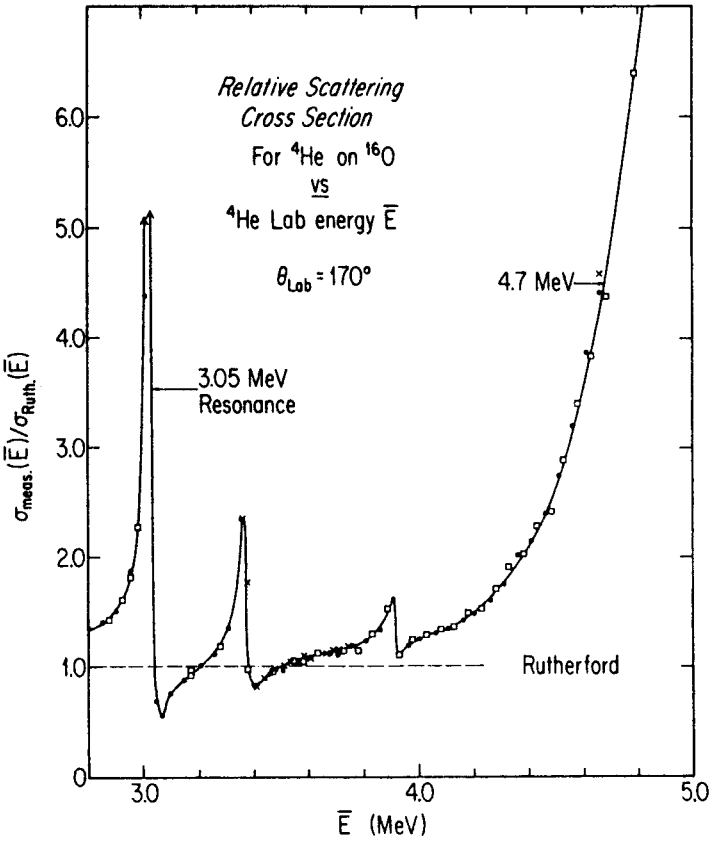

Figure 2.3.2: *relative scattering cross section for elastic resonant He→O scattering.*

Aside from the strong energy dependence of the resonant scattering cross section, there can also be a strong angular dependence. This means that to take benefit from resonant scattering, one should adjust both the beam energy and the scattering angle.

2.4 Stopping of ions in matter

2.4.1 Stopping powers

As an ion propagates through matter, mainly three types of collisions can occur:
- atomic, i.e. collisions involving an ion and a target atom as a whole.
- nuclear: in this case the impinging ion collides with the nucleus of an atom;
- electronic, arising from ion-electron interactions.

The ion transfers its kinetic energy to the target material through these collisions. Atomic collisions occur when the projectiles have relatively low (keV) kinetic energy. When this energy is increased to higher values (MeV) a collision event can cause excitations and ionizations (electronic collisions) and the ion can penetrate the electron cloud and approach the underlying nucleus at close distance (nuclear collisions). In the intermediate energy region, capture and loss of electrons by the projectile play an important role.
A parameter frequently used to quantify the amount of energy lost by an ion traveling through matter is the stopping power. The stopping power is defined as the amount of energy loss per unit length:

$$S = -\frac{dE}{dx} \tag{2.4.1}$$

Two stopping powers are distinguished:
1. the **nuclear** stopping power S_n which mainly stems from energy loss in atomic collisions. In general, true nuclear collisions hardly contribute to the nuclear stopping power mainly because of their low probability to occur.
2. the **electronic** stopping power S_e, representing ion-electron energy transfer.

The kinetic energy loss of a fast moving ion in matter depends heavily on the atomic numbers Z_1 and Z_2 of both projectile and target. For a specific ion-target combination, the stopping power depends strongly on the energy of the projectile, as can be seen in figure 2.4.1.

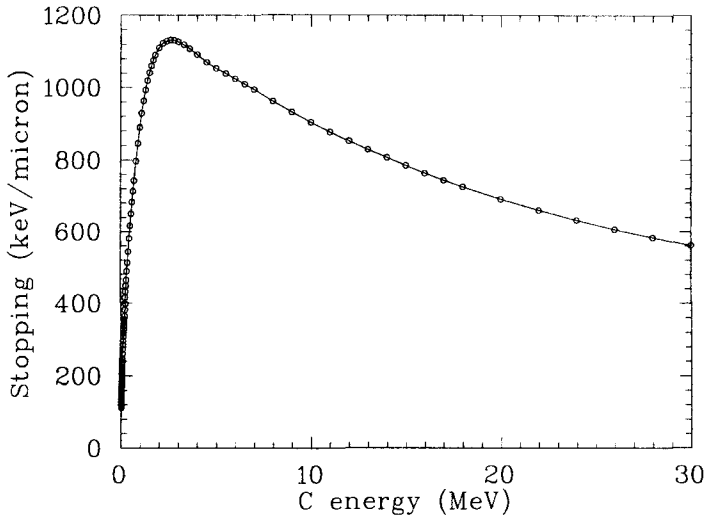

Figure 2.4.1: *an example of a stopping curve, in this case the stopping of C ions in porphyrin material. The curve was generated using the program TRIM.*

The contribution of S_n to the total stopping is only substantial in the low (keV) energy region (the region of atomic collisions). In this energy region, the impinging ion transfers kinetic energy to the target atoms in elastic screened Coulomb collisions (see paragraph 2.4.2). The screening of the nuclear charges by the electron clouds of the colliding particles decreases with increasing ion velocity: less electrons stay bound to the projectile and the electron cloud of the target nucleus can be penetrated. Less screening results in a greater force on the nuclei during the collision and hence more kinetic energy is transferred. Hence, at low energy the nuclear stopping power increases with the kinetic energy of the ion. When the ion velocity is increased further, the impinging nucleus will penetrate the electron cloud of the target nucleus deeper and deeper and the scattering process becomes more and more like Rutherford scattering. In the case of Rutherford scattering, the nuclear energy loss decreases rapidly with increasing ion velocity ($\propto v^{-2}$, see paragraph 2.4.2).

When the kinetic energy of the ion is increased starting from the region of elastic atomic collisions, inelastic collisions which involve excitation and/or ionization of target electrons become important (see paragraph 2.4.3). At first, the energy loss in such electronic collisions rises with ion velocity, as will be briefly explained in paragraph 2.4.3. The behaviour of electronic stopping around the maximum is governed by electron exchange processes between the projectile and the target atom. In this energy region, there is no smooth dependence of the electronic stopping power on the atomic numbers Z_1 and Z_2 of the projectile and the target, respectively. Instead, oscillations occur which depend on the electron affinity of both projectile and target (see [GEY86] and [DIC86] on Z_1 and Z_2 oscillations respectively). Effects due to these oscillations will not be discussed in this work. In the high (MeV) energy region, where the energy loss is almost exclusively due to S_e, the electronic stopping power decreases with the velocity of

the projectile (see paragraph 2.4.3).
The stopping of ions in matter has been studied extensively and many attempts have been made to derive stopping powers theoretically. However, comparison to experimental data shows rather large differences in the region around the stopping maximum even for fairly complex theoretical calculations. Therefore, for practical purposes the use of stopping tables or the computer program TRIM is more convenient. The tables and TRIM use theoretical predictions to interpolate where no experimental results are available.
The energy loss of an ion in matter consists of the sum of the energy transfer in many subsequent collisons on an atomic scale. The probability P_i for an energy transfer T_i to occur in a collision process when an ion travels a distance dx through a material with atomic density N_A can be expressed as follows [GOL93]:

$$P_i = N_A dx \sigma_i \tag{2.4.2}$$

where σ_i is the scattering cross section for the collision event. The mean energy loss -dE can be calculated from:

$$-dE = \sum_i P_i T_i = N_A dx \sum_i T_i \sigma_i \tag{2.4.3}$$

When the average energy loss in a great number of collisions is assumed to be continuous this expression transforms to:

$$-\frac{dE}{dx} = N_A \int T d\sigma \tag{2.4.4}$$

By definition, the stopping cross section ε equals:

$$\varepsilon = -\frac{1}{N_A}\frac{dE}{dx} = \frac{S}{N_A} = \int T d\sigma \tag{2.4.5}$$

The stopping "cross section" has the dimension [Jm^2]. Like the stopping power S, the stopping cross section ε consists of two components for nuclear and electronic stopping, ε_n and ε_e, respectively:

$$\varepsilon = \varepsilon_n + \varepsilon_e = \int T_n d\sigma_n + \int T_e d\sigma_e \tag{2.4.6}$$

2.4.2 Nuclear stopping

At low energies, when nuclear stopping is dominant (in the region of atomic collisions), the central potential in which scattering takes place is not a simple Coulomb potential. As was mentioned before, this is due to screening of the nuclei by their electron clouds. In this case calculation of the scattering cross section (necessary to obtain the stopping cross section) by means of evaluation of the scattering integral (equation 2.3.3) is not straightforward. The usual procedure to tackle this problem is to propose a potential which is a product of the Coulomb potential $V_C(r)$ and so-called screening functions $\Psi(r)$. Various screening functions have been proposed, a historical selection will be listed here:
1. Thomas-Fermi:

$$\Psi_{TF}(x) = \left[1 + \left(\frac{x^3}{144}\right)^{\lambda/3}\right]^{-3/\lambda}, \qquad x = \frac{r}{a_{TF}}, \qquad \lambda = 0.8034 \tag{2.4.7}$$

$$a_{TF} = \frac{1}{4Z_2^{1/3}} \frac{h^2}{(2\pi m_e)^2} \left(\frac{9\pi^2}{2}\right)^{1/3}$$

2. Moliere:

$$\Psi_M(x) = 0.35e^{-0.3x} + 5.5e^{-1.2x} + 0.1e^{-6x} \tag{2.4.8}$$

3. Lenz-Jensen:

$$\Psi_{LJ}(x) = 0.7466e^{-1.038x} + 0.2433e^{-0.3876x} + 0.01018e^{-0.206x} \tag{2.4.9}$$

The nuclear stopping cross section can be obtained by inserting the adjusted potential $V(r)=V_C(r)\Psi(x)$ in the scattering integral and applying the result to:

$$\varepsilon_n = \int T d\sigma = \int T(E_0, b) 2\pi b db \tag{2.4.10}$$

For further calculations, the reader is referred to [ZIE85]. More precise calculations use solid state charge distributions and take interatomic screening (important when the incident ion is still carrying electrons) into account.
In the Rutherford scattering regime we can find ε_n by inserting Thompson's formula (equation 2.3.11) in equation 2.4.10. This results in:

$$\varepsilon_n = \frac{2\pi}{m_2 v_1^2} \left(\frac{Z_1 Z_2 e^2}{4\pi\varepsilon_0}\right)^2 \ln \frac{2m_2 v_1^2}{(1 + m_2/m_1)^2 T_{min}} \tag{2.4.11}$$

The quotient in the logarithmic term represents T_{max}/T_{min}. T_{max} is the kinematically limited maximum energy transfer (calculated from equation 2.2.4 for a head-on collision with recoil angle $\phi=0$). In a true Coulomb potential with infinite range, the minimum energy transfer T_{min} would be zero. For Rutherford ion-atom scattering, a finite minimum arises from screening at large impact parameters. We see that for Rutherford scattering the nuclear stopping cross section is inversely proportional to the kinetic energy of the projectile.

2.4.3 Electronic stopping

For low energy projectiles, electronic stopping increases with ion velocity v_1. This can be understood by the following greatly simplified picture in which the target electrons are regarded as a Fermi gas at zero temperature. All states of electron velocities v_e smaller than the Fermi velocity v_F are occupied, states with $v_e>v_F$ are empty. A collision between an electron with velocity v_e and an ion with mass $m_1>>m_e$ can change the electron velocity from v_e to a value between v_e-v_1 and v_e+v_1, but the Pauli exclusion principle states that only those collisions are possible for which the final velocity lies outside the Fermi sphere. For $v_1<<v_F$, this condition is fulfilled for the electrons that occupy states within the spherical shell given by $v_F-v_1<v_e<v_F$. So only a fraction proportional to v_1/v_F of the total number of electrons in the Fermi gas participate in collisions with the impinging ion. According to this simplified picture, electronic stopping increases linearly with v_1 for $v_1<<v_F$ (see [GOL93]). More advanced calculations also show a v_1 proportionality.
In the high energy region (far above the maximum in the stopping curve), the electronic stopping cross section ε_e is predicted well by the quantum mechanical Bethe-Bloch formula:

$$\varepsilon_e = \frac{4\pi Z_1^2 e^4}{m_e v_1^2 (4\pi\varepsilon_0)^2} Z_2 \left(\ln\frac{2m_e v_1^2}{I} + \ln\frac{1}{1-\beta^2} - \beta^2 - \frac{C}{Z_2} - \frac{\delta}{2} \right) \qquad (2.4.12)$$

in which I is the mean excitation energy, C/Z_2 the shell correction factor, $\delta/2$ the density correction and $\beta=v_1/c$ where c is the speed of light. The formula is derived under the following assumptions:

- The projectile is considered to be a point particle, so the equation only holds for ions that are fully stripped of their electrons;
- the initial velocity of the electron is set equal to zero, implying that the ion velocity must be much higher than the Bohr velocity of the electron;
- the electrons are initially treated as free, a correction for the energy needed for ionization is made later on.

The first term in equation 2.4.12 is very similar to the classical approximation valid for Rutherford type collisions between a bare nucleus and an electron achieved by integrating Thompson's formula:

$$\varepsilon_e = \int T d\sigma = \int_I^{T_{max}} \frac{2\pi}{m_e v_1^2}\left(\frac{Z_1 e^2}{4\pi\varepsilon_0}\right)^2 \frac{dT}{T} = \frac{2\pi}{m_e v_1^2}\left(\frac{Z_1 e^2}{4\pi\varepsilon_0}\right)^2 \ln\frac{2m_e v_1^2}{I} \qquad (2.4.13)$$

This equation deviates from Bethe's first term by a factor two, which indicates a deficiency in the classical treatment. The calculation was based on direct collisions with electrons in the solid. However, an additional term (approximately equal in magnitude) must be added arising from distant resonant energy transfer.

As stated before, electron exchange between the projectile and target atoms plays an important role in the region around the maximum in the stopping curve. To describe how this effects electronic stopping of an ion with atomic number Z_1, one often introduces an artificial point particle with effective charge Z_1^*. For a detailed discussion on the effective charge concept, the reader is referred to [BRA82] or [MAT95].

2.5 PSD ERDA and CERDA-TOF

2.5.1 The pulse shape discrimination (PSD) technique

As mentioned in paragraph 2.1, in pratising ERDA one has to discriminate between recoils and scattered beam particles. The PSD technique provides a way to do so if the recoils of interest are heavier than the beam particles.
The technique is based on the difference between the stopping powers of particles with different masses. The heavy recoils are stopped after having travelled only a short distance in the detector material, whereas the light beam particles (in our case α's) have a much longer range. The detector that is used is a low resistivity PIPS (Planar Implanted Passivated Silicon) detector at low bias voltage. The depletion layer thickness δ (in μm) is controlled by the applied bias voltage V_b (in Volts) according to [KNO79]:

$$\delta \approx 0.56\sqrt{\rho(V_b + 0.6)} \qquad (2.5.1)$$

where ρ is the resistivity of the bulk n-type silicon (in Ωcm). The thickness δ is chosen such that the range of all recoils falls within the depletion layer while α particles with comparable energy pass through the layer and deposit a mayor fraction of their energy behind it. Low energy α's are stopped in the depletion layer.
The recoiled particles deposit all of their energy in the depletion layer of the detector and produce electron-hole pairs that are collected in a very short time. This gives rise to a fast output pulse of the detector. The high energy α particles mainly liberate charge carriers in the neutral zone behind the depletion layer, which will either be collected by the slow process of diffusion or recombine. Consequently these α particles produce an output pulse with a much larger rise time. Recoils and low energy α particles (fast output pulse) can thus be discriminated from high energy α particles (slow output pulse) by means of pulse rise time analysis.
In addition to pulse rise time analysis, which provides a timing signal used for discrimination purposes, pulse height analysis is performed to obtain the energy of the detected particles. Each particle thus produces an energy signal and a timing signal.

2.5.2 CERDA-TOF

Coincident ERDA (CERDA) is an alternative method to discriminate between recoils and scattered projectiles. In CERDA, both recoils and scattered particles are detected by separate detectors.Only if a recoil is detected in coincidence with its scattered collision partner it is treated as valid. This means that most counts arising from scattered beam particles (apart from accidental coincidences) in the recoil detector are disregarded.

Combining CERDA with a time-of-flight measurement (CERDA-TOF) gives the advantage of a better energy resolution (i.e. depth resolution). The recoil energy can be related to the flight time according to:

$$E = \tfrac{1}{2} m \left(\frac{L}{t} \right)^2 \qquad (2.5.2)$$

where t is the time-of-flight and L is the traversed distance. Experimentally, the flight time is obtained by measuring the time elapsed between a start pulse generated by the scattered projectile and a stop pulse coming from the associated recoil. To minimize systematic errors w.r.t. the start signal, the start detector must be placed as close to the sample as possible. Positioning the stop detector at large distance (several meters) increases the flight time and hence the energy resolution.

CHAPTER 3: Ion beam induced damage in solids

When an energetic ion penetrates a solid, numerous interactions take place which can dramatically change the structure of the target material. These structural changes manifest themselves in many different ways depending on the irradiated material and the properties of the ion beam. To illustrate the variety in damage production, some examples are listed below:

- *Ti irradiated with GeV U ions undergoes a transition from one crystalline phase to another in the material surrounding the ion's path [DUN93];*
- *crystalline tracks appear in amorphous silicon (or reverse) subjected to irradiation with various ion beams [TOU92];*
- *in polymers exposed to ion bombardment, effects like chain scissioning, crosslinking and emission of small molecules are observed [CAL92].*

These examples clearly indicate that in materials analysis with ion beams possible damage production never should be overlooked. This is particularly important in the research of organic materials, which are especially sensitive to ion irradiation.
The remainder of this chapter handles the mechanisms behind the various forms of damage production. In paragraph 3.1, we will discuss how different collision processes lead to different forms of damage. A description of the energy distribution process of a fast moving ion in a solid is presented in paragraph 3.2. Paragraph 3.3 contains a brief overview of theoretical models on damage creation. Ion beam induced effects in polymers and other organic compounds will be discussed briefly in paragraph 3.4. Finally, in paragraph 3.5 a model for hydrogen loss from organic materials is presented.

3.1 Damage creation mechanisms qualitatively

3.1.1 Atomic and nuclear collisions

In an atomic collision, a transfer of kinetic energy from the incident ion to the target atom causes the latter to recoil from its original position. This generally causes a collision cascade: repetitive collisions between atoms in the material triggered by the initial ion-atom collision. These cascades result in point defects in crystalline solids and sputtering of elements from the surface of the irradiated material.
The result of sputtering is erosion of the surface under ion bombardment. This effect is most severe in the low energy (keV) region, were the ion transfers a large part of its kinetic energy in atomic collisions. In the relevant energy region for RBS and ERDA (around 1 MeV/amu), the contribution of nuclear stopping to the total energy loss is very small ($\approx 1/1000$). Hence, only a small number of atoms will be sputtered from the surface: typical sputtering yields for MeV light ion beams are ≈ 0.001 atoms per incident ion [FEL86]. Such sputtering yields are very small compared to the loss of elements from organic materials as observed under MeV ion irradiation. In the scope of this work, the effects of sputtering will thus be disregarded.

3.1.2 Ion-electron interactions

In the MeV energy region, the larger part of the energy transfer from ions to solids is due to electronic collisions, leading to excitation and ionization of target atoms. The electrons that are ejected from their orbitals in an ionization event (secondary electrons) can cause additional excitations and ionizations. Hence, the passage of an ion through a solid results in a region of ionized and excited species surrounding its path. This is the region in which so-called tracks are formed: cylindrical zones of modified material.
In the case of organic materials, the initial ionizations and excitations lead to bond breaking and the production of free radicals. These free radicals initiate reactions that lead to modifications of the material. A further discussion on this topic is given in paragraph 3.4.
In materials that are less sensitive to damage, for example silicon, ion-electron energy transfer related damage is still observed. In the ion track, the energy deposited in the electronic system leads to a rearrangement of atoms (for example a crystalline-amorphous transition). Apparently, the energy gained by the electrons is transferred to the atoms; two models that describe this process will be discussed in paragraph 3.3.
Since the energy deposition in the electronic system of the target plays a key role in track formation, the process will receive extra attention in the next paragraph.

3.2 Energy density distribution in the electronic system

Ionization of target atoms by an energetic ion leads to emission of secondary electrons (δ-rays). The energy deposition by these secondary electrons can be calculated by means of the following procedure.
First, we calculate the number of δ-rays that are ejected from their parent atoms due to the passage of a fast moving ion. Using Thompson's formula (i.e. Rutherford scattering) one obtains [KOB68]:

$$\frac{dn}{d\omega} = \frac{2\pi N_e z^2 e^4}{m_e v^2 \omega^2} \tag{3.2.1}$$

where dn is the number of δ-rays emitted per unit path length with energy between ω and dω. N_e is the electron density in the target, z the effective charge number of the ion, e the electron charge, m_e the electron mass and v the ion velocity. The factor $(4\pi\varepsilon_0)^{-1}$ is omitted in this equation; substituting e^2=14.396 eVÅ gives the correct units.
The effective charge number z should be used rather than the atomic number Z, due to possible electron capture by the ion. According to Barkas [WAL86], z can be approximated by:

$$z = Z\left(1 - e^{-125\frac{v}{c}Z^{-2/3}}\right) \tag{3.2.2}$$

The energy ω transferred to a δ-ray is composed of its kinetic energy w and the ionization energy I, hence ω=w+I. Obviously, there is a lower limit ω_{min}=I to the energy transfer for ionization. There is also an upper limit to the maximum kinetic energy of δ-rays which can be derived from classical kinematics:

$$w_{max} = 4\frac{m_e}{m_i}\left(\tfrac{1}{2} m_i v^2\right) = 2 m_e v^2 \tag{3.2.3}$$

The δ-rays are assumed to be ejected normally and to travel in straight line paths. The validity of the normal ejection approximation can be demonstrated by evaluating the differential scattering cross section, which scales with $(\cos^3\varphi)^{-1}$ (see equation 2.3.10).
Next, the energy deposition by δ-rays as a function of radial distance is considered. The residual energy W of δ-rays that have traversed a radial distance r can be calculated from energy-range relations for electrons. From experimental results, the dependence of the range on the initial electron energy has the form [FEL86]:

$$R = \frac{\kappa}{\rho} w^{\alpha} \tag{3.2.4}$$

where ρ is the density of the material and κ is a material independent constant.The exponent α varies roughly from 1.2 to 1.7 for different data-sets.
With k=κ/ρ, the residual energy W of an electron with initial energy w (and corresponding range R) that has travelled a radial distance r is given by:

$$W = \left(\frac{R - r}{k}\right)^{\frac{1}{\alpha}} \tag{3.2.5}$$

We can now calculate the energy $E_t(r)$ transmitted by the δ-rays through a layer of thickness r:

$$E_t(r) = \int_{w_{min}}^{w_{max}} W(w,r)\frac{dn}{dw}dw \tag{3.2.6}$$

where w_{max} is the kinematically limited maximum electron energy and w_{min} is the energy corresponding to electrons with range R=r wich will just be transmitted through the layer. The energy density D(r) deposited by δ-rays emitted normally w.r.t. the ion's path in a cylindrical slice of radius r, thickness dr and unit length can be written as:

$$D(r) = \frac{1}{2\pi r}\left(-\frac{dE_t(r)}{dr}\right) \tag{3.2.7}$$

The energy density distribution function is thus given by:

$$D(r) = \frac{-1}{2\pi r}\int_{w_{min}}^{w_{max}} \frac{dW}{dr}\frac{dn}{dw}dw \tag{3.2.8}$$

In the following two cases, an exact solution of this expression can be found:
1. The energy-range relation for the electrons in the material is supposed to be linear and the electrons are considered to be bound with ionization potential I;
2. The electrons are assumed to be free (I=0) and the range-energy relation is taken to be a power law.

The first case is that of the linear equation R=kw:

$$W = \frac{1}{k}(R - r)$$

$$D(r) = \frac{1}{2\pi r}\int_{w_{min}}^{w_{max}}\left(-\frac{dW}{dr}\right)\frac{dn}{dw}dw = \frac{N_e e^4 z^2}{m_e v^2 r k}\left(\frac{1}{w_{min} - I} - \frac{1}{w_{max} - I}\right) \tag{3.2.9}$$

To obtain an expression in terms of $r=kw_{min}$ and the maximum range $R_{max}=kw_{max}$ we define $\theta=kI$ and find:

$$D(r)=\frac{N_e e^4 z^2}{m_e v^2 r}\left(\frac{1}{r-\theta}-\frac{1}{R_{max}-\theta}\right) \tag{3.2.10}$$

We now treat the second case: a power law energy-range relation and free electrons:

$$R=kw^{\alpha}, \qquad \frac{dR}{R}=\alpha\frac{dw}{w}, \text{ for substitution in the integral expression}$$

$$W=\left(\frac{R-r}{k}\right)^{\frac{1}{\alpha}}=w\left(1-\frac{r}{R}\right)^{\frac{1}{\alpha}}, \qquad -\frac{dW}{dr}=\frac{w}{\alpha R}\left(1-\frac{r}{R}\right)^{\frac{1}{\alpha}-1} \tag{3.2.11}$$

$$D(r)=\frac{1}{2\pi r}\int_{w_{min}}^{w_{max}}\left(-\frac{dW}{dr}\right)\frac{dn}{dw}dw=\frac{N_e e^4 z^2}{\alpha m_e v^2 r}\int_{w_{min}}^{w_{max}}\frac{1}{R}\left(1-\frac{r}{R}\right)^{\frac{1}{\alpha}-1}\frac{dw}{w}, \qquad \text{with } I=0$$

$$D(r)=\frac{N_e e^4 z^2}{\alpha^2 m_e v^2 r}\int_{r}^{R_{max}}\left(1-\frac{r}{R}\right)^{\frac{1}{\alpha}-1}\frac{dR}{R^2}=\frac{N_e e^4 z^2}{\alpha m_e v^2 r}\frac{\left(1-r/R_{max}\right)^{\frac{1}{\alpha}}}{r}$$

A coarse correction for the assumption I=0 can be obtained by comparing equations 3.2.10 and 3.2.11. Taking I=0 while solving the integral in equation 3.2.9 results in an expression which can be obtained by substitution of:

$$r+\theta \Rightarrow r$$
$$R_{max}+\theta \Rightarrow R_{max} \tag{3.2.12}$$

in equation 3.2.10. We now apply the inverse substitution to equation 3.2.11:

$$D(r)=\frac{N_e e^4 z^2}{\alpha m_e v^2 r}\left(\frac{1}{r+\theta}\left(1-\frac{r+\theta}{R_{max}+\theta}\right)^{1/\alpha}\right) \tag{3.2.13}$$

wich is assumed to describe the energy deposition by secondary electrons which were bound with ionization potential I and obey a power law energy-range relation.
Waligorsky et al. [WAL86] corrected equation 3.2.13 by comparing the energy density distribution D(r) around the paths of protons in liquid water with Monte Carlo calculations.

This semi-empirical corrected formula also accounts for primary ionization and excitation events and takes the form:

$$D'(r) = D(r)(1 + K(r)) \tag{3.2.14}$$

in which the correction function K(r) is given by:

$$K(r) = A\left(\frac{r - B}{C}\right)e^{-(r-B)/C} \tag{3.2.15}$$

The fitting constants are given in [WAL86] and will not be presented here.
Equation 3.2.14 is plotted in figure 3.2.1 for He ions of various energies in porphyrin material. Following Waligorsky et al., we used $\kappa=6\cdot10^{-6}$ g·cm^{-2}keV$^{-\alpha}$ and $\alpha=1.079$. The porphyrins have mass density $\rho=1.35$ g/cm^3, hence $k=\kappa/\rho=4.45\cdot10^{-6}$ keV$^{-\alpha}$cm. The mean ionization energy I was arbitrarily set equal to 10 eV, which has the correct order of magnitude for the ionization of valence electrons in organic materials (Waligorsky et al. used the same value for their calculations in liquid water). Only outer shell ionizations were considered, Z_2 and shell effects are disregarded in this rough calculation. The valence electron density N_e in porphyrin material amounts to approximately 275 nm^{-3}.

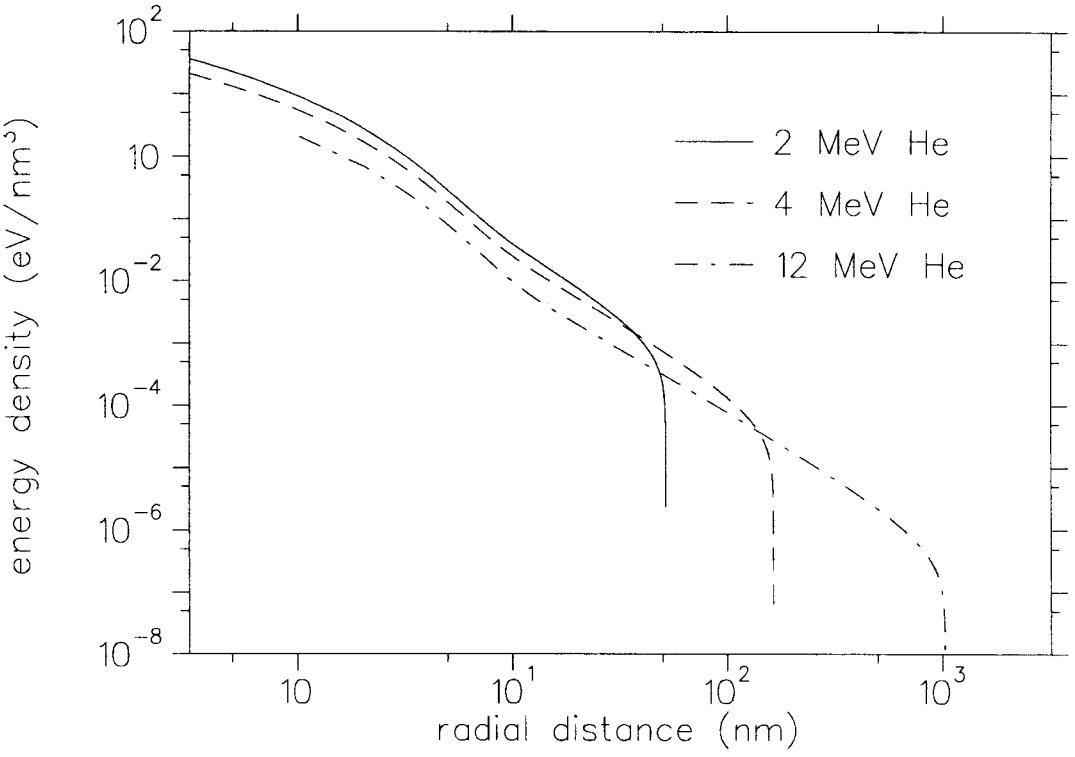

Figure 3.2.1: *double logarithmic plot of the energy density deposited by secondary electrons as a function of the radial distance to the path of He ions in porphyrins.*

By radial (numerical) integration of equation 3.2.14 the stopping power is obtained:

$$-\frac{dE}{dx} = \int_0^\infty D(r)2\pi r dr \qquad (3.2.16)$$

where x denotes the pathlength traversed by the impinging ion and E its kinetic energy. A comparison of the so obtained stopping power with TRIM calculations (see [ZIE85]) is shown in figure 3.2.2, which shows a reasonable agreement between the two curves.

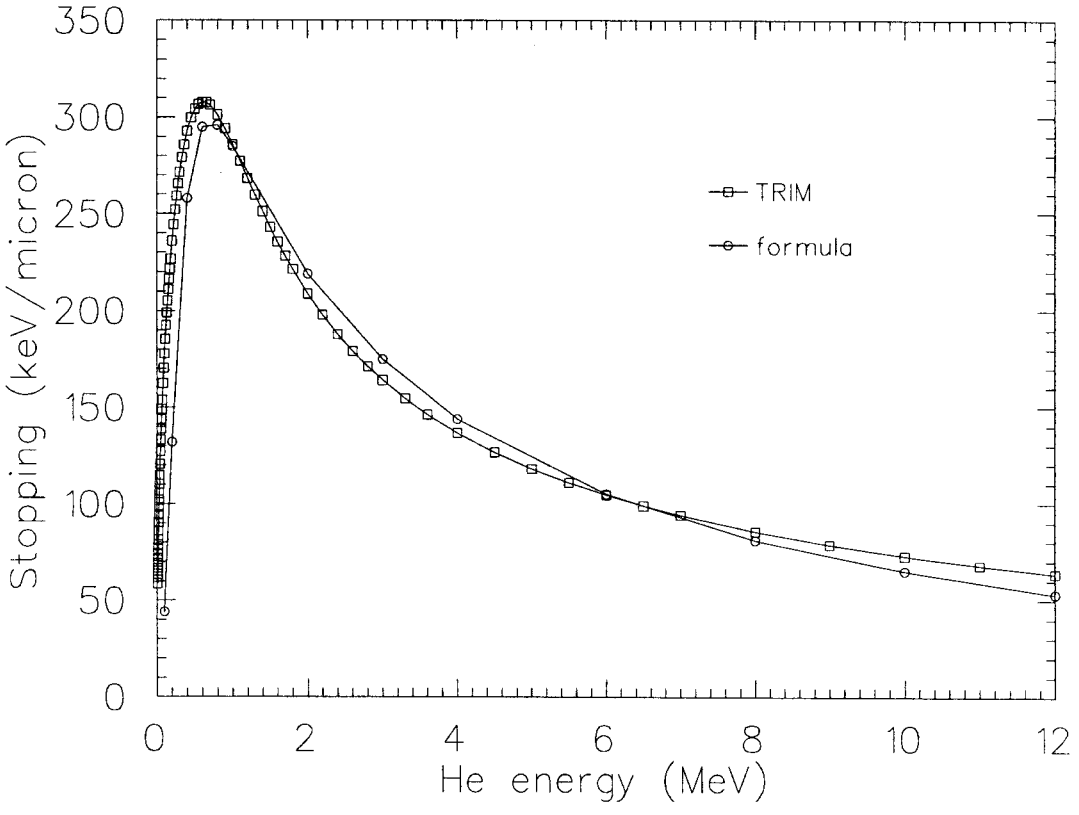

Figure 3.2.2: *Stopping of He ions in porphyrins as calculated by TRIM and the numerically integrated energy density function.*

3.3 Theoretical models on track formation

3.3.1 The Coulomb explosion model

As stated before, the interaction of an ion with electrons results in ionization and excitation of target atoms. Consequently a zone of positively charged ions is created along the path of the incident particle. These ions are set in motion by mutual Coulomb repulsion and thus gain kinetic energy. The time span over which the charge distribution is maintained can be approximated by the inverse of the plasma frequency $\omega_p=(e^2n_e/(\varepsilon_0 m_e))^{1/2}$ for a system formed by the valence electrons and the positive cores. For an electron density $n_e \approx 10^{23}$ electrons/cm^3 the inverse plasma frequency amounts to 10^{-16} s (order of magnitude) [FEL86]. During this very short time the ionized atoms will only receive a small amount of kinetic energy (typically 0.1 to 1 eV). However, if the initial movement of the ionized target atoms is coherent (in a sense that all ions start to move at the same time) a shock wave is formed. In the Coulomb explosion model, this shock wave is considered to be the main source of damage production. Using linear elasticity theory of isotropic media, the wave equation can be represented by [AUD93]:

$$\frac{\partial}{\partial r}\left(\frac{1}{r}\frac{\partial}{\partial r}(ru(r,t))\right)=\frac{1}{s^2}\frac{\partial^2}{\partial t^2}u(r,t) \tag{3.3.1}$$

where s is the longitudal sound velocity. The radial displacement of atoms at a distance r from the ion's path at time t is described by u(r,t). The initial conditions for u(r,t) and its time derivative are:

$$\begin{aligned} u(r,0) &= 0 \\ \frac{\partial u(r,0)}{\partial t} &= v_0(r) \end{aligned} \tag{3.3.2}$$

The exact form of $v_0(r)$ will be considered later on. The solution to this problem is known to be:

$$u(r,t)=\int_0^\infty J_1(\lambda r)\sin(\lambda st)d\lambda\int_0^\infty \frac{v_0(r')}{s}J_1(\lambda r')r'dr' \tag{3.3.3}$$

The displacement of atoms results in a local dilatation (proportional to the local pressure) given by:

$$\delta(r,t)=\frac{1}{r}\frac{\partial}{\partial r}(ru(r,t))=\int_0^\infty \lambda J_0(\lambda r)\sin(\lambda st)d\lambda\int_0^\infty \frac{v_0(r')}{s}J_1(\lambda r')r'dr' \tag{3.3.4}$$

Consider an initial cylindrical space charge of the form:

$$\rho(r,t') = \rho_0, \quad r \le b \text{ and } t' \le \tau$$
$$\rho(r,t') = 0, \quad r > b \text{ or } t' > \tau \tag{3.3.5}$$

where it is assumed that the space charge density formed by the electrons that were ejected from the cylinder is negligible because the volume within which these electrons are present is large compared to the volume that contains the ionized atoms. The radius b of the cylinder may be estimated from the energy distribution function. The initial charge density contained in this region is given by:

$$\rho_0 = \frac{\lambda}{\pi b^2}, \qquad \lambda = \frac{eS_e}{W} \tag{3.3.6}$$

λ, the line charge density generated by the passage of the incident ion, is assumed to be proportional to the ratio of the electronic stopping power S_e and the mean ionization energy W. The charge is neutralized after a time τ in which the electrons return to the track. This space charge distribution results in an electric field which can be described by:

$$\vec{\nabla} \cdot \vec{E} = \frac{1}{r}\frac{\partial}{\partial r}(rE_r) = \frac{\rho(r)}{\varepsilon_0}, \qquad \vec{E}(r,\varphi,z) = \begin{pmatrix} E_r \\ 0 \\ 0 \end{pmatrix}$$

$$E(r,t') = \frac{\rho_0}{2\varepsilon_0} r, \qquad r \le b \qquad t' \le \tau$$
$$E(r,t') = \frac{\rho_0 b^2}{2\varepsilon_0 r}, \qquad r > b \qquad t' \le \tau \tag{3.3.7}$$
$$E(r,t') = 0, \qquad \forall r \qquad t' > \tau$$

At time τ, when the charge is neutralized, the velocity distribution in the track region is:

$$v_0(r) = \frac{\rho_0^2 N_A \tau}{m_a N_a 2\varepsilon_0} r \tag{3.3.8}$$

where N_A is Avogadro's number, m_a is the atomic mass and N_a is the atomic density. The time τ is taken to be the time origin for the shock wave differential equation. Finally an expression for the dilatation as a function of radial distance and time is obtained. Transitions between crystalline states can be explained in terms of the described compression wave [DUN93].
The effect of Coulomb explosion becomes more pronounced if the number of ions initially produced is increased. The ionization density should thus be sufficiently high, which is the case when the electronic stopping power is large.

3.3.2 Thermal spike theory

The transfer of energy from the electrons (which have gained energy in collisions with the fast moving ion) to the atoms can be described through heat flow relations. The theory treats the electrons and the atoms as separate systems which mutually interact. A gain in kinetic (thermal) energy of the target atoms results.
The thermal behavior of the electrons and the atoms is modeled using two coupled inhomogenous differential equations [TOU94]:

$$\rho C_e(T_e)\frac{\partial}{\partial t}T_e = \frac{\partial}{\partial r}\left(K_e(T_e)\frac{\partial}{\partial r}T_e\right) + \frac{K_e(T_e)}{r}\frac{\partial}{\partial r}T_e - g(T_e - T_a) + A(r)$$

$$\rho C_a(T_a)\frac{\partial}{\partial t}T_a = \frac{\partial}{\partial r}\left(K_a(T_a)\frac{\partial}{\partial r}T_a\right) + \frac{K_a(T_a)}{r}\frac{\partial}{\partial r}T_a + g(T_e - T_a) \qquad (3.3.9)$$

in which the indices e and a refer to electrons and atoms respectively, T is the temperature, ρ the material density, C and K are the specific heat and thermal conductivity, $g(T_e-T_a)$ is the electron atom coupling and A(r) the energy density deposited per unit time by the incident ion in the electron system. The "electron equation" concerning the electron temperature T_e can be solved analytically if the following approximations are made:

- mean values are assumed for the electron diffusivity $D=K_e/(C_e\rho)$;
- the electron-atom interaction time $\tau_a=(C_e\rho/g(T_e-T_a))T_e$ is constant and large w.r.t. the electron-electron interaction time;
- an alternative energy distribution function A(r) is proposed in order to be able to solve the differential equation;

Because τ_a is large, the electron system can be assumed to be in a steady state compared to the atoms and the term $g(T_e-T_a)$ can be neglected. Rewriting the electron equation gives:

$$\frac{\partial}{\partial t}T_e = D\left(\frac{\partial^2}{\partial r^2}T_e + \frac{1}{r}\frac{\partial}{\partial r}T_e\right) + \frac{1}{\rho C_e}A(r) \qquad (3.3.10)$$

We approximate A(r) by a Gaussian distribution:

$$A(r) = \xi e^{-r^2/4\sigma^2}, \qquad \sigma^2 = \frac{R_d^{\,2}}{4} + Dt \qquad (3.3.11)$$

This distribution is constructed to be at 1/e of its maximum when $r=R_d$ at t=0, where R_d is the radius within which 65% of the total energy is deposited. The spreading of the energy density in time is accounted for by the factor Dt.
A solution for T_e is given by:

$T_e = \Gamma e^{-r^2/4\sigma^2}$, wich can be checked by substitution in equation 3.3.10:

$$\frac{\partial}{\partial t} T_e = \frac{Dr^2}{4\sigma^4} T_e \tag{3.3.12}$$

$$D\left(\frac{1}{r}\frac{\partial}{\partial r} T_e + \frac{\partial^2}{\partial r^2} T_e\right) = \frac{Dr^2}{4\sigma^4} T_e - \frac{D}{\sigma^2} T_e$$

and $$A(r) = \rho C \frac{D}{\sigma^2} \Gamma e^{-r^2/4\sigma^2}$$

The constant Γ has the dimension [K], giving the correct dimension [W/m^3] for A(r). Recall that $g(T_e-T_a)=T_e\rho C_e/\tau_a$ was assumed while solving the electron equation. Define N(r,t), the electron-atom coupling which is to be inserted in the "atom equation" (see equation 3.3.9), as:

$$N(r,t) = g(T_e - T_a) = \frac{1}{\tau_a}\frac{dE}{dx} \Psi e^{-r^2/4\sigma^2} f(t) \tag{3.3.13}$$

The time dependence of the coupling can not be omitted in this case, hence an additional f(t) is incorporated. Writing N(r,t) in this form allows for substitution of the electronic stopping power. The "constant" ψ can be obtained by normalization:

$$\int_0^\infty \Psi e^{-r^2/4\sigma^2} 2\pi r dr = 1 \tag{3.3.14}$$

$$\Psi = \frac{1}{4\pi\sigma^2}$$

The energy deposition by electrons in the atomic system is known to follow a exponential decay [TOU92]: $f(t)=\exp(-t/\tau_a)$. Summarizing:

$$N(r,t) = \frac{1}{\tau_a}\frac{dE}{dx} e^{-t/\tau_a} \frac{1}{4\pi\sigma^2} e^{-r^2/4\sigma^2} \tag{3.3.15}$$

Inserting this in the atom equation allows for calculation of the temperature in the material as a function of radial distance and time. Taking mean values for the heat capacity and the thermal conductivity will not lead to reasonable results now, especially since a phase change (solid to liquid or vapour) will occur. Hence, the differential equation must be solved numerically. Toulemonde et al. used this procedure to calculate the radii of the molten cylinders in a-Ge and a-Si irradiated with various energetic (GeV) heavy ions [TOU92].

3.4 Ion irradiation damage in organic materials

Ion irradiation of polymers results in irreversible changes in the molecular structure. Such changes generally include [CAL92]:

- crosslinking of polymer chains, depicted below for polyethylene;

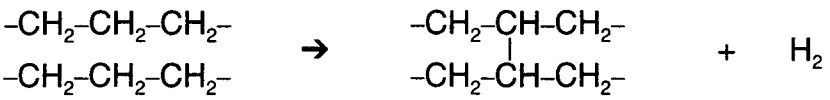

- emission of small molecules (H_2, CH_3 etc.), which for example occurs in the crosslinking reaction shown above;
- chain scissioning (i.e. cleavage of the main chain);
- bond rearrangement within the molecules.

The process that initiates these changes is the energy transfer from the incident ion to the polymer by primary ionizations and excitations. The energy is distributed to a small volume surrounding the ion's path by secundary electrons. The amount of energy stored in the electronic molecular environment is generally much larger than the typical binding energies of organic molecules. Hence the molecules that have absorbed the energy will suffer from bond cleavages, giving rise to free radicals. These free radicals subsequently induce chemical transformations of the polymer in a volume much larger than the ion track due to diffusion effects.

The exact modifications to the material depend strongly on the molecular structure of a specific polymer. For example, increased branching has a weakening effect on the main chain, as can be seen by comparing the behaviour under ion irradiation of polyethylene (PE), polypropylene (PP) and polybutylene (PB,) [CHA88]:

- PE undergoes mainly crosslinking;
- in PP crosslinking and chain scissioning occur in equal measure;
- PB suffers almost entirely from chain scissioning.

A similar weakening effect of a tetra-substituted carbon atom on the main chain can also be observed from the behaviour of polymethylmetacrylate (PMMA), which is a typically scissioning polymer.

The presence of phenyl rings in the molecular structure tends to strengthen the main chain by trapping of the excitation energy. This can be seen from irradiated polystyrene (PS) in which scissioning is negliable.

All polymers show emission of small molecules (H_2 in particular). The emission rate depends strongly on the energy deposition by the bombarding ions. For example, in polystyrene a threshold in the range 15-20 eV/Å is observed. Below the threshold crosslinking occurs with a very low H_2 release rate. Above the threshold the release rate is about ten times faster. This behaviour can be explained by considering that a different kind of reaction is initiated at sufficiently high energy deposition.

In general, amorphization of organic materials occurs under ion irradiation. At high ion fluence, an amorphous carbon-like state is formed which has little "memory" of the original structure.

3.5 Hydrogen loss model

The loss of hydrogen from organic materials under ion irradiation is initiated by molecular bond cleavages in the tracks of the impinging ions. As a result of these bond cleavages, free hydrogen radicals are formed. A fraction of these radicals will eventually escape from the material in the form of H_2. We will discuss the hydrogen loss process in two steps:

1. *the formation of free hydrogen radicals in the ion track;*
2. *the release of hydrogen from the material.*

As an improvement of the previously developed hydrogen release model by Adel et al. [ADE89], a new model is proposed which treats the mechanisms of direct combination, diffusion and trapping of radicals, as will be explained below.

3.5.1 Bond cleavage in the ion track

The primary step in the hydrogen release process is the cleavage of molecular bonds due to electronic energy deposition by the incident ions. In paragraph 3.2, we already calculated the energy deposition by secondary electrons (δ-rays) as a function of the radial distance to the ion's path. These calculations indicate that increasing the ion's velocity (i.e. kinetic energy) basically has two effects:

1. the number of secondary electrons ejected from their parent atoms is reduced;
2. the average kinetic energy of the secondary electrons increases.

When the kinetic energy w (and corresponding range R) of the δ-rays is increased, a larger track results. Together with a decreased number of ejected secondary electrons per unit path length, this leads to a lower energy density in the track.

From the differential energy distribution (equation 3.2.1) the mean kinetic energy w_m of the secondary electrons can be calculated according to:

$$w_m = \frac{\int_0^{w_{max}} w\frac{dn}{dw}dw}{\int_0^{w_{max}} \frac{dn}{dw}dw} = \frac{2m_e v^2 I}{2m_e v^2 - I}\ln\frac{2m_e v^2}{I} - I \qquad (3.5.1)$$

where dn/dw is given by equation 3.2.1 and w_{max} is the kinematically limited maximum kinetic energy of the δ-rays (see equation 3.2.3). Recall that v is the ion's velocity, m_e the electron mass and I the (average) ionization energy: I≈10 eV. In the case of an impinging ^{4}He ion with a kinetic energy of 2 MeV one finds that w_m is 37 eV, which means that approximately 80% of the energy transfer in an ionization event is carried by the ejected secondary electron. This stresses the importance of secondary electrons with respect to energy deposition and hence the creation of damage.

In order to incorporate the size of the ion track into the hydrogen loss model, we define an effective track radius r_{eff} equal to the range of the δ-rays with kinetic energy w_m: $r_{eff} = k(w_m)^{\alpha}$ (see paragraph 3.2). Effectively, this means that all secondary electrons are assumed to have

kinetic energy w_m, which reduces the ion track to an artificial cilinder with radius r_{eff}. Following this procedure, one finds effective track radii in porphyrin material ($k=4.45\cdot10^{-6}$ $keV^{-\alpha}cm$) of 1.3 and 2.0 nm for 2 MeV and 12.1 MeV He ions, respectively.
Within the cilinder defined by r_{eff}, hydrogen radicals are produced through molecular bond cleavage with a probability that depends on the total number of emitted δ-rays N_δ:

$$N_\delta = \int_0^{w_{max}} \frac{dn}{dw} dw \qquad (3.5.2)$$

As a rough estimate, the bond breaking probability ξ within the track can be expected to scale with N_δ. We will now focus on the processes that lead to the escape of the free hydrogen radicals from the material.

3.5.2 Hydrogen release

A crucial question arises when one considers the loss of hydrogen from organic materials: are the released molecules formed at the surface after atomic diffusion through the layer or are they created in the bulk? Wild et al. [WIL87] showed experimentally that hydrogen depletion from double layers of hydrogenated and deuterated amorphous carbon (a-C:H and a-C:D) occured through the creation of molecules in the bulk followed by molecular outdiffusion. The effect of hydrogen loss by means of atomic diffusion to the surface is negligible because of the high probability that a diffusing hydrogen atom is trapped by a "dangling" bond in the amorphous network.
It is stated frequently in literature that an amorphous network with similar characteristics as a-C:H is formed in all organic materials after a deposited ion fluence of typically 10^{14}-10^{15} He ions/cm^2 (see for example [CAL92]). Hence, at higher ion fluences, a similar scenario for hydrogen depletion from organic materials is likely to be valid in general. At low fluence, atomic diffusion to the surface may enhance hydrogen loss in organic materials that initially contain few potential traps for free hydrogen radicals. In porphyrins, the initial trap concentration is large: free hydrogen atoms are easily captured by the π-electrons (see paragraph 4.1 and [BAR95]) of the carbon atoms in the molecules. Hence, hydrogen loss through atomic diffusion to the surface of a porphyrin layer can be expected to be negligible even at low irradiation dose.
We now consider the combination of two liberated hydrogen atoms to a hydrogen molecule in the track of an impinging ion. If the atoms are freed within a very close distance, a hydrogen molecule will be formed instantly. An estimate of the maximum distance within which direct combination is possible, can be obtained by observing of the molecular potentials of H_2 and H_2^+ as a function of nuclear separation in vacuum, which decrease rapidly after a seperation of 3 and 5 Å, respectively [ADE89]. Because the molecular potentials are effected by screening in solid materials, these numbers represent an upper limit for the distance λ within which two liberated hydrogen atoms will form a molecule directly. The condition for direct combination of two hydrogen atoms is thus that both atoms are created within a volume $V=4/3\pi\lambda^2$.
Another possibility of forming a hydrogen molecule is the combination of two free radicals

after diffusion through the material. This process competes with the trapping of free hydrogen atoms. Both mechanisms will be discussed next.

3.5.2.1 Direct combination of hydrogen radicals

The direct formation of molecules by combination of two liberated hydrogen atoms is only possible if both atoms are freed within a certain combination volume V, as explained above. If the hydrogen density in the material is given by ρ, an average number of ρV bound hydrogen atoms are present within V. We now apply standard statistics to calculate the average number of molecules that will be formed of these ρV atoms that can be liberated with bond cleavage probability ξ.
The actual number of bound hydrogen atoms in any combination volume V can be described by a Poisson distribution with mean ρV. As a first approximation, we only consider the possibilities of finding N or N+1 atoms, with N being the integer part of ρV. The corresponding probabilities are given by $P_N=(1+N-\rho V)$ and $P_{N+1}=(\rho V-N)$ respectively (if for example $\rho V=2.3$, there is a 70% chance of finding 2 atoms within V and a 30% chance that 3 atoms are present).
Consider the case of N bound hydrogen atoms present within V. The probability P_n of liberating n of these N atoms is given by:

$$P_n = \xi^n (1-\xi)^{N-n} \binom{N}{n} \tag{3.5.3}$$

A molecule can be formed if at least two hydrogen bonds are broken, i.e if $n \geq 2$. For the formation of a second molecule, again two liberated atoms are needed etc. The average number of molecules N_{mol} formed from N bound atoms within V that can be freed with probability ξ is thus given by:

$$N_{mol} = \sum_{n=2}^{N} \mathrm{int}\left(\tfrac{1}{2}n\right) \xi^n (1-\xi)^{N-n} \binom{N}{n} \tag{3.5.4}$$

where int(½n) represents the integer part of ½n. Hence, the average number of molecules formed within V as a function of hydrogen density ρ equals:

$$N_{mol} = (1+N-\rho V) \sum_{n=2}^{N} \mathrm{int}\left(\tfrac{1}{2}n\right) \xi^n (1-\xi)^{N-n} \binom{N}{n} + (\rho V - N) \sum_{n=2}^{N+1} \mathrm{int}\left(\tfrac{1}{2}n\right) \xi^n (1-\xi)^{N+1-n} \binom{N+1}{n} \tag{3.5.5}$$

which consists of two terms corresponding to N and N+1 atoms within the volume V.

When ξ is small and the average number of atoms ρV within V is not very large, equation 3.5.5 can be approximated by (see figure 3.5.1):

$$N_{mol} = \xi^2 \tfrac{1}{2}\rho V(\rho V - 1) \qquad (3.5.6)$$

which is the equation that appeared earlier in the hydrogen loss model formulated by Adel et al. [ADE89]. The validity of the approximation can be seen by realizing the following.
For small ξ, the terms in equation 3.5.5 that contain ξ^n with $n \geq 3$ can be neglected. Furthermore, $1-\xi \approx 1$ and the binomial coefficient for n=2 equals ½N(N-1) where N is the number of atoms within V. Taking $N=\rho V$ and hence allowing N to be a real (i.e. non-integer) number gives equation 3.5.6. The validity of the assumption $\xi << 1$ will be discussed further on in this paragraph.
$(d\rho/di)_{dir}$, the density decrease in the track per impinging ion (in an experiment, the same track is hit many times) due to direct combination, is given by:

$$\left(\frac{d\rho}{di}\right)_{dir} = -\frac{2N_{mol}}{V} \qquad (3.5.7)$$

N.B: the process of direct combination ceases when (on the average) only one atom remains within V.

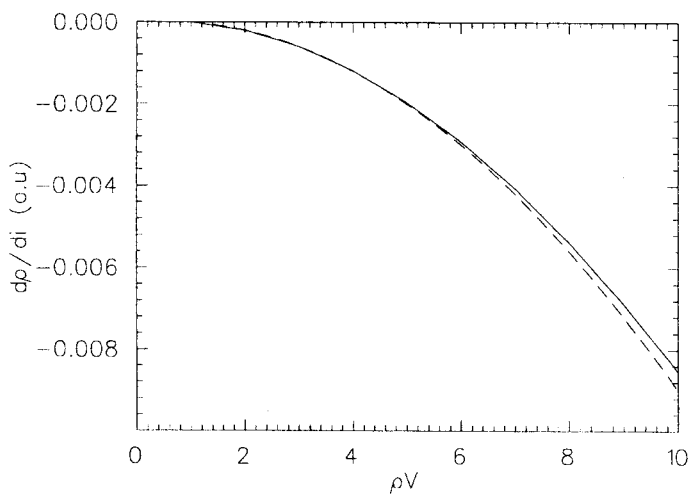

Figure 3.5.1: *Comparison of $d\rho/di$ as calculated from equations 3.5.5 (solid line) and 3.5.6 (dashed line) with ξ=0.01 versus the number of atoms ρV within V. A bond breaking probability of 0.01 has the correct order of magnitude in the case of ^{4}He bombardment, as will be shown in chapter 5.*

3.5.2.2 Hydrogen molecules formed by diffusing radicals

If a free hydrogen radical cannot instantly form a molecule with another liberated atom, it will diffuse through the material untill it is either trapped or it reacts with a second diffusing atom. This process can be discribed by two competing chemical reactions in the track:

1) $H+H \rightarrow H_2$

2) $H+T \rightarrow TH$

where T represents a "hydrogen trap" and HT a trapped hydrogen atom. According to standard reaction kinematics, the reaction rate equations are given by:

$$\frac{d[H_2]}{dt} = k_1[H]^2$$

$$\frac{d[HT]}{dt} = \kappa_2[H][T] \approx k_2[H] \qquad \text{with} \quad k_2 = \kappa_2[T] \tag{3.5.8}$$

where [..] denotes a concentration and k_1 and κ_2 are reaction constants. N.B: the time t in equation 3.5.8 corresponds to the time during which the reactions take place, starting from the passage of an impinging ion. This is <u>not</u> correlated to the time elapsed between two subsequent passages of ions through the same track region: each ion triggers new reactions. Taking typical values for the beam current (50 nA), the track area (in the order of 10 nm^2) and the beamspot area (10 mm^2) one finds that the time between two passages is in the order of seconds. Since the reaction time (limited by the diffusion of the hydrogen radicals) is in the order of μs, only radicals that are produced in a single ion track can escape in the form of H_2, and hence the beam current (i.e. the number of ions impinging per unit time) does not affect hydrogen release. Indeed, no beam current dependence of hydrogen loss has been observed experimentally (see [MAR96]).
If the concentration of traps [T] is assumed to be large w.r.t. the concentration of free hydrogen radicals [H], a new reaction constant $k_2=\kappa_2[T]$ can be defined for the trapping reaction. The assumption $[H] \ll [T]$ is realistic, because hydrogen radicals are created with (small) probability ξ while traps are always present.

The solution to equation 3.5.8 can be derived to be:

$$[H_2](t) = -\tfrac{1}{2}\frac{H_0 e^{-k_2 t}}{1+\frac{2k_1}{k_2}H_0\left(1-e^{-k_2 t}\right)} - \frac{k_2}{4k_1}\ln\left(1+\frac{2k_1}{k_2}H_0\left(1-e^{-k_2 t}\right)\right) + \tfrac{1}{2}H_0$$

(3.5.9)

$$[HT](t) = \frac{k_2}{2k_1}\ln\left(1+\frac{2k_1}{k_2}H_0\left(1-e^{-k_2 t}\right)\right)$$

where H_0 is the concentration of free radicals in the ion track at t=0, thus directly after the passage of the impinging ion, which is given by $\xi\rho+(d\rho/di)_{dir}$, i.e. the average density of liberated atoms minus the fraction that forms H_2 because of direct combination. The H_2 molecules produced in the reaction are released from the material, the trapped radicals obviously are not. The atomic hydrogen density ρ in the track thus decreases by an amount of $2[H_2](\infty)$ atoms per unit volume (at $t=\infty$ all hydrogen radicals are gone, they are either trapped in the material or released in the form of H_2):

$$[H_2](\infty) = \tfrac{1}{2}H_0 - \frac{k_2}{4k_1}\ln\left(1+H_0\frac{2k_1}{k_2}\right)$$

(3.5.10)

$$\left(\frac{d\rho}{di}\right)_{rea} = -2[H_2](\infty) = -\left(H_0 - \frac{k_2}{2k_1}\ln\left(1+H_0\frac{2k_1}{k_2}\right)\right)$$

where $(d\rho/di)_{rea}$ denotes the density decrease as a result of the combination of diffusing radicals per ion passing through the track region.

3.5.2.3 Hydrogen content as a function of ion fluence

Adding the two contributions $(d\rho/di)_{dir}$ and $(d\rho/di)_{rea}$ gives the total density decrease $d\rho/di$:

$$\left(\frac{d\rho}{di}\right)_{dir} = -\frac{2}{V}\left\{(1+N-\rho V)\sum_{n=2}^{N}\mathrm{int}\left(\tfrac{1}{2}n\right)\xi^n(1-\xi)^{N-n}\binom{N}{n} + (\rho V-N)\sum_{n=2}^{N+1}\mathrm{int}\left(\tfrac{1}{2}n\right)\xi^n(1-\xi)^{N+1-n}\binom{N+1}{n}\right\}$$

(3.5.11)

$$\frac{d\rho}{di} = \left(\frac{d\rho}{di}\right)_{dir} - \left[\xi\rho+\left(\frac{d\rho}{di}\right)_{dir} - \frac{k_2}{2k_1}\ln\left(1+\frac{2k_1}{k_2}\left(\xi\rho+\left(\frac{d\rho}{di}\right)_{dir}\right)\right)\right]$$

For small ξ, this expression can be simplified significantly. As we saw earlier, the direct

combination contribution can then be approximated by $(d\rho/di)_{dir}=-\xi^2\rho(\rho V-1)$ (see equations 3.5.5 and 3.5.6). Furthermore, $(d\rho/di)_{dir}$ (which scales with ξ^2) is small w.r.t. $\xi\rho$ which means that $H_0\approx\xi\rho$ in equation 3.5.10. Making use of the power series expansion of ln(1+x) and taking $H_0=\xi\rho$ with $\xi<<1$ in equation 3.5.10 gives:

$$\left(\frac{d\rho}{di}\right)_{rea} = -\left(\xi\rho - \frac{k_2}{2k_1}\ln\left(1+\xi\rho\frac{2k_1}{k_2}\right)\right) = \tag{3.5.12}$$

$$= -\xi\rho + \frac{k_2}{2k_1}\left\{\frac{2k_1}{k_2}\xi\rho - \tfrac{1}{2}\left(\frac{2k_1}{k_2}\xi\rho\right)^2 + \tfrac{1}{3}\left(\frac{2k_1}{k_2}\xi\rho\right)^3 - \ldots.\right\} \approx \frac{k_1}{k_2}\xi^2\rho^2$$

Hence, $d\rho/di$ can be approximated by:

$$\frac{d\rho}{di} = -\xi^2\left(\rho(\rho V-1)+\frac{k_1}{k_2}\rho^2\right) \qquad \rho V > 1 \tag{3.5.13}$$

$$\frac{d\rho}{di} = -\xi^2\frac{k_1}{k_2}\rho^2 \qquad \rho V \le 1$$

For $\rho V=1$, there is only one atom left in the combination volume V and direct combination stops. The number of ions i incident on the track region with effective radius r_{eff} can be expressed in terms of the ion fluence φ (see figure 3.5.2): $i=A\varphi$ with $A=\pi r_{eff}^2/\sin\alpha$ where α is the angle of incidence. Hence, we substitute $di=Ad\varphi$ in order to obtain an expression that gives ρ as a function of ion fluence.

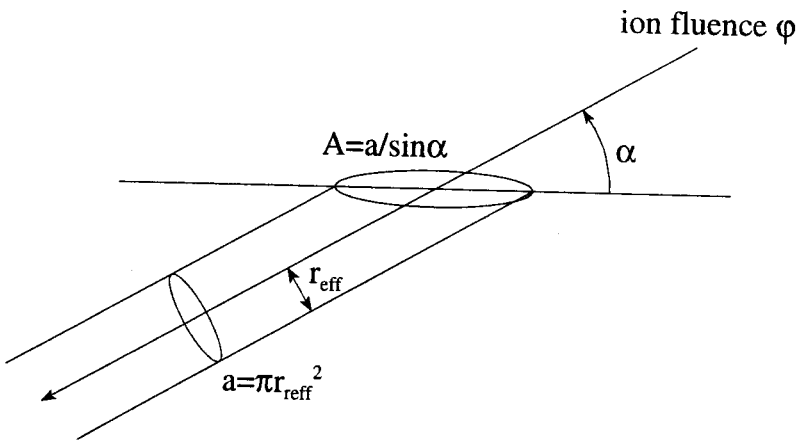

Figure 3.5.2: *The number of ions that have passed through the same track is equal to the product Aφ, where A is the cross section of the track and the surface of the sample.*

The solution to equation 3.5.13 can be found by separation of variables and integration:

$$\rho(\varphi) = \frac{1}{V + \frac{k_1}{k_2} + \left(\frac{1}{\rho(0)} - \left(V + \frac{k_1}{k_2}\right)\right)e^{-\xi^2 A\varphi}} \qquad \rho V > 1$$

$$\rho(\varphi) = \frac{1}{\frac{k_1}{k_2}\xi^2 A\varphi + C} \qquad \rho V \leq 1 \tag{3.5.14}$$

where $\rho(0)$ is the initial hydrogen concentration and A is the effective track area. The integration constant C must fulfill the condition that the two curves match when $\rho V=1$ (smooth matching is guarantied, as can be seen from equation 3.5.13):

$$C = V - \frac{k_1}{k_2}\ln\left(\frac{V + k_1/k_2 - 1/\rho(0)}{k_1/k_2}\right) \tag{3.5.15}$$

A comparison of $\rho(\varphi)$ calculated from equations 3.5.11 (numerically) and 3.5.14 is shown in figure 3.5.3.

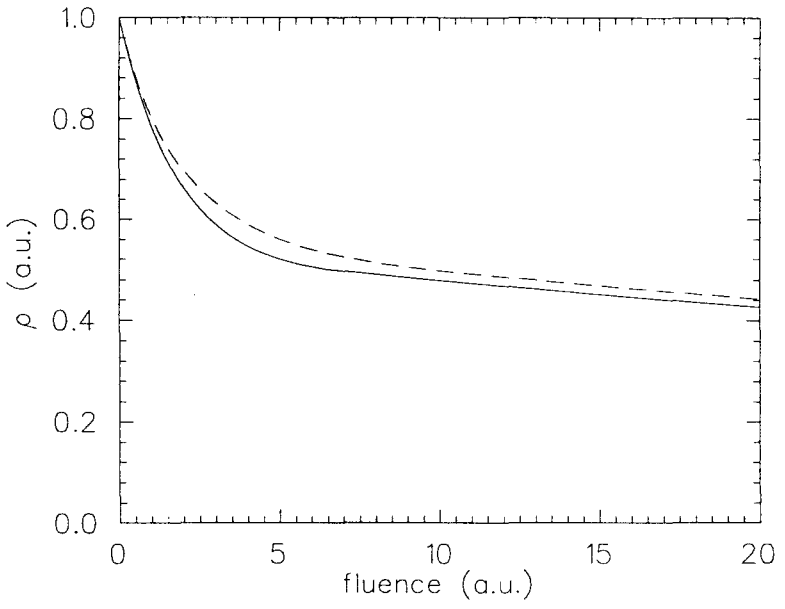

Figure 3.5.3: *comparison of $\rho(\varphi)$ as calculated numerically from equation 3.5.11 (solid line) and a calculation using equation 3.5.14.*

Equation 3.5.14 was derived under the assumption that $\xi<<1$. This assumption can be justified by regarding the experimental hydrogen loss curves that will be presented in chapter 5 of this work.

In the case of 2 MeV He irradiation, when hydrogen loss is most severe, the hydrogen concentration drops to approximately 80% of the initial value at a deposited fluence of $1\cdot10^{15}/cm^2$, which corresponds to roughly 200 ions that have passed trough the same track (with r_{eff}=1.3 nm and a 15° angle of incidence).

We regard direct combination (equation 3.5.6) only, which is dominant at low ion fluence. Taking $(d\rho/di)/\rho \approx -0.2\rho(0)/(0.8\rho(0))=-0.25$ for 200 ions, gives $\xi^2(\rho V-1)\approx 1.25\cdot10^{-3}$ for 1 ion. As will be shown later on, the combination volume V is approximately 50 $Å^3$ and the factor $(\rho V-1)$ can be estimated to be $(\rho V-1)\approx 1$ (the initial hydrogen density in the porphyrin material is 31at/nm^3). This gives an order of magnitude estimate $\xi\approx 0.05$.

CHAPTER 4: Experiments

The application of IBA techniques for the investigation of porphyrin layers is limited by the loss of elements under ion irradiation. This effect can be studied by measuring the content of a certain element as a function of deposited ion fluence.
At the EUT cyclotron laboratory, ERDA experiments have been performed with 2, 4, 7.6 and 12.1 MeV ^{4}He beams in order to determine the dependence of hydrogen evolution on the kinetic energy of the projectiles. The carbon content could be monitored at 4 and 12.1 MeV by means of RBS and PSD-ERDA measurements, respectively.
Additional ERDA hydrogen loss experiments have been performed at the UU van der Graaff laboratory using 4 and 10 MeV ^{12}C beams.
In paragraph 4.1, a description of the composition of the porphyrin samples is given. The experimental setups are discussed in paragraph 4.2.

4.1 Sample composition

The porphyrin layers were grown by electropolymerization on ITO (IndiumTinOxide) coated glass. The thickness of the porphyrin layers varies roughly from 20 to 200 nm. The conducting ITO layer serves as the working electrode in the electropolymerization process. The ITO layer is approximately 70 nm thick and its composition is In_2O_3:Sn. Only a very small quantity of tin is present as doping. ITO is used for its transparency which allows optical analysis of the porphyrin layer. The substrate is 1 mm thick soda lime glass with the approximate composition $Si_{10}O_{24}Na_5Ca_{1.5}$.
The porphyrins that were investigated were PalladiumTetra-Hydroxyphenylporphyrins with molecular composition $PdC_{44}H_{28}N_4O_4$. The structure of the porphyrin molecule is depicted in figure 4.1.1.

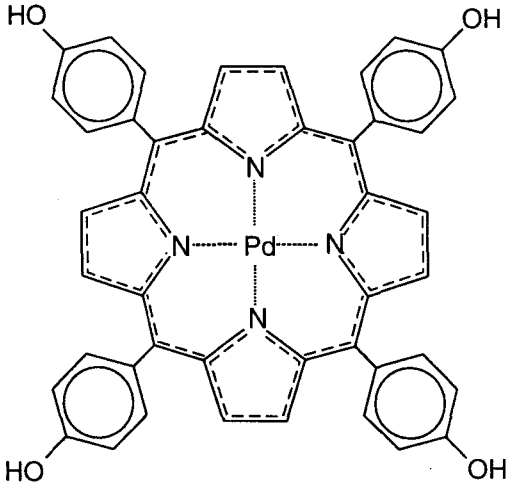

Figure 4.1.1: *the PalladiumTetra-Hydroxyphenylporphyrin molecule.*

The carbon atoms, which occupy all corner positions in the molecule, are omitted in figure 4.1.1. Apart from the four hydrogen atoms in the hydroxy groups, sixteen more H atoms are bound to the phenyl rings and eight to the central skeleton. The dashed lines represent the system of delocalized π-electrons [BAR95].

4.2 The cyclotron laboratory at EUT

4.2.1 Overview of the laboratory

An AVF(Azimuthal Varying Field)-cyclotron, which can accelerate protons and alpha particles to energies between 2 and 30 MeV, is used to produce the ion beam (see figure 4.2.1). The beam is directed to the various IBA setups by means of a beam guidance system that contains numerous bending magnets, magnetic lenses (i.e. quadrupoles) and slits. There are four setups where different types of IBA techniques are practised, among which are RBS(-channeling), ERDA, and PIXE (Particle Induced X-ray Emission). A switcher magnet bends the beam towards the desired location.

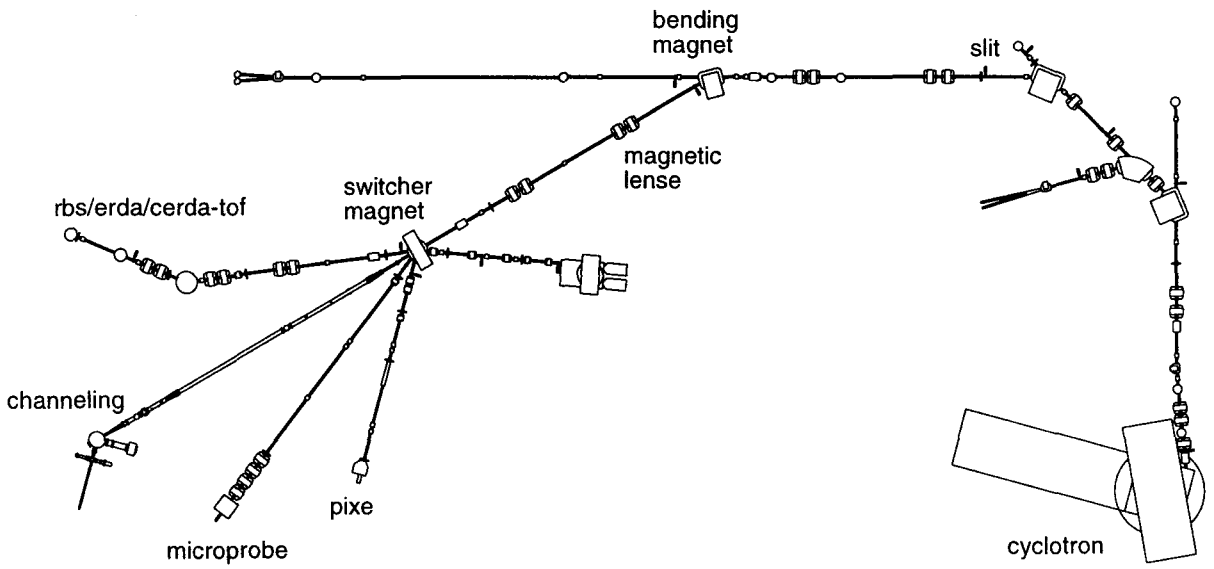

Figure 4.2.1: *overview of the cyclotron laboratory at EUT.*

All experiments were performed using the RBS/ERDA/CERDA-TOF setup, which is discussed in paragraph 4.2.2.

4.2.2 The RBS/ERDA/CERDA-TOF setup

The main component of the setup is the scattering chamber, in which the samples and the detectors are located (see figure 4.2.2). The vacuum in the chamber is maintained at approximately $5 \cdot 10^{-6}$ mbar.

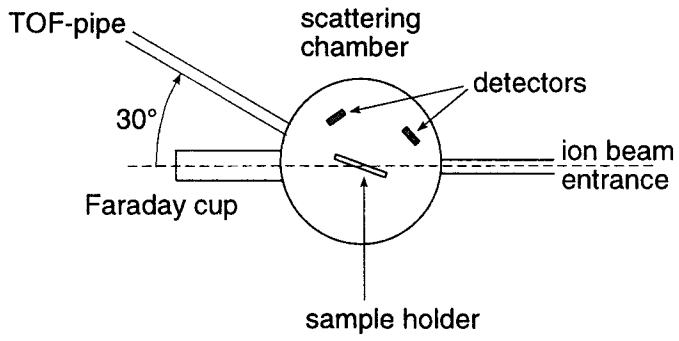

Figure 4.2.2: *schematic representation of the RBS/ERDA/CERDA-TOF setup. The TOF-pipe is partially omitted since no use was made of the CERDA-TOF technique.*

The ion beam enters the scattering chamber on the right hand side. The sample is placed in the sample holder located in the centre. The sample holder can be rotated in the horizontal plane to adjust the angle of incidence (accuracy $\approx 1°$).
The detectors that are used for standard energy measurements of scattered or recoiled particles are Canberra PIPS (Planar Implanted Passivated Silicon) detectors. The operation principals of these detectors will not be discussed here, the reader is referred to [KNO79]. For PSD (Pulse Shape Discrimination) measurements, a low resistivity PIPS detector with a very thin depletion layer is used (see paragraph 2.5.1).
The detectors can be placed at arbitrary angles w.r.t. the ion beam entrance (accuracy $< 0.2°$) on either the top or bottom plate of the scattering chamber. The plates can be rotated independently while maintaining the vacuum in the chamber, providing the possibility to alter the detection angles during a measuring session.
At the left hand side of the chamber, directly opposed to the ion beam entrance, a Faraday cup is located by means of which the beam current can be measured (see appendix 2).
The TOF pipe, which enables CERDA-TOF measurements (see paragraph 2.5.2), is attached to the scattering chamber at a 30° angle relative to the ion beam entrance. It is partially omitted in figure 4.2.2 since the CERDA-TOF technique was not used in the experiments described in this work.

4.2.3 Hydrogen and carbon evolution measurements

Ion beam induced hydrogen depletion from porphyrin layers was studied by means of ERDA measurements under various irradiation conditions. The porphyrins were exposed to ^{4}He irradiation with beam energies of 2, 4, 7.6 and 12.1 MeV. The hydrogen content as a function of ion fluence was determined by measuring the hydrogen recoil yield in subsequent time intervals: every 10 seconds a list mode data file (see [SIM94]) was written that contained all events that were measured during that time.
A stopper foil was placed in front of the ERDA detector to stop forwardscattered projectiles that would otherwise distort the H-recoil spectrum. The foil composition and thickness were chosen such that all ^{4}He particles were stopped while recoiled hydrogen could pass through.
In order to determine the ion fluence, the beam current and the beamspot area had to be known. The current could be measured on the Faraday cup (see appendix 2) before starting an experiment. The beamspot area could be obtained by measuring the area of the blackened region on the sample resulting from the ion bombardment (see appendix 1).
By measuring the hydrogen yield as a function of time, a fluence dependent plot could be obtained. However, the beam current was not completely constant during the experiments and a correction had to be made for current fluctuations. This could be done by performing a simultaneous RBS measurement. The RBS yield of a stable (substrate) element, for example In, could then be used as a measure of the ion dose.
The orientation of the sample and the angular positions of the RBS and ERDA detectors are depicted in figure 4.2.2.

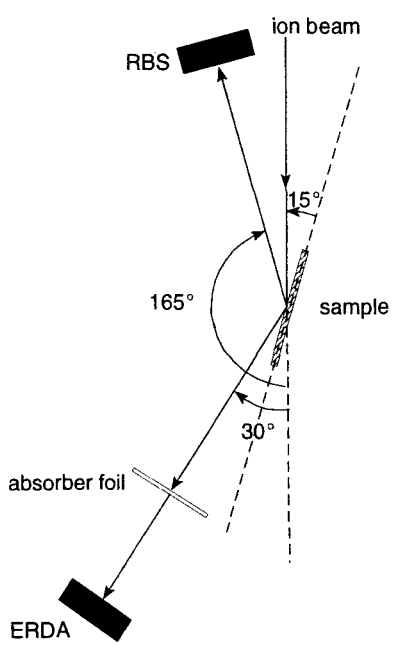

Figure 4.2.2: *scattering geometry for hydrogen evolution experiments.*

Using a 4 MeV ^{4}He beam it was possible to study carbon evolution from the porphyrin layers simultaneously because of the resonance in the ^{4}He-^{12}C scattering cross section at this beam

energy. Due to this resonance, the RBS detection sensitivity for carbon (at a 165° backscattering angle) was enhanced to roughly seven times the Rutherford value [LEA89].
At 12.1 MeV beam energy, another resonance occurs in the cross section for ^{4}He-^{12}C scattering. However, RBS measurements could not be used to determine the carbon content due to the large irregular background arising from resonant ^{4}He-^{28}Si scattering from the glass substrate. Instead, carbon recoils could be detected using the PSD-ERDA technique. A PSD detector was added to the setup according to figure 4.2.3.

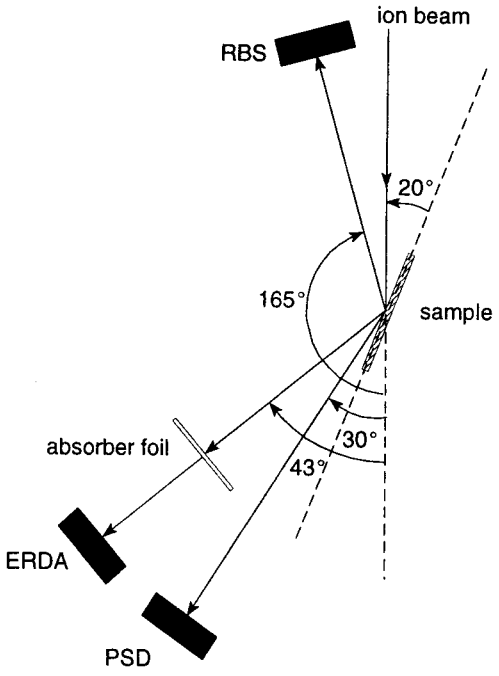

Figure 4.2.3: *scattering geometry for combined RBS, ERDA (H-detection) and PSD-ERDA (C-detection) measurements.*

4.3 The van der Graaff laboratory at UU

4.3.1 The magnetic spectrograph

Two van der Graaff accelerators are available at the laboratory: a 3 MV single ended accelerator and a 6.5 MV tandem accelerator. Beams of many different ionic species (for example He, C and Ag) can be provided by these facilities. As at EUT, the ion beam is guided to the desired experimental setup by a beam guidance system.
The experiments were performed using the magnetic spectrograph setup. The setup is shown schematically in figure 4.3.1.

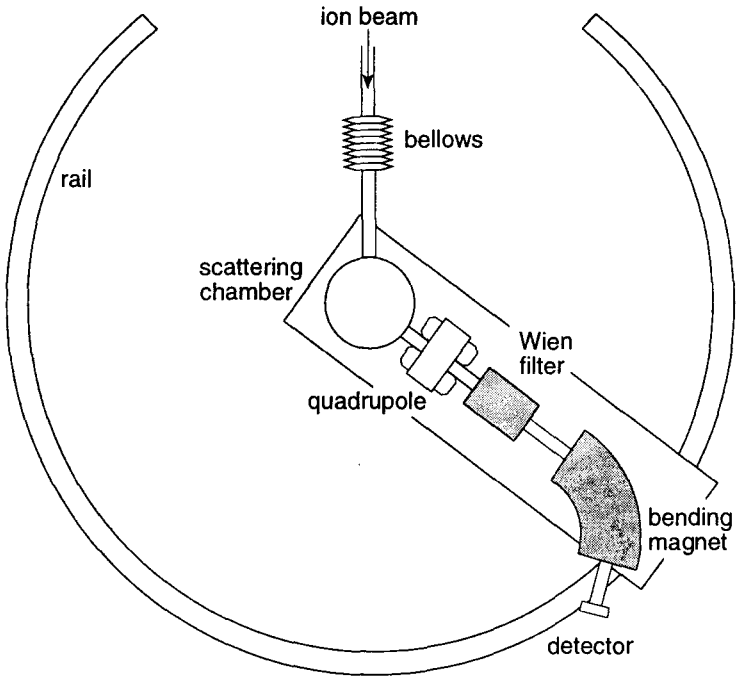

Figure 4.3.1: *the magnetic spectrograph setup at the UU van der Graaff laboratory.*

The ion beam impinges on the sample that is located in the scattering chamber. A specific scattered or recoiled particle is selected by means of the magnetic spectrograph, which consists of three main components: a quadrupole lens, a Wien filter and a bending magnet. The Wien filter, a crossed electric and magnetic field, selects particles with a specific velocity (see figure 4.3.2).

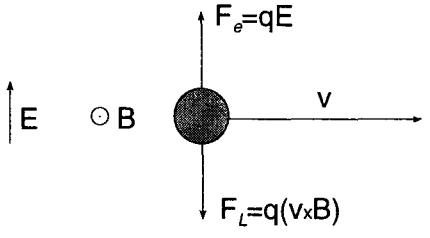

Figure 4.3.2: *operation principle of a Wien filter.*

The electrostatic force F_e and the Lorentz F_L force cancel when v=E/B and only particles with velocity v can pass unhindered. A momentum selection takes place when the particles pass through the field of the bending magnet: mv=qBr, where r is the radius of curvature. The magnetic spectrograph thus provides the possibility to select a particle on its energy, mass and charge.
The detection angle can be altered by rotation of the entire setup, which is mounted on a circular rail and connected to the beam guidance system by a number of flexible bellows.
The particles that are selected by the spectrograph strike a two dimensional position sensitive detector. The horizontal position is a measure of the energy of a particle, the vertical position gives the angle at which the particle left the scattering plane (for more details, see [ARN96]).

4.3.2 Hydrogen loss experiments

The porphyrin samples were bombarded with 4 MeV and 10 MeV ^{12}C beams. Again hydrogen evolution was studied by means of ERDA experiments performed with the magnetic spectrograph setup. The scattering geometry is depicted in figure 4.3.3.

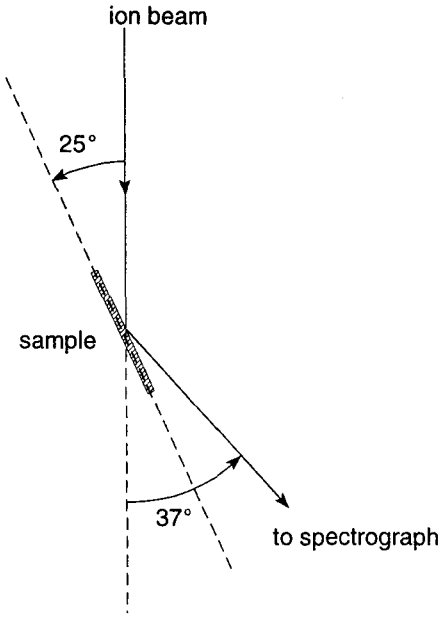

Figure 4.3.3: *scattering geometry of the hydrogen ERDA measurements.*

Detection of recoiled hydrogen was accomplished by adjusting the settings of the spectrograph to H^+. The deposited ion dose was monitored by measuring the backscattering yield on a vibrating gold string, which is located in the beam guidance system several meters away from the scattering chamber. The string sweeps in and out of the ion beam with a fixed frequency and hence the scattering yield is a measure of the ion dose.

CHAPTER 5: Results

5.1 Hydrogen loss from porphyrin layers under 2, 4 , 7.6 and 12.1 MeV ^{4}He irradiation

5.1.1 Hydrogen-ERDA measurements

To accomplish the detection of hydrogen recoils without a background arising from scattered ^{4}He particles, an absorber foil was placed in front of the detector in all hydrogen-ERDA (H-ERDA) experiments. The angle of incidence was kept constant at 15° w.r.t. the sample surface. The other experimental parameters are given in table 5.1.1.

experiment number	ion beam	absorber foil	recoil angle	beam current (nA)	beamspot area (mm^2)	film thickness (nm)
1	2 MeV He^+	8 μm Al	30°	12	14	200
2	2 MeV He^+	8 μm Al	30°	48	14	20
3	4 MeV He^+	15.8 μm Mylar	30°	93	5.7	20
4	7.6 MeV He^{2+}	20 μm Ag	30°	47	11	20
5	12.1 MeV He^{2+}	45 μm brass	25°	76	7.6	100
6	12.1 MeV He^{2+}	45 μm brass	25°	73	7.5	40

Table 5.1.1: *experimental parameters of the hydrogen-ERDA experiments.*

The measured H-ERDA spectra are shown in figures 5.1.1 to 5.17. The energy axis was calculated theoretically for each spectrum in the following manner:

- the recoil energy for surface hydrogen was calculated using the kinematic factor (equation 2.2.4);
- the energy loss in the absorber foil was estimated from: $E_{loss}=S(E_{mean})d$, where $S(E_{mean})$ is the stopping power at mean energy (mean energy approximation, see [FEL86]) and d is the absorber foil thickness. S(E) was obtained from a table generated by the computer program TRIM;
- the offset of the energy-calibration was assumed to be 0.

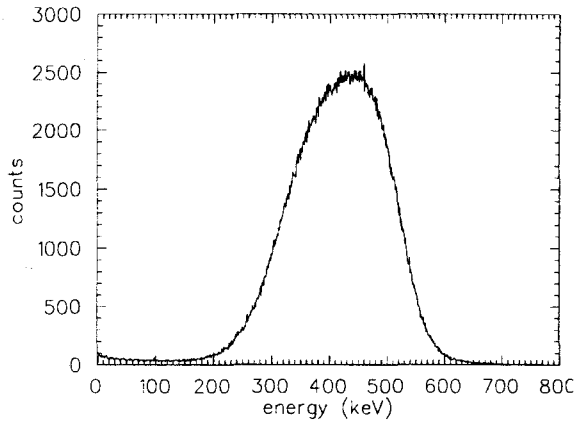

Figure 5.1.1: *2 MeV ^{4}He H-ERDA spectrum, experiment number 1.*

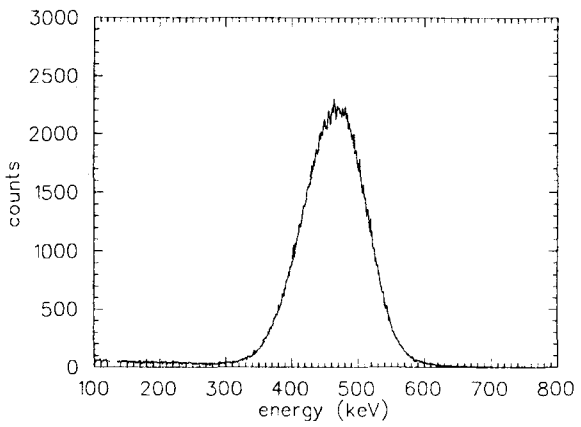

Figure 5.1.2: *2 MeV ^{4}He H-ERDA spectrum, experiment number 2.*

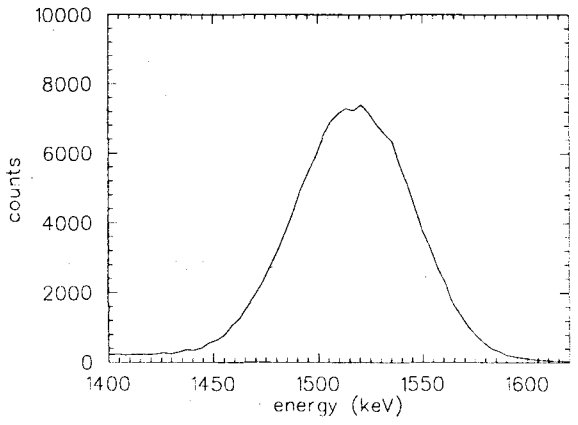

Figure 5.1.3: *4 MeV ^{4}He H-ERDA spectrum, experiment number 3.*

The 2 and 4 MeV ^{4}He H-ERDA spectra (experiments 1, 2 and 3) feature a single peak that arises from hydrogen contained in the porphyrin layer. Comparing the two 2 MeV ^{4}He H-ERDA spectra (figures 5.1.1 and 5.1.2), one notices that figure 5.1.1 shows a broader hydrogen peak than figure 5.1.2. This is due to different porphyrin film thicknesses: the spectrum that shows the broadest hydrogen peak corresponds to the sample with the thickest porphyrin layer. Unfortunately, an accurate depth scale can not be obtained from the energy axis when using an absorber foil in H-ERDA experiments: the foil causes a significant spread in the kinetic energy of the H-recoils that are passing through (straggling, see [FEL86]).

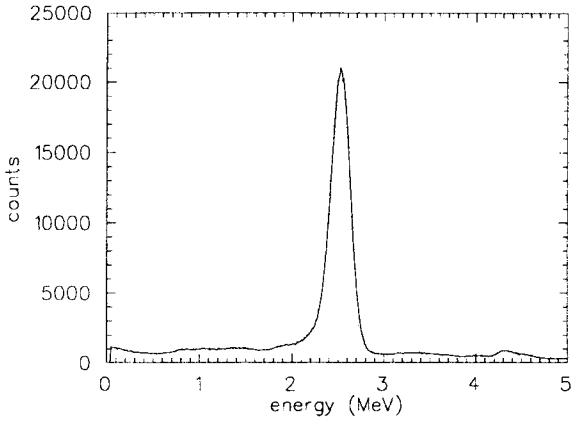

Figure 5.1.4: *7.6 MeV ^{4}He H-ERDA spectrum, experiment number 4.*

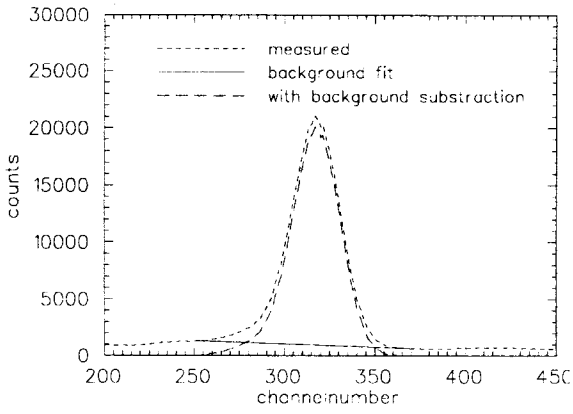

Figure 5.1.5: *7.6 MeV ^{4}He H-ERDA spectrum (Figure 5.1.4) with background substraction (see text).*

A background resulting from (^{4}He,p) reactions on substrate elements appears in the spectra of 7.6 and 12.1 MeV ^{4}He H-ERDA experiments. At such high beam energies, proton producing nuclear reactions between an impinging ^{4}He nucleus and a target nucleus as, for example, ^{28}Si or ^{29}Si are quite common. This is a drawback of using high energy ^{4}He ERDA for the profiling of hydrogen in thin films deposited on a glass substrate. A closer look at the origin of the background in 12.1 ^{4}He H-ERDA spectra is presented in paragraph 5.1.6.
The background-correction that was applied is described in paragraph 5.1.5.

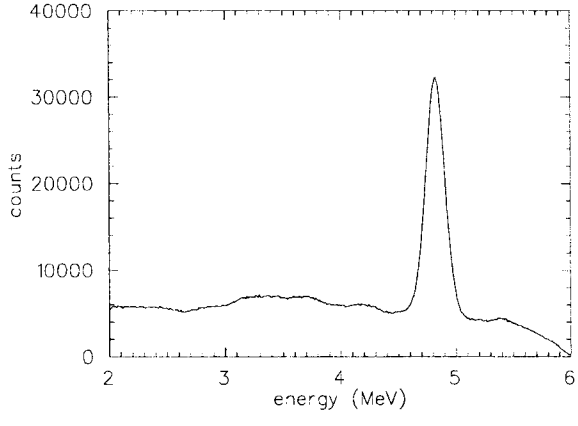

Figure 5.1.6: *12.1 MeV ^{4}He H-ERDA spectrum, experiment number 5.*

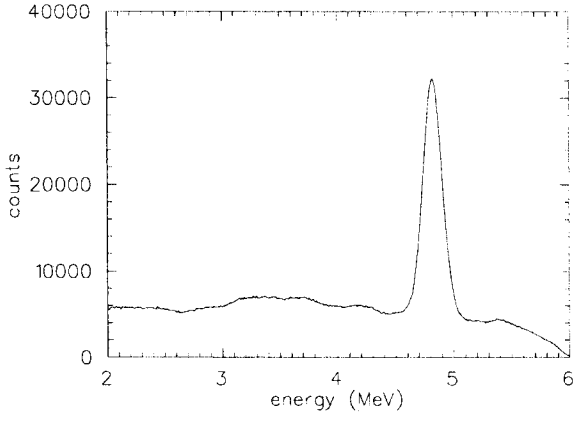

Figure 5.1.7: *12.1 MeV ^{4}He H-ERDA spectrum, experiment number 6.*

The recoil angle ϕ was adjusted to 25° in the 12.1 MeV ^{4}He H-ERDA experiments (ϕ was 30° in all other cases) in order to increase the detection sensitivity for hydrogen. Various hydrogen detection experiments were performed with different recoil angles (ranging from 15° to 40°) and otherwise similar experimental parameters with the aim to find an optimum (see figure 5.1.8).

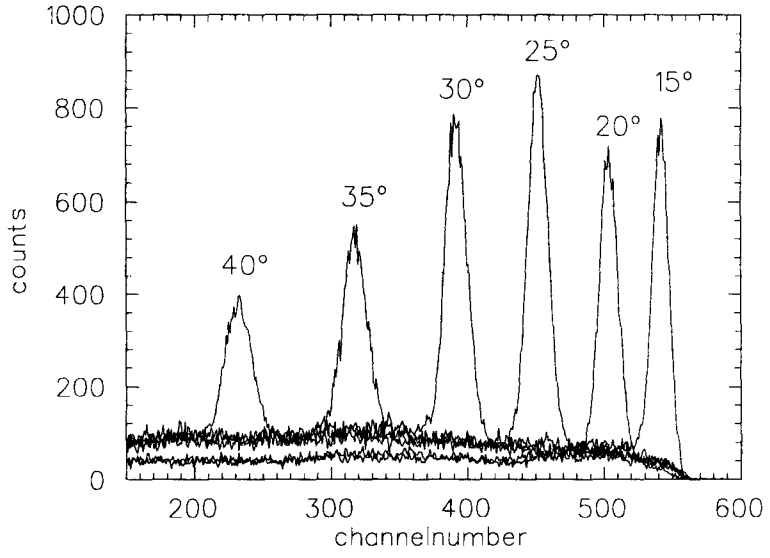

Figure 5.1.8: *12.1 MeV ^{4}He H-ERDA spectra measured with various different recoil angles ϕ ranging from 15° to 40°. The value of ϕ is displayed directly over the corresponding hydrogen peak.*

Since these experiments were performed using a porphyrin sample, the irradiation time was kept short (1 minute) to minimize hydrogen loss which would complicate comparison of the spectra. Judging from figure 5.1.8, a recoil angle ϕ=25° gives the best detection sensitivity.
The spectra shown in figures 5.1.1 to 5.1.7 contain the total hydrogen yield and give no information on hydrogen loss during irradiation. However, hydrogen loss becomes evident when the spectra are split up in small fragments corresponding to subsequent time intervals. Plotting these fragmented spectra as a function of time results in 3-dimensional pictures such as shown in figures 5.1.9 and 5.1.10 (corresponding to experiment number 2). Instead of time the "filenumber" parameter is used, which is essentially the same since each file contains the events that were detected during ten seconds (see paragraph 4.2.3).

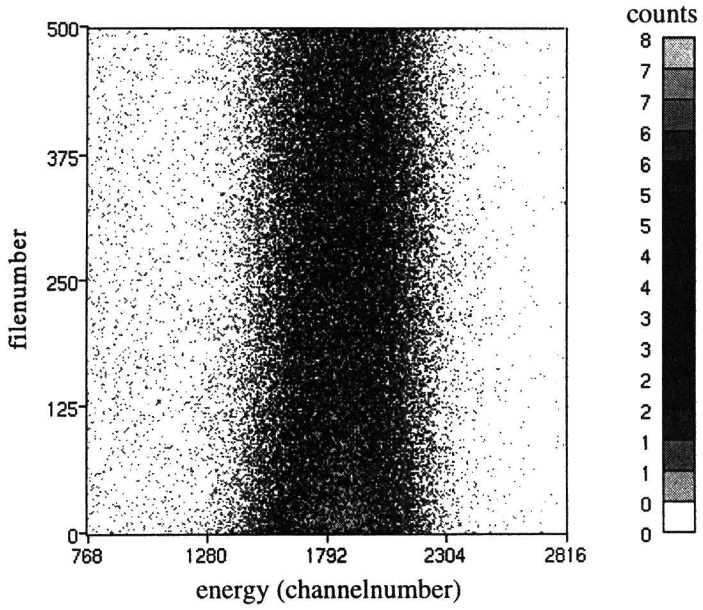

Figure 5.1.9: *H-ERDA energy spectra (experiment number 2) plotted as a function of filenumber, the grey scale indicates the number of counts.*

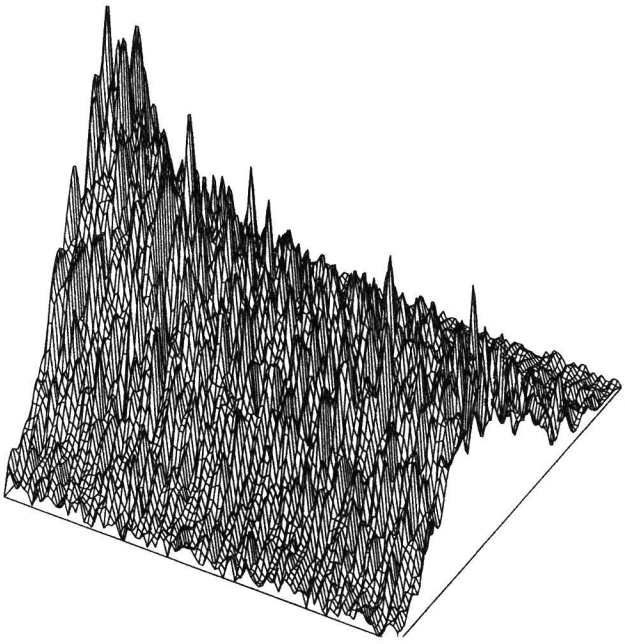

Figure 5.1.10: *ERDA spectra (experiment number 2) plotted as a function of filenumber. The horizontal plane is formed by the energy axis and filenumber axis. The energy increases from back to front, the filenumber from left to right.*

The loss of hydrogen is illustrated best by figure 5.1.10, where the decreasing count rate in time is clearly visible. An even more demonstrative picture is obtained when the hydrogen yield is projected on the filenumber (i.e. time) axis, as shown in figure 5.1.11.

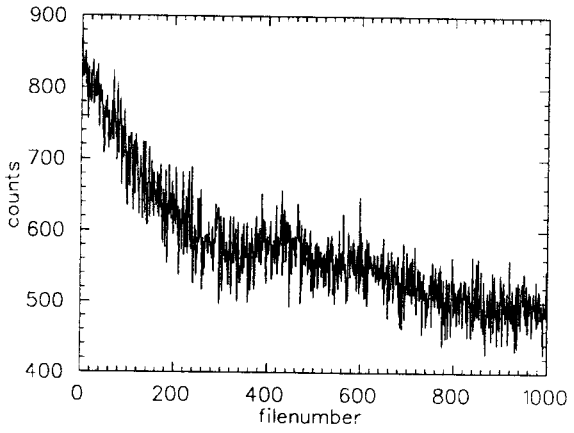

Figure 5.1.11: *hydrogen yield as a function of filenumber, experiment number 1.*

The plot obtained from experiment number 1 is shown here to demonstrate the effect of current fluctuations: the curve features a distinct "lump" at filenumber 400. The procedure that was applied to correct for the current variations is described in paragraph 5.1.3.

5.1.2 Simultaneous RBS experiments

In order to be able to monitor the beam current fluctuations, RBS measurements were performed simultaneously with the H-ERDA experiments (see paragraph 5.1.3 on how the monitoring works). Backscattered ^{4}He particles were detected at 165° resulting in the RBS spectra shown in figures 5.1.12 to 5.1.20.

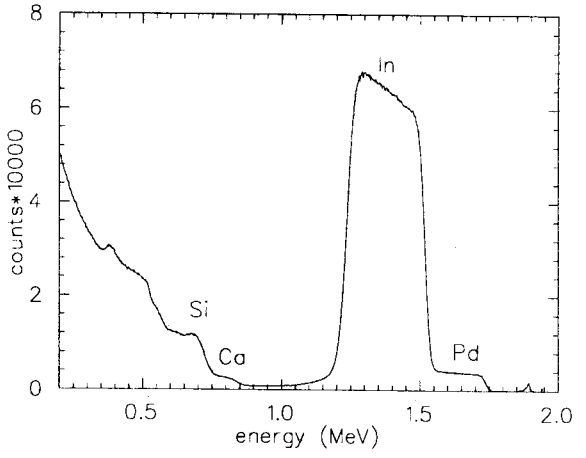

Figure 5.1.12: *2 MeV ^{4}He RBS spectrum, experiment number 1. The features corresponding to the elements Pd (located in the porphyrin layer), In (in ITO layer), Ca and Si (in the glass substrate) are easy to distinguish.*

The various peaks and steps in the 2 and 4 MeV RBS spectra could be identified by means of computer simulation of the RBS experiment using the program RUMP [DOO90]. The proper energy axis was also deduced from the simulation. The measured and simulated spectra are plotted together in figures 5.1.13 and 5.1.16 for the 2 and 4 MeV experiments, respectively.

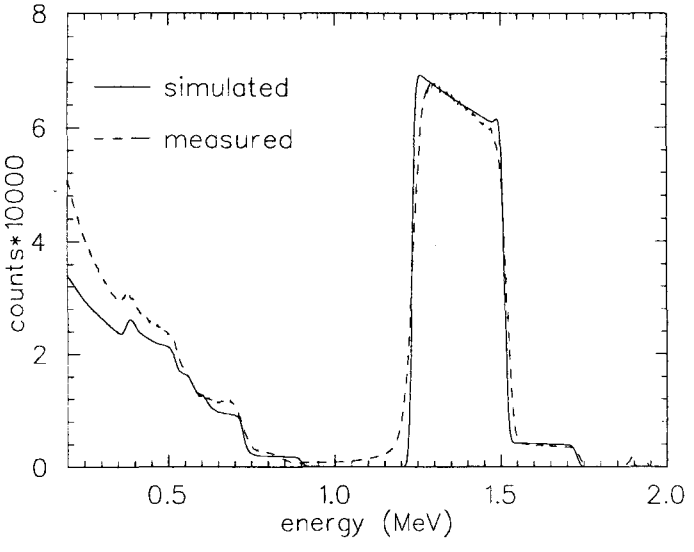

Figure 5.1.13: *comparison of measured and simulated 2 MeV ^{4}He RBS spectra (experiment number 1).*

The 2 MeV ^{4}He RBS spectrum shows very clear features of the heavy elements Pd (located in the porphyrin layer) and In (in ITO layer), the light elements C, O and N, however, are not easy to distinguish (see figure 5.1.14).

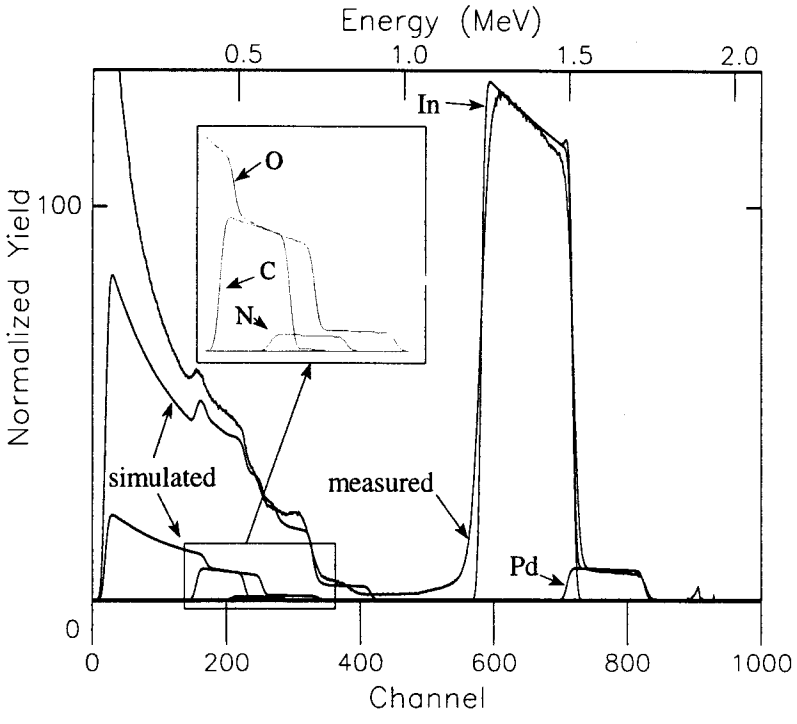

Figure 5.1.14: *comparison of measured and simulated 2 MeV ^{4}He RBS spectra (experiment number 1). The contribution of the elements Pd, C, N (all located in the porphyrin layer), O (present in the porphyrin and ITO layer as well as in the glass substrate) and In (in ITO layer) to the total simulated spectrum are shown explicitly. The separate contributions from Si, Ca and Na (present in the glass substrate) are omitted for clarity.*

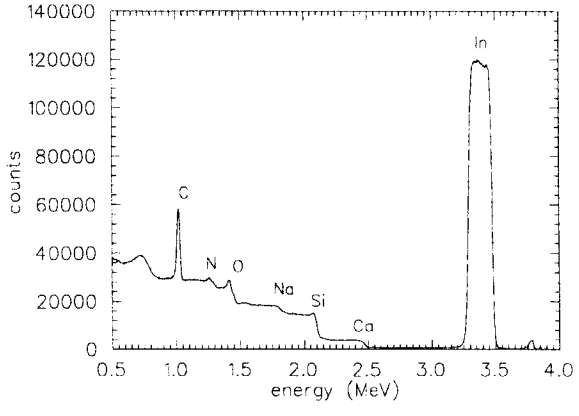

Figure 5.1.15: *4 MeV ^{4}He RBS spectrum, experiment number 3.*

In the 4 MeV ^{4}He RBS spectrum (figure 5.1.15), the In peak is still very pronounced. The Pd feature is hardly visible in figure 5.2.2 because of the thin porphyrin film thickness.

Due to a resonance in the ^{4}He-^{12}C scattering cross section near 4 MeV beam energy, the detection sensitivity for carbon is enhanced considerably which can be seen from the distinct C-peak. The cross sections for scattering of ^{4}He on ^{16}O and ^{14}N are also non-Rutherford, leading to an increased detection yield. To allow for accurate simulation of the 4 MeV ^{4}He RBS experiment (see figure 5.1.16), RUMP was complemented with non-Rutherford cross section data for C, O and N.

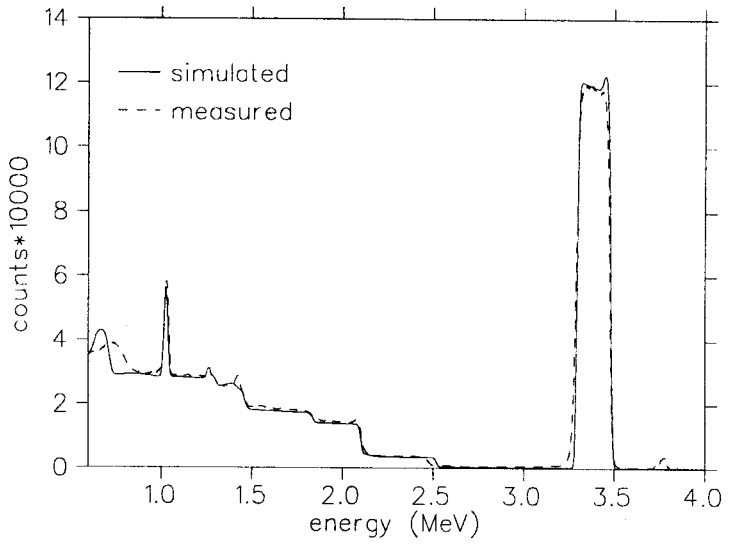

Figure 5.1.16: *comparison of measured and simulated 4 MeV ^{4}He spectra, experiment number 3.*

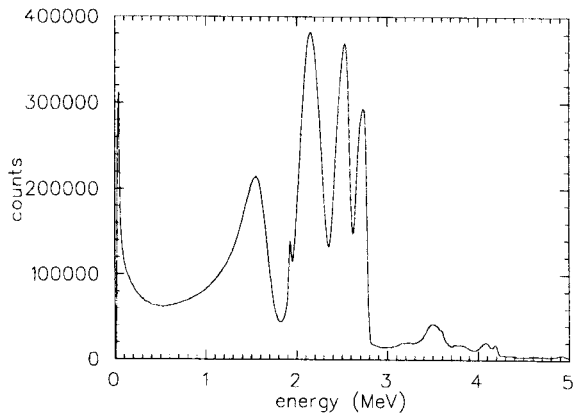

Figure 5.1.17: *7.6 MeV ^{4}He RBS spectrum, experiment number 4.*

At 7.6 and 12.1 MeV ^{4}He energy, the scattering cross sections for most elements in the sample are non-Rutherford and simulation of the RBS experiments becomes practically impossible. However, the RBS measurements are still suitable for their purpose: to monitor the beam current. The four large peaks in the energy region from 1 to 3 MeV in the 7.6 MeV ^{4}He RBS spectrum (figure 5.1.17) stem from resonant ^{4}He-^{16}O scattering, as can be seen by comparison with figure 5.1.18.

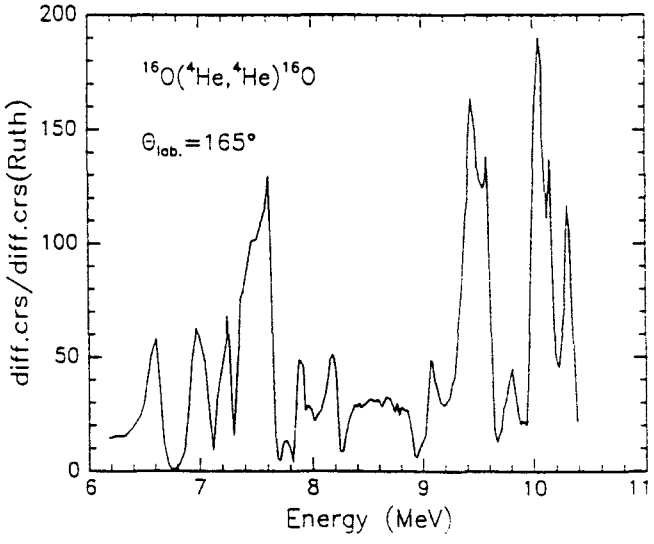

Figure 5.1.18: *the ratio of measured differential cross sections to Rutherford cross sections for ^{16}O(^{4}He,^{4}He)^{16}O scattering at a 165° laboratory angle as a function of ^{4}He kinetic energy.*

The porphyrin layer only contains a small fraction of oxygen (4 oxygen atoms on a total of 81, see paragraph 4.1) and hence the corresponding peak is overwhelmed by the large features due to scattering from substrate-oxygen.

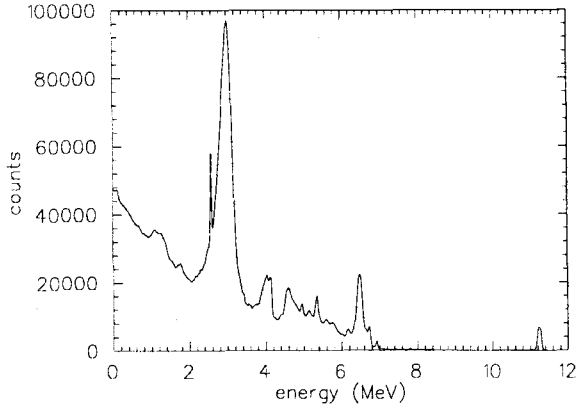

Figure 5.1.19: *12.1 MeV ^{4}He RBS spectrum, experiment number 5.*

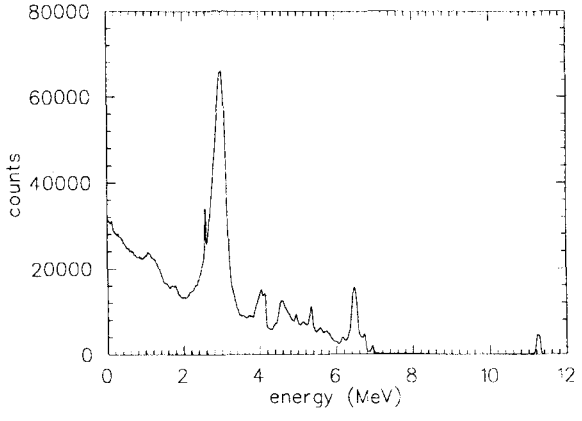

Figure 5.1.20: *12.1 MeV ^{4}He RBS spectrum, experiment number 6.*

The large peak at approximately 3 MeV in figures 5.1.19 and 5.1.20 arises from resonant scattering of ^{4}He particles from carbon.

5.1.3 The normalization procedure and calculation of the ion fluence

The beam current was monitored by means of the simultaneous RBS experiments. With RBS, the backscattering yield from heavy, stable (i.e. non-vanishing) substrate elements was obtained. The corresponding count rate is a direct measure of the beam current. The RBS spectra can be plotted as a function of filenumber f, and a projection of a region of interest on the f-axis can be made. In figure 5.1.21, the f-axis projection of the indium peak in figure 5.1.12 is shown. As in figure 5.1.5, the "lump" at filenumber 400 is visible.

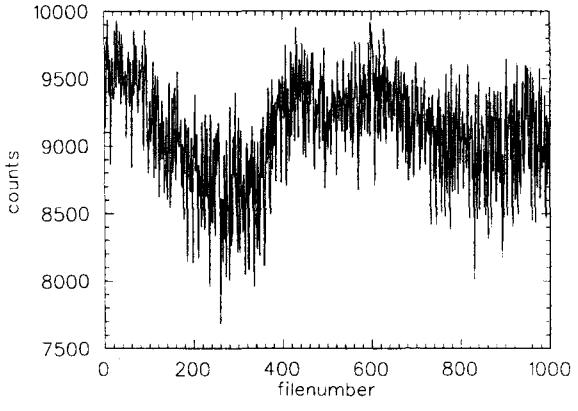

Figure 5.1.21: *projection of the RBS In-yield on the f-axis, experiment number 1.*

The time dependent relative hydrogen content can now be obtained as follows. The number of hydrogen counts Y_H in a certain file depends on the hydrogen coverage (atoms per unit area) H at the time the file was written and the number of ions Q deposited during the measuring time: $Y_H \propto HQ$. Due to beam current fluctuations, the number of incident ions per file Q is not a constant. However, the indium detection yield Y_{In} also depends on Q according to $Y_{In} \propto InQ$, where In is the indium coverage which is constant during the experiment. Hence, Q can be eliminated by calculating the normalized hydrogen yield Y_H/Y_{In} which only depends on the hydrogen coverage H in the porphyrin film: $Y_H/Y_{In} \propto (HQ)/(InQ) \propto H$. A plot of the normalized hydrogen yield Y_H/Y_{In} as a function of filenumber is shown in figure 5.1.22.

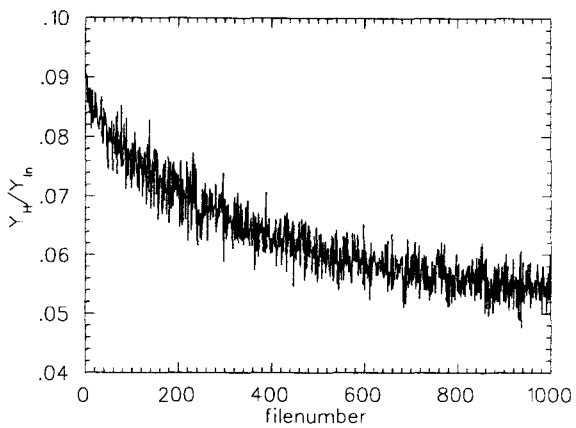

Figure 5.1.22: *the normalized hydrogen yield as a function of filenumber, experiment number 1. The normalized yield no longer depends on beam current fluctuations.*

The result of the normalization procedure is clear: the "lump" that was present in figure 5.1.11 is gone. Still, the filenumber axis has to be transformed to a fluence axis to obtain the desired graph of relative hydrogen content vs. ion fluence. This can be done in the following way:

- the mean indium yield per file is determined over an interval at the beginning of the curve where it is approximately constant, in the case of figure 5.1.21 that is from files 1 to 50;
- this mean yield Y_{mean} corresponds to the initial beam current I_b according to $Y_{mean} \propto (I_b/q)t$, where q is the charge of the ^4He particle ($1.6 \cdot 10^{-19}$ C for 2 and 4 MeV beam energy, $3.8 \cdot 10^{-19}$ C for 7.6 and 12.1 MeV beams) and t is the measurement time per file (10 s). The initial beam current is measured using the Faraday cup (see appendix 2);
- for a certain filenumber f, the deposited dose D follows from $D = (I_b/q)tY_{sum}(f)/Y_{mean}$, where $Y_{sum}(f)$ is the indium yield summed over files 0 to f. Finally, the fluence F is obtained from F=D/O. The beamspot area O can be determined according to the procedure described in appendix 1.

5.1.4 The hydrogen contents as a function of ion fluence

The relative hydrogen content H(F)/H(0) (relative to the initial content in the undamaged porphyrin layer) is obtained by dividing the quantity $Y_H/Y_{In}(F)$ through $Y_H/Y_{In}(0)$. Plots of the relative hydrogen content as a function of ^4He fluence are shown in figures 5.1.23 to 5.1.32. The average was taken over each subsequent pair of points to reduce the number of points in the figures and to diminish the statistical spread. In each plot, a smooth line corresponding to a fit obtained from the theoretical hydrogen loss model (equation 3.5.14) described in paragraph 3.5 is shown. The fitting method is described in appendix 3.
The scattering of particles can be treated as a "random" process that can be described by a Poisson distribution. The standard deviation σ is then given by the square root of the number of counts per point. In each plot, an error bar is drawn that represents such a standard deviation. The number of counts at the high fluence end of each plot was considered in the calculation of σ.

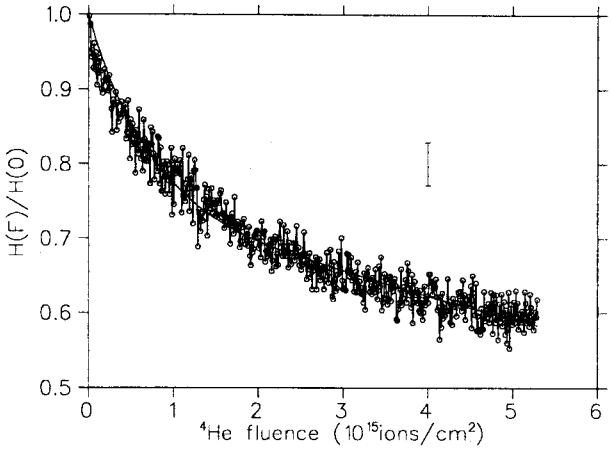

Figure 5.1.23: *relative hydrogen content as a function of 2 MeV ^{4}He fluence, exp. number 1.*

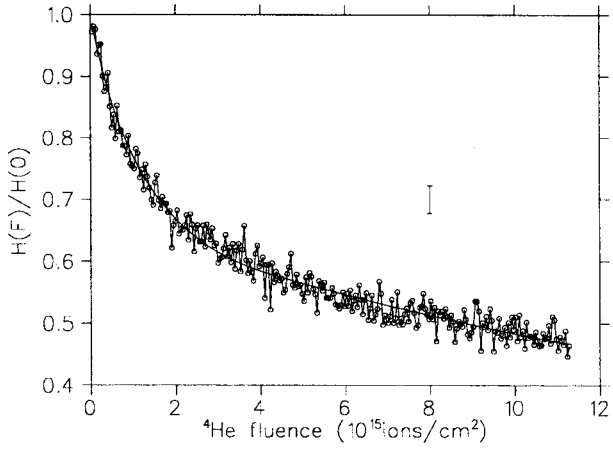

Figure 5.1.24: *relative hydrogen content as a function of 2 MeV ^{4}He fluence, exp. number 2.*

To compare the two 2 MeV ^{4}He induced hydrogen loss curves, figures 5.1.23 and 5.1.24 are drawn in one picture in figure 5.1.25. As is to be expected, the curves are similar within reasonable accuracy.

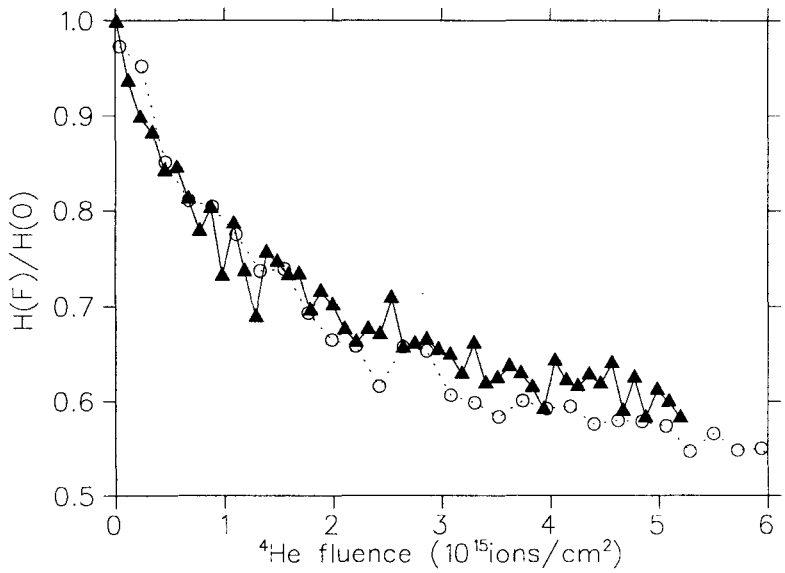

Figure 5.1.25: *comparison of the hydrogen release curves obtained from experiment number 1 (▲) and experiment number 2 (○). Only a fraction of the datapoints is shown for clarity but no extra averaging was performed.*

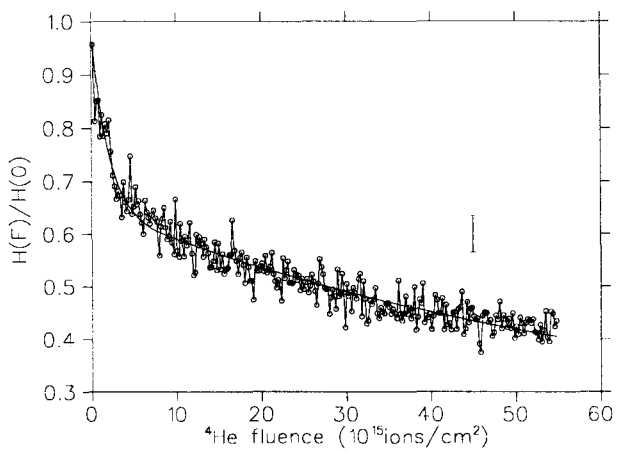

Figure 5.1.26: *relative hydrogen content as a function of 4 MeV ^{4}He fluence, exp. number 3.*

The RBS indium yield was used for normalization in the 2 and 4 MeV ^{4}He hydrogen loss experiments, a region corresponding to Si was selected in the case of the 7.6 MeV and 12.1 MeV experiments.

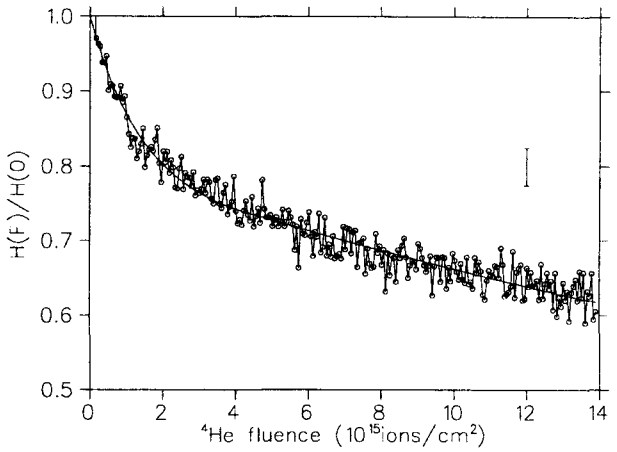

Figure 5.1.27: *relative hydrogen content as a function of 7.6 MeV ^{4}He fluence, exp. number 4.*

Judging from figures 5.1.23 to 5.1.27, the measured hydrogen loss can be adequately described by fitting the data according to the hydrogen loss model. The parameters k_1/k_2, V and ξ^2A (see chapter 3, paragraph 5) were calculated from the fits and are shown in table 5.1.2.

experiment number	beam energy (MeV)	k_1/k_2 (Å^3)	V (Å^3)	ξ^2A (Å^2)
1	2	3.8	47	7.0
2	2	4.5	56	4.2
3	4	1.9	54	3,0
4	7.6	2.0	44	4.5

Table 5.1.2: *fitted values for k_1/k_2, V and ξ^2A.*

A mean combination volume V (see paragraph 3.5.2) of 50±6 Å^3 could be deduced from the fits with an initial hydrogen density ρ(0) equal to 31 atoms/nm^3, which follows from the known mass density (1.35 g/cm^3) of the porphyrin material and the molecular composition ($Pd_1C_{44}H_{28}N_4O_4$). This corresponds to a direct combination distance of 2.3±0.1 Å, which is in good agreement with the nuclear separation distance λ=3 Å beyond which the molecular potential of H_2 in vacuum decreases rapidly. N.B.: a direct combination distance smaller than 3 Å was to be expected since molecular potentials are affected by screening in solid materials.
According to the theoretical hydrogen loss model, ξ^2A is the only quantity that depends on the kinetic energy of the impinging ^{4}He ions, since this is the only parameter that contains the properties of the ion track (the bond breaking probability ξ and the effective track area A, see paragraph 3.5.1). As can be seen from table 5.1.2, this does not show up right away in the

numbers obtained from the fits, which indicates that the model is an oversimplification of the actual hydrogen loss process. However, if we fit the experimental data with fixed mean values for V and k_1/k_2 (V=50 Å^3, k_1/k_2=3.1 Å^3) while allowing ξ^2A to vary, a fair agreement with theoretical calculations (see paragraph 3.5.1) is obtained (see table 5.1.3, figure 5.1.28 and figure 5.1.29).

experiment number	beam energy (MeV)	calculated effective track area A (nm^2)	N_δ: calculated #δ-rays per nm path length	ξ^2A (Å^2), fitted	ξ, calculated from $(\xi^2 A/A)^{1/2}$
1	2	21	2.2	6.0	0.053
2	2	21	2.2	7.6	0.060
3	4	27	1.2	2.4	0.030
4	7.6	39	0.7	1.8	0.022

Table 5.1.3: *comparison of the fitted parameter ξ^2A (V and k_1/k_2 constant) with calculated values for A and N_δ (see chapter 3, paragraph 5).*

As discussed in chapter 3, paragraph 5 we assume the bond breaking probability ξ in the artificial track formed by the cylinder with cross section A to be proportional to the number of emitted δ-rays per unit path length N_δ, which in return depends on the beam energy. Dividing the fitted parameter ξ^2A by the calculated effective track area gives the bond breaking probability ξ (see table 5.1.2), which indeed scales with N_δ (see table 5.1.4).

Comparison of different beam energies	ratio of the corresponding N_δ's	ratio of the corresponding ξ's in table 5.1.3
2 vs. 4 MeV	1.8	1.9
4 vs. 7.6 MeV	1.7	1.4

Table 5.1.4: *comparison of the ratios $N_{\delta,i}/N_{\delta,j}$ (see equation 3.5.2) and ξ_i/ξ_j for different ^{4}He energies i and j.*

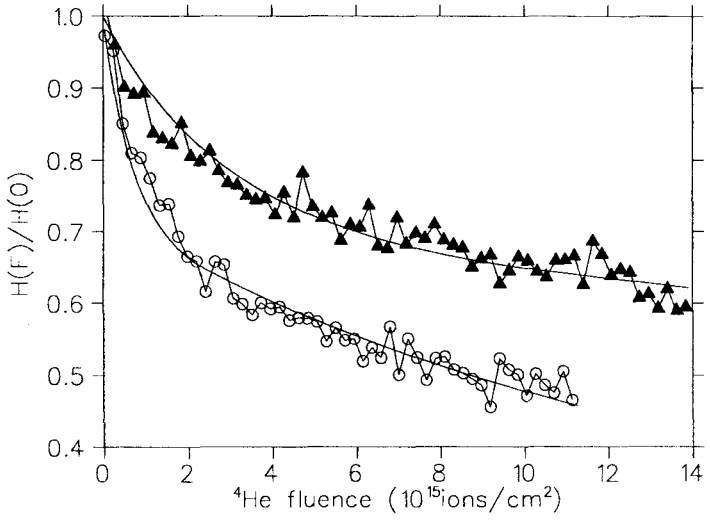

Figure 5.1.28: *2 (o) and 7.6 (▲) MeV ^{4}He induced hydrogen loss. The <u>one parameter</u> fits (represented by the smooth lines) were obtained with fixed values for V and k_1/k_2 (V=50 Å^3 and k_1/k_2=3.1 Å^3) while ξ^2A was allowed to vary. Not all data points are shown for clarity.*

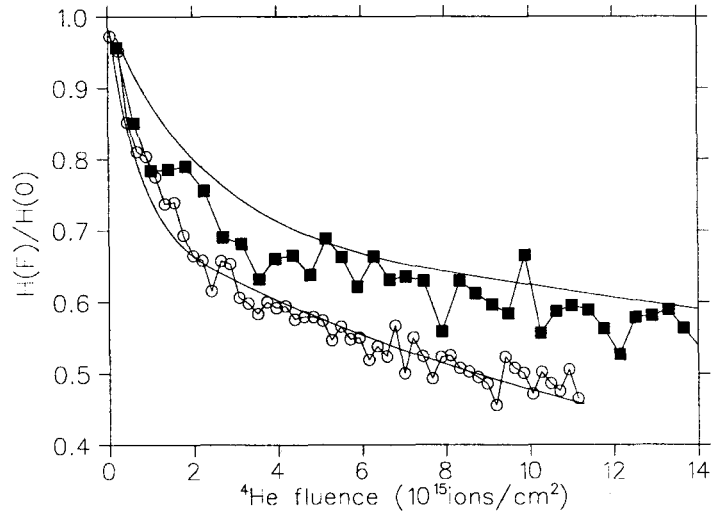

Figure 5.1.29: *2 (o) and 4 (■) MeV ^{4}He induced hydrogen loss. The <u>one parameter</u> fits (represented by the smooth lines) were obtained with fixed values for V and k_1/k_2 (V=50 Å^3 and k_1/k_2=3.1 Å^3) while ξ^2A was allowed to vary. Not all data points are shown for clarity.*

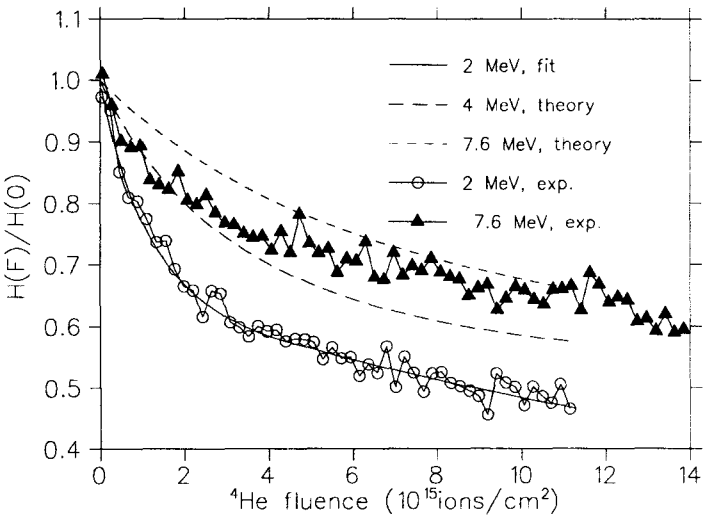

Figure 5.1.30: *the dashed curves, which represent "theoretical" hydrogen loss under 4 and 7.6 MeV ^{4}He irradiation, were calculated from the fitted 2 MeV curve (solid line) according to the hydrogen loss model. The calculations show a larger difference than was experimentally observed.*

Though the measured hydrogen loss decreases when the beam energy is increased from 2 to 4 and further to 7.6 MeV, the decrease is not quite as pronounced as predicted by the model. To illustrate this, we calculated the theoretical hydrogen loss curves for 4 and 7.6 MeV ^{4}He irradiation from the fitted curve for 2 MeV (experiment number 2) through theoretical scaling of the parameter $\xi^2 A$ (see figure 5.1.30).
Surprisingly, the 12.1 MeV ^{4}He irradiation experiments show a fast initial hydrogen loss rate (see figures 5.1.31 and 5.1.32). It should be noted that to the large background in the 12.1 MeV ^{4}He H-ERDA spectra, the calculation of the relative hydrogen content from the detection yield becomes more inaccurate even though a background subtraction was performed.

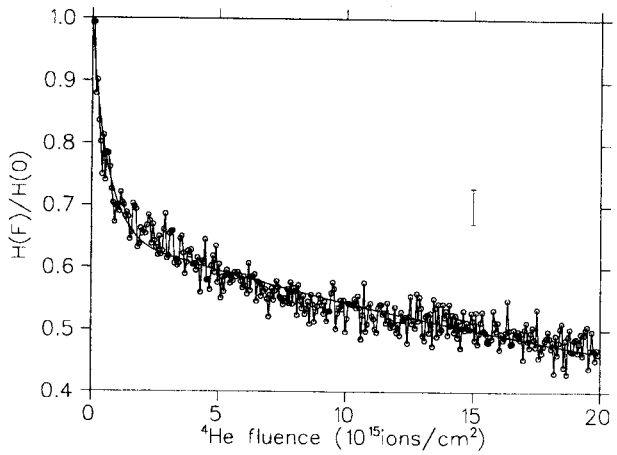

Figure 5.1.31: *relative hydrogen content as a function of 12.1 MeV ^{4}He fluence, experiment number 5.*

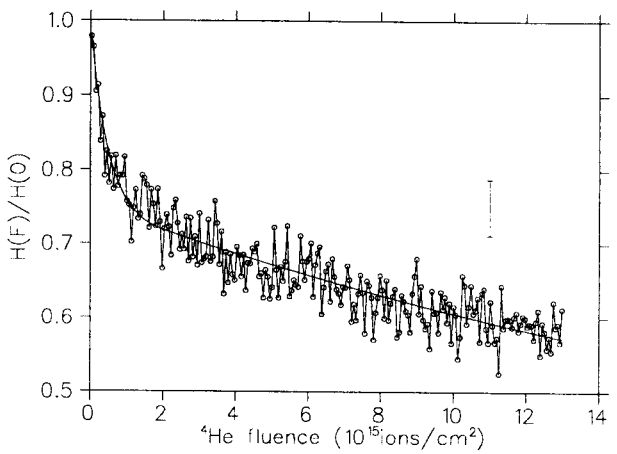

Figure 5.1.32: *relative hydrogen content as a function of 12.1 MeV ^{4}He fluence, experiment number 6.*

Figure 5.1.33 shows a comparison between the two 12.1 MeV ^{4}He hydrogen loss measurements. The matching of the curves is not perfect, the difference probably stems from uncertainties in the first few datapoints were the hydrogen release rate is maximal.

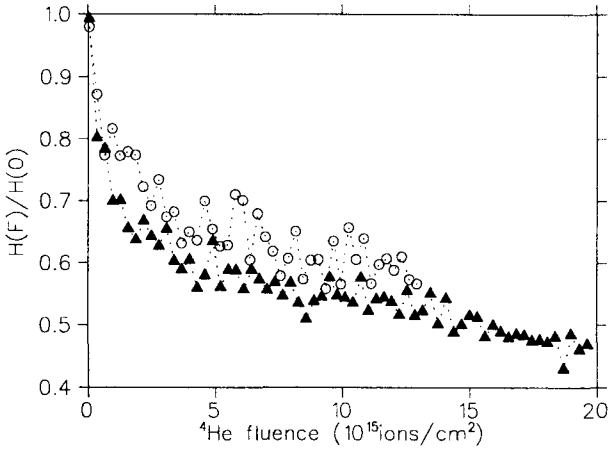

Figure 5.1.33: *comparison of experiments 5 (○) and 6 (▲). Only a fraction of the points is shown for clarity.*

Though the accuracy of the measured hydrogen loss under 12.1 MeV ^{4}He irradiation is limited by the background, comparison between experiments 2 (2 MeV) and 5 (12.1. MeV) show far less difference than expected (see figure 5.1.34), despite the much lower energy deposition by 12.1 MeV ^{4}He ions (the ratio of the stopping powers for 2 and 12.1 MeV ^{4}He ions in porphyrin material is approximately 3:1).

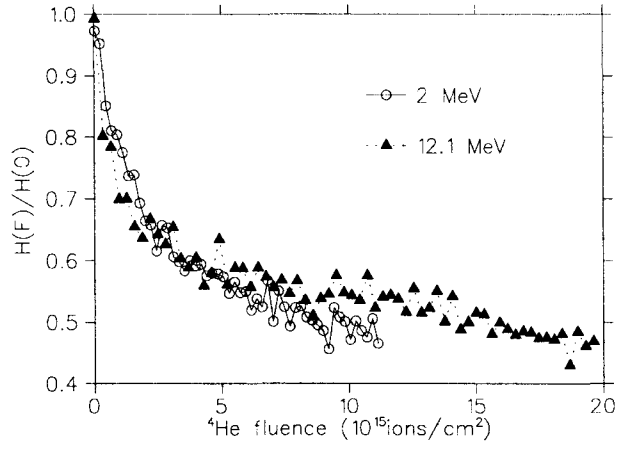

Figure 5.1.34: *comparison of 2 and 12.1 MeV ^{4}He induced hydrogen loss, experiments 2 and 5 respectively.*

We see that hydrogen loss under 12.1 MeV irradiation is especially severe in the initial stage of irradiation (see figure 5.1.35), followed by a sharp bend in the slope of the hydrogen loss curve

at a fluence of approximately $1 \cdot 10^{15}$ cm^{-2}. This might be caused by a lower initial trap concentration (due to the slower amorphization process) which would lead to an increased loss of hydrogen even if less hydrogen bonds are broken, perhaps even through atomic diffusion to the surface.

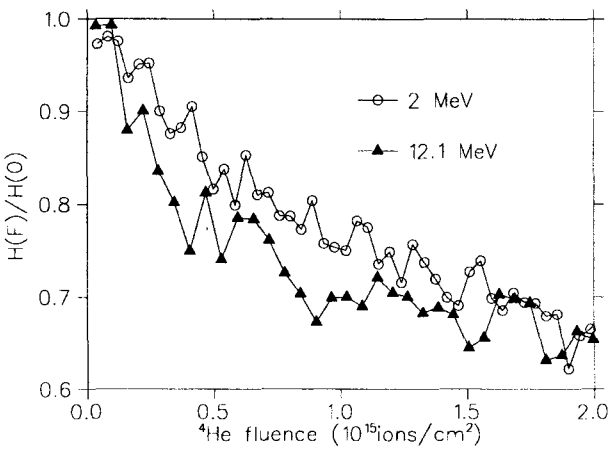

Figure 5.1.35: *comparison of 2 and 12.1 MeV ^{4}He induced hydrogen loss at the initial stage of irradiation.*

An estimate of the average trap density can be given by evaluation of k_1/k_2, the ratio of the reaction constants for the formation of H_2 (k_1) and trapping (k_2). Recall that k_2 was defined as $k_2=\kappa_2[T]$ where $[T]$ is the concentration of traps and κ_2 is the "true" reaction constant for the trapping reaction (see chapter 3, paragraph 5). When we assume that the reaction time for the formation of a H_2 molecule is approximately equal to the reaction time for the trapping of a H atom, the trap density is given by $[T]=(k_1/k_2)^{-1}$. Inserting the mean value for $k_1/k_2=3.1$ Å^3 obtained from the experiments gives $[T]\approx 320$ nm^{-3}. If the initial trap concentration is set equal to the density of π-electrons in the porphyrin material one finds $[T]_{initial}\approx 50$ nm^{-3}, which indicates that the formation of traps during irradiation is important.

5.1.5 Background subtraction

A linear fit is calculated through the background on which the signal of interest is situated (see figure 5.1.36).

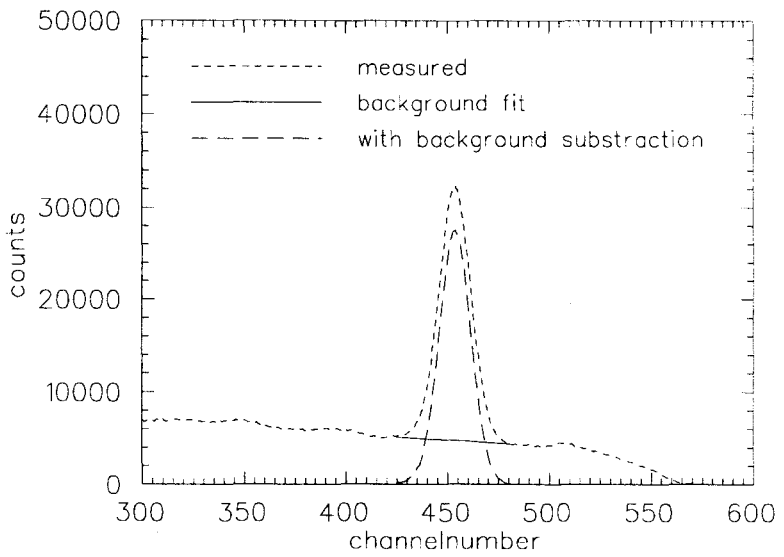

Figure 5.1.36: *background subtraction in the H-ERDA spectrum obtained from experiment number 5 (12.1 MeV ^{4}He).*

The contribution of the background Y_{back} to the total number of counts Y_{tot} in the region of interest that contains the relevant peak (in the case of figure 5.1.36 this is the hydrogen feature) can now be calculated. Y_{back} contains the total number of background counts summed over all files. However, the background has to be subtracted for each file to obtain a plot of detection yield vs. filenumber. To achieve this, we proceed as follows. The background is mainly due to proton producing nuclear reactions in the substrate (see paragraph 5.1.6) and hence the number of counts per file will only vary with beam current variations. As stated before, this beam current variations can be monitored by evaluating the RBS monitoring yield Y_{mon} for each file. The appropriate background subtraction per file Y_f is thus $Y_f=Y_{mean}(Y_{mon}/Y_{mon,mean})$ where Y_{mean} is the mean number of background counts per file, Y_{mon} and $Y_{mon,mean}$ are the RBS monitoring yield and mean RBS monitoring yield per file, respectively.

5.1.6 The background in the 12.1 MeV ^{4}He H-ERDA experiments

In paragraph 5.1.1, we saw that a background appeared in the H-ERDA spectra of the 7.6 and 12.1 MeV ^{4}He experiments. In order to investigate the origin of this background, several experiments were performed with a 12.1 MeV ^{4}He beam.
An energy calibration was carried out using a Am-Cm ^{4}He source, which emits ^{4}He particles at fixed energies (Am: 5.443 and 5.486 MeV, Cm: 5.764 and 5.805 MeV).
ERDA experiments were performed on a carbon foil (thickness 100 μg/cm^2, 90° angle of incidence) to study the possibility of proton producing nuclear reactions between the ^{4}He and ^{12}C nuclei. The detector was placed at 43° with respect to the ion beam.

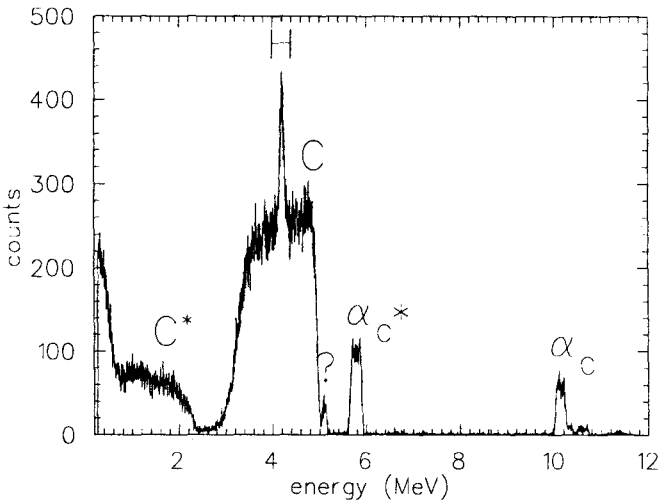

Figure 5.1.37: *energy spectrum of forward scattered α particles and C and H recoils, obtained from a 12.1 MeV α scattering experiment on a thin carbon foil.*
Explanation of symbols: C= carbon recoiling from an inelastic collision, α_C^*= ^{4}He nuclei scattered from inelastic collisions with carbon nuclei. H, C and α= elastically recoiled hydrogen and carbon and elastically scattered α's on C, respectively. ?=unknown (for the moment). (the detected H particles arise from surface contamination).*

The features in figure 5.1.37 could be identified by means of a theoretical calculation of the kinetic energies of the indicated scatters and recoils (see equations 2.2.4 to 2.2.7). We will now focus on the feature at 5.1 MeV that is labelled with a question mark in figure 5.1.37.
A calculation of the kinetic energy of protons emitted at 43° in the reaction ^{12}C(α,p)^{15}N with a Q value of -4.966 MeV [YON94] and E_α=12.1 MeV gives the correct number: 5.1 MeV (E_α is the kinetic energy of the α particles). To complete the identification of the "5.1 MeV peak", an additional experiment was performed with a brass stopper foil (estimated thickness ≈50 μm) placed in front of the detector. The corresponding energy spectrum is depicted in figure 5.1.38. All carbon recoils and the major part of the scattered α particles were stopped in the foil. The foil

proved to be thinner than expected: high energy (≈10 MeV) α's could still pass through (see figure 5.1.38).
The thickness of the foil could be estimated from a TRIM calculation of the energy loss of the recoiled hydrogen nuclei as a function of penetration depth in the foil, since this energy loss is known from the experiments. Accordingly, one finds a foil thickness of 23 μm. This foil thickness corresponds to an energy loss for 5.1 MeV protons of approximately 0.87 MeV (TRIM calculation, see figure 5.1.40). Experimentally, we find that the 5.1 MeV peak shifts to a 0.84 MeV lower energy. Since these numbers agree within 4%, the "5.1 MeV feature" can be identified as a peak arising from protons produced in the reaction $^{12}C(\alpha,p)^{15}N$.

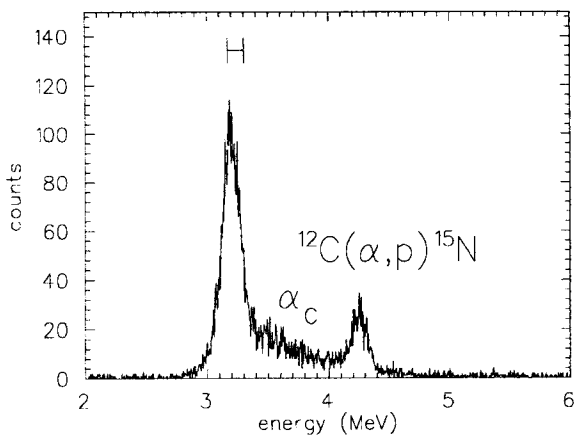

Figure 5.1.38: *energy spectrum of recoiled hydrogen and protons produced in the nuclear reaction $^{12}C(\alpha,p)^{15}N$. A brass stopper foil was placed in front of the detector. Not all scattered ^4He particles are stopped in the foil, high energy α's appear in the spectrum between the H and $^{12}C(\alpha,p)^{15}N$ features.*

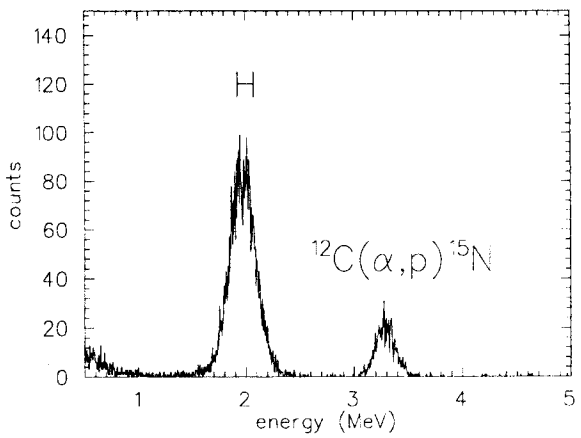

Figure 5.1.39: *energy spectrum of recoiled H and $^{12}C(\alpha,p)^{15}N$ protons obtained with <u>two</u> similar brass stopper foils placed in front of the detector. All ^4He particles are stopped in the foils.*

When two similar stopper foils (both approximately 23 μm thick) are placed in front of the detector, all scattered α particles are stopped (see figure 5.1.39). The energy loss of the elastically recoiled hydrogen particles and the $^{12}C(\alpha,p)^{15}N$ protons corresponds to a combined foil thickness of 45 μm (TRIM calculation), in good agreement with the earlier calculated 23 μm for a single foil.

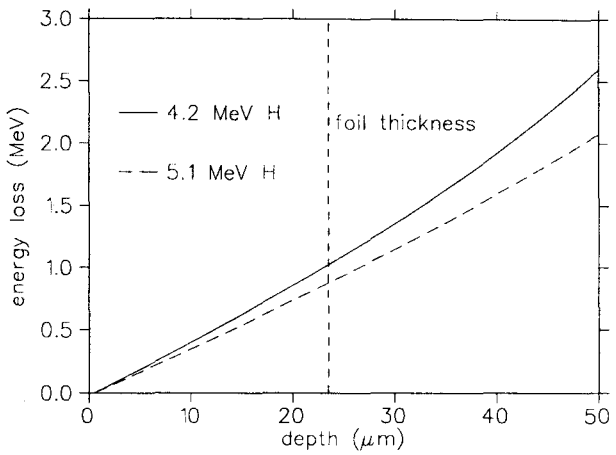

Figure 5.1.40: *the energy loss in brass (60% Cu, 40% Zn) of 4.2 and 5.1 MeV protons as a function of penetration depth as calculated using TRIM. The stopper foil thickness follows from the measured energy loss of the 4.2 MeV H recoils. With given foil thickness, the energy loss of 5.1 MeV protons is also known.*

Apart from the reaction $^{12}C(\alpha,p)^{15}N$, other proton producing nuclear reactions contribute (more significantly) to the background in the 12.1 MeV ^{4}He H-ERDA experiments. The element Si (located in the glass substrate) plays an important role, as can be seen from figure 5.1.41.

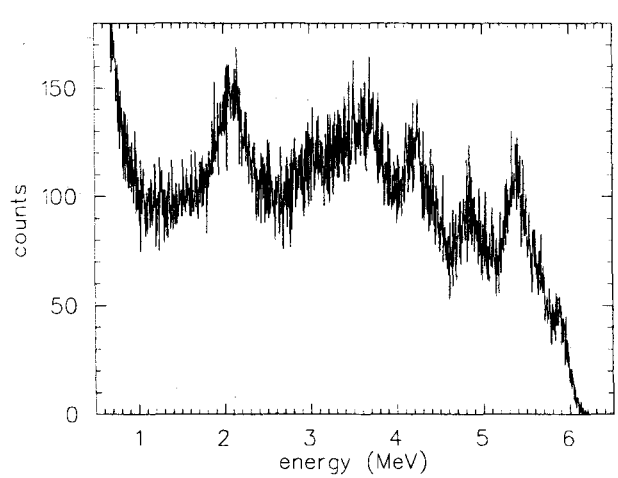

Figure 5.1.41: *energy spectrum of nuclear reaction products detected at 43° with respect to a 12.1 MeV α beam incident on a crystalline silicon target. The feature at approximately 2.3 MeV is probably due to hydrogen surface contamination.*

The spectrum shown in figure 5.1.41 was obtained with the same two brass foils (total thickness ≈43 μm) placed in front of the detector in order to stop scattered α particles. Since the formerly described experiments indicate that no scattered α's are transmitted through the foils, the detected particles must be light (lighter than ^{4}He) reaction products of nuclear reactions between the ^{4}He and ^{28}Si nuclei (reactions with ^{29}Si and ^{30}Si, natural abundance 4.7% and 3.1% respectively, are also possible).
Some possible reactions are [YON94]:

- $^{28}Si(\alpha,p_0)^{31}P$, Q=-1.9158, surface proton energy E_p=9.32 MeV;
- $^{28}Si(\alpha,p_1)^{31}P$, Q=-3.1819, E_p=8.03 MeV;
- $^{28}Si(\alpha,p_2)^{31}P$, Q=-4.1500, E_p=7.03 MeV;

the indices i in p_i correspond to excited states in the produced nucleons. The interpretation of the spectrum is not straightforward, since a number of detected particles may only have deposited a fraction of their kinetic energy in the approximately 300 μm thick Si-detector. For protons, the energy deposition in a 300 μm thick Si layer is maximal when the proton kinetic energy is roughly 6 MeV: these protons have a range of ±300 μm in silicon. Since the largest detected energy is about 6 MeV, the detected particles might very well be protons only. However, emission of deuterium nuclei can not be excluded.
Figure 5.1.42 shows a comparison between figure 5.1.41 and the enlarged background in a 12.1 MeV ^{4}He H-ERDA experiment on a porphyrin sample.

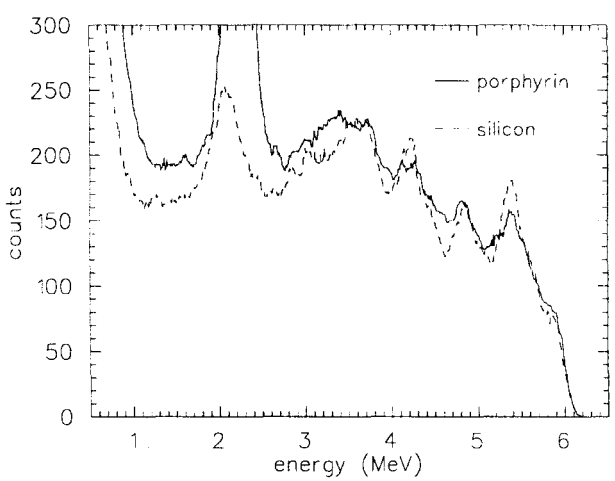

Figure 5.1.42: *comparison of the (smoothed) spectra of reaction products from nuclear reactions in crystalline silicon and the background in a H-ERDA spectrum of a porphyrin film on ITO coated glass (see chapter 4 paragraph 1 for a description of the porphyrin samples). Judging from the obvious similarities between the two spectra, the background in the porphyrin H-ERDA spectrum is mainly due to nuclear reactions between α particles and Si nuclei in the glass substrate. Comparing the spectra one should realize that the kinetic energy of the α particles that reach the glass substrate has been slightly (several keV) decreased due to energy loss in the porphyrin and ITO layers, which results in different proton energies.*

Figure 5.1.42 indicates that particles emitted in reactions between Si and ^{4}He nuclei contribute

in a major way to the background in the 12.1 MeV ^{4}He H-ERDA experiments. The difference between the two spectra at approximately 3.3 MeV might be caused by the $^{12}C(\alpha,p)^{15}N$ reaction that will occur in the porphyrin layer (see figure 5.1.39).
An additional experiment was performed on a bare substrate (ITO coated glass). The so obtained energy spectrum of detected particles showed very little difference with figure 5.1.41.

5.2 Possible carbon loss from porphyrin layers subjected to 4 and 12.1 MeV ^{4}He beams

Due to the resonance near 4 MeV ^{4}He energy in the ^{4}He-^{12}C scattering cross section [LEA89], the RBS carbon peak was sufficiently enhanced to study the time dependent carbon content (see figure 5.1.15) in experiment number 3. First, the background on which the carbon peak is situated had to be subtracted (see paragraph 5.1.5).

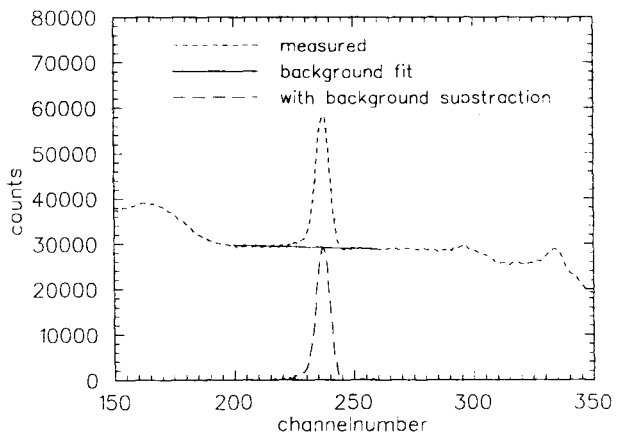

Figure 5.2.5: an isolated carbon peak is obtained by means of background subtraction.

A plot of the relative carbon content (corrected for beam current fluctuations) vs. ion fluence is depicted in figure 5.2.6.

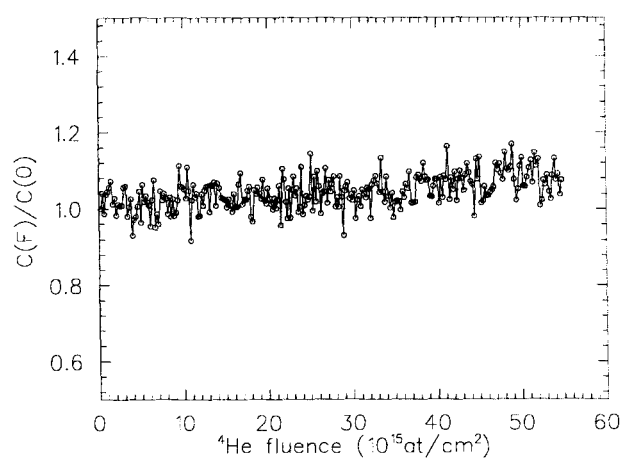

Figure 5.2.6: relative carbon content as a function of 4 MeV ^{4}He fluence, experiment number 3.

No carbon loss is observed, the carbon content increases slightly instead. This is a common feature in long lasting (several hours) irradiation experiments: through the fractioning of hydrocarbons by the ion beam (hydrocarbons are always present in the scattering chamber, the pressure in the chamber is approximately $5 \cdot 10^{-6}$ mbar), radicals are formed which are easily chemisorbed or adsorbed on the surface of the sample. Hence, an extra amount of carbon is deposited.
The detection of carbon recoils was possible at 12.1 MeV beam energy by means of the PSD-ERDA technique (see chapter 2 paragraph 5). The corresponding energy/timing spectrum is shown in figure 5.2.7.

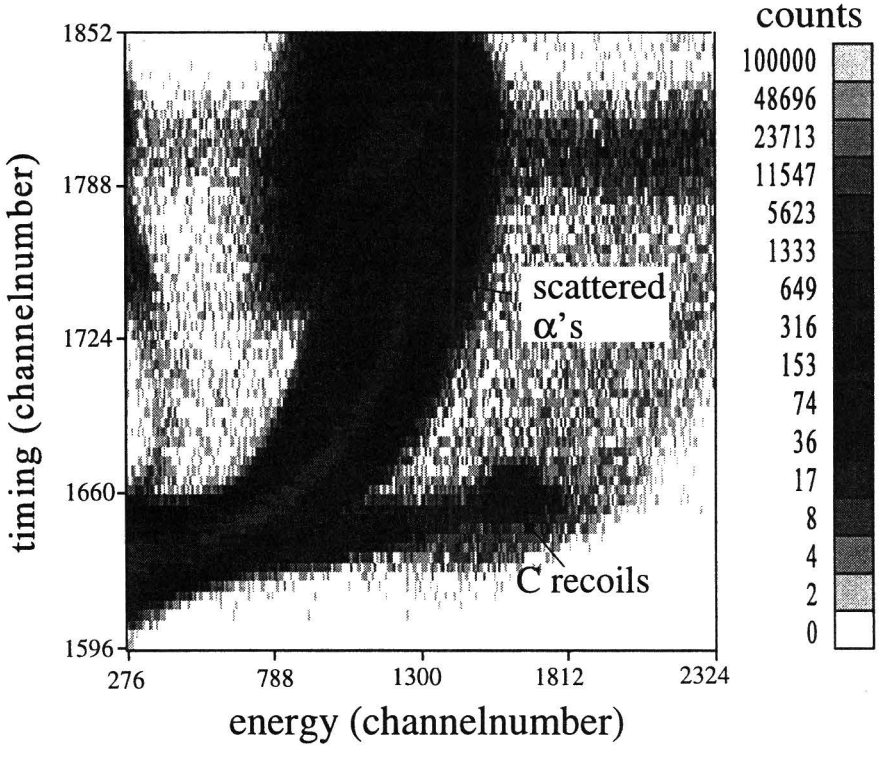

Figure 5.2.7: *energy/timing spectrum of recoils and scatters in a PSD-ERDA experiment. The detector was placed at 30° with respect to a 12.1 MeV ^{4}He beam incident on a porphyrin/ITO/glass target. Due to the different charge collection rates (see paragraph 2.5), the timing signals for scattered α's and C recoils with comparable energy deposition differ considerably. In the energy/timing plane, the scatters and recoils are therefore separated.*

Scattered α particles with high kinetic energy are stopped far beyond the depletion layer, which causes a much slower charge collection rate and hence a slow timing pulse (see paragraph 2.5). Moreover, the charge collection becomes incomplete due to recombination of diffusing charge carriers, which causes the curve of scattered α's to fold backwards (i.e. to a lower energy) when their kinetic energy is increased beyond a certain point.

By selecting a region in the energy/timing plane in figure 5.2.7 that contains the detected carbon recoils, the carbon yield could again be plotted as a function of filenumber. The RBS-indium yield was used as normalization. Again, no carbon loss was observed as can be seen from figure 5.2.8.

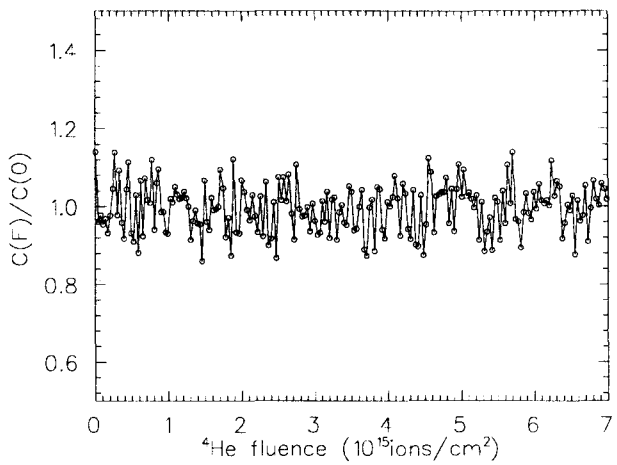

Figure 5.2.8: *relative carbon content as a function of 12.1 MeV ^{4}He fluence, obtained from a PSD-ERDA experiment.*

5.3 Hydrogen loss induced by 4 and 10 MeV ^{12}C bombardment

Using the magnetic spectrograph setup at UU (see chapter 4, paragraph 3), hydrogen-ERDA experiments were performed using 4 and 10 MeV ^{12}C beams. The spectrograph was adjusted such that only hydrogen recoils were detected.
The measured hydrogen loss under 4 MeV ^{12}C irradiation is shown in figure 5.3.1.

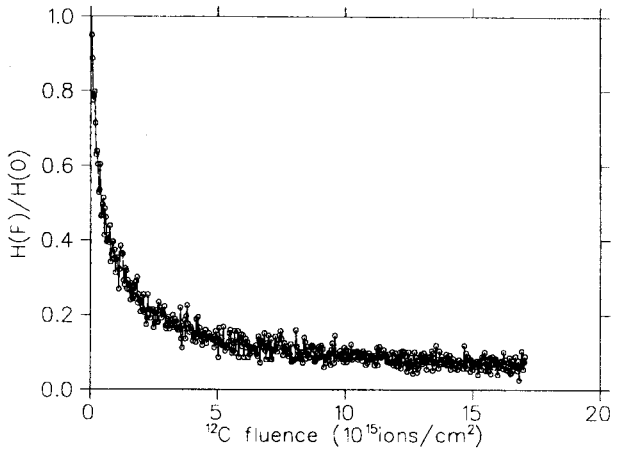

Figure 5.3.1: *relative hydrogen content as a function of 4 MeV ^{12}C fluence.*

It is sometimes claimed in literature that a quasi stable final state is reached from which hydrogen loss becomes negligible (see for instance [ADE89]). However, figure 5.3.2 clearly shows that even for a very high ^{12}C fluence (>$15 \cdot 10^{15}$ cm^2), no (quasi) stable hydrogen concentration is reached.

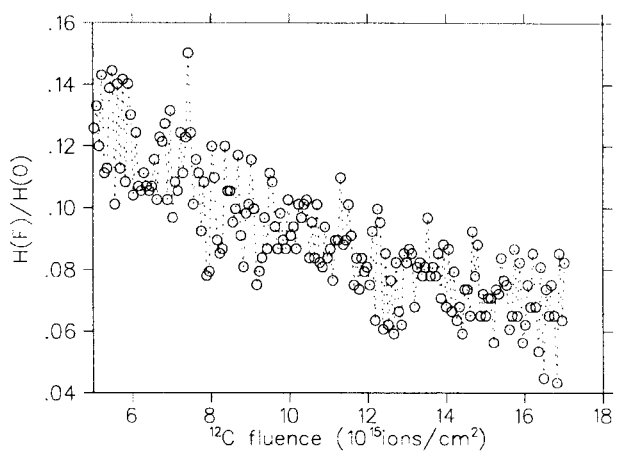

Figure 5.3.2: *an enlarged picture of the final stage of the hydrogen loss curve in figure 5.3.1.*

This result is in agreement with the ^{4}He irradiation experiments, which also show no stabilization at high ion fluence (see for example figure 5.1.26: 4 MeV ^{4}He induced hydrogen loss continues even at a fluence of $55 \cdot 10^{15}$ cm^2).
Due to the decreased energy deposition, 10 MeV ^{12}C ions induce less hydrogen loss as can be seen from figure 5.3.3. A comparison with 2 MeV ^{4}He induced hydrogen release, which is much less severe, is also shown.

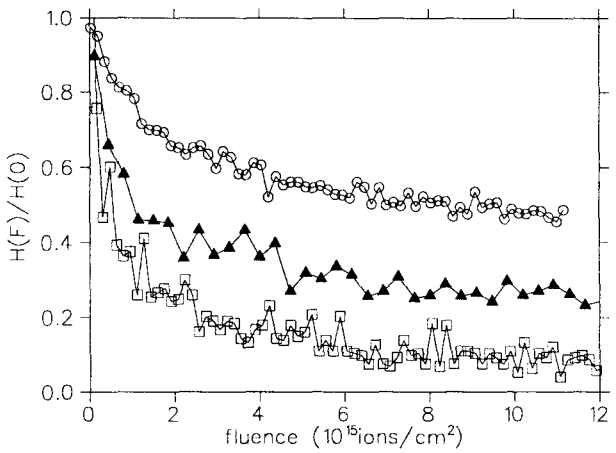

Figure 5.3.3: *comparison of hydrogen loss under 4 (□) and 10 (▲) MeV ^{12}C irradiation and 2 MeV ^{4}He bombardment (○).*

Under ^{12}C irradiation, the carbon content in the porphyrin layers decreases (roughly 10% is lost [MAR96]) which means that small hydrocarbons (CH_4, C_2H_4 etc.) are released from the material. The amount of hydrogen that is lost in the form of these hydrocarbons is significant: assuming 2 hydrogen atoms per carbon atom in each lost molecule a 10% decrease of the carbon content means that the hydrogen content reduces with roughly 30% (in porphyrins the C/H ratio is approximately 3/2). The hydrogen loss model described in paragraph 3.5, which only considers the loss of H_2, will thus not be suitable to describe ^{12}C induced hydrogen loss.

5.4 Hydrogen loss versus detection sensitivity

The quantification of the hydrogen content in an organic material requires a sufficient number of detected particles. Therefore it is not only important to minimize hydrogen loss, the detection sensitivity for hydrogen (i.e. the differential cross section) must also be considered. In other words: the amount of lost hydrogen should be kept small with respect to the detection yield. Table 5.4.1 shows a comparison of the differential cross section $d\sigma/d\Omega$ at a 30° recoil angle and the induced hydrogen loss H_{loss} in the fluence region $2\text{-}6\cdot10^{15}$ ions/cm^2 for various ion beams.

ion beam	$d\sigma/d\Omega$ (mbarn/sr)	H_{loss}	$(d\sigma/d\Omega)/H_{loss}$ (a.u.)
2 MeV $^4He^+$	392	41%	9.6
4 MeV $^4He^+$	315	32%	9.8
7.6 MeV $^4He^{2+}$	679	25%	27.2
4 MeV $^{12}C^{3+}$	2990	84%	35.5
10 MeV $^{12}C^{4+}$	479	64%	7.5

Table 5.4.1: *comparison of hydrogen loss and differential cross section for various ion beams.*

The ^{4}He-p recoil cross sections can be found in [BEN86], Rutherford ^{12}C-p scattering was assumed. Table 5.4.1 clearly indicates that minimizing the hydrogen loss alone does not necessarily improve the ratio $(d\sigma/d\Omega)/H_{loss}$.

Chapter 6: Conclusions and recommendations

The hydrogen loss model discussed in paragraph 3.5 gives an adequate description of the measured hydrogen loss curves under ^{4}He irradiation. The fast initial depletion followed by a much slower release rate without reaching a stable hydrogen concentration can be understood by considering the two mechanisms of direct combination and the formation of H_2 by diffusing radicals.

The ^{4}He kinetic energy dependence of the hydrogen loss process for 2, 4 and 7.6 MeV ^{4}He beams can also be explained by the model, by means of a calculation of the properties of the ion tracks: the track width depends on the range of the secondary electrons and the bond breaking probability is proportional to the number of produced δ-rays per unit path length.

Benefit can be taken from the fact that a 7.6 MeV ^{4}He beam not only inflicts a relatively low amount of damage but also provides a good detection sensitivity, due to non-Rutherford ^{4}He-p scattering in the energy region above 2 MeV.

The results of the 12.1 MeV ^{4}He hydrogen loss experiments do not fit in the general picture of decreasing damage with decreasing energy deposition. Further experiments are needed to confirm the observed increased hydrogen loss. The hypothesis that this might be due to a slower production of hydrogen-traps can be tested by measuring the hydrogen loss under 12.1 MeV ^{4}He irradiation from a sample that has been pre-irradiated with a small dose of 2 MeV ^{4}He ions (in order to produce a large amount of traps).

Though the loss of hydrogen can be diminished by adjusting the beam energy, it always occurs in hydrogen-ERDA experiments. Other solutions are required to further suppress the outgassing of volatile molecules as H_2, such as using a cooled substrate holder ($T \approx 20$ K) in order to freeze the molecules (or radicals) in place.

References

[ADE89] M.E. Adel, O. Amir, R. Kalish and L.C. Feldman
Ion-beam-induced hydrogen release from a-C:H: A bulk recombination model
J. Appl. Phys. 66(7), 1989

[ARN96] W. M. ArnoldBik et al.
Nucl. Instr. and Meth. B (to be published)

[AUD93] A. Audouard, E. Balanzat, J.C. Jousset, D. Lesueur and L. Thomé
Atomic displacements and atomic motion induced by electronic excitation in heavy-ion-irradiated amorphous metallic compounds
J. Phys: Condensed Matter 5, 1993

[BAR95] I. Baraldi, A. Carnevali, G. Ponterini and D. Vanossi
Electronic spectrum of porphyrins: CS INDO CI study
J. of Molecular Structure (Theochem) 333, 1995

[BEN86] R.E. Benenson, L.S. Wielunski and W.A. Lanford
Computer simulation of helium-induced forward-recoil proton spectra for hydrogen concentration determinations
Nucl. Instr. and Meth. B15, 1986

[BRA82] W. Brandt and M. Kitagawa
Effective stopping-power charges of swift ions in condensed matter
Phys. Review B25(9), 1982

[BRA93] P.J.M. Brands, J. Jonkers and M.B. Keuzenkamp
Nuclear analysis techniques
According to the lectures by prof. dr. M.J.A. de Voigt, EUT, 1993

[CAL92] L. Clacagno, G. Compagnini and G. Foti
Stuctural modification of polymer films by ion irradiation
Nucl. Instr. and Meth. B65, 1992

[CHA88] A. Chapiro
Chemical modifications in irradiated polymers
Nucl. Instr. and Meth. B32, 1988

[DAV93] J.A. Davies and R. Siegele
High energy heavy ion RBS, ERDA and channeling
In: *Application of particle and laser beams in materials technology*
Kluwer Academic Publishers, Dordrecht/Boston/London 1993

[DIC86] P. Dickstein, D. Ingman and N.H. Shafrir
Z_2 oscillation systematics in the stopping of fission fragments
Nucl. Instr. and Meth. B15, 1986

[DOO90] L. R. Doolittle
High energy backscattering analysis using RUMP
Conference Proceedings, Heavy Ion Beams. Materials Research Society 1990

[DUN93] A. Dunlop, D. Lesueur and A. Barbu
Evolution of microstructure resulting from high electronic excitation during swift heavy ion irradiations
J. of Nucl. Materials 205, 1993

[FEL86] L.C. Feldman and J.W. Mayer
Fundamentals of surface and thin film analysis
Elsevier Science Publishing, Amsterdam, 1986

[GEY86] E. Geyer, D. Reschke and K. Freitag
Z_1 stopping power oscillation in the nuclear stopping regime as obtained by time-of-flight spectroscopy of heavy ions in hydrogen
Nucl. Instr. and Meth. B15, 1986

[GOL93] R. Golser
Fundamentals of ion electron interactions
In: *Application of particle and laser beams in materials technology*
Kluwer Academic Publishers, Dordrecht/Boston/London 1993

[KNO79] G.F. Knoll
Radiation detection and measurement
Wiley & Sons, New York, 1979

[KOB68] E.J. Kobetich and R. Katz
Energy deposition by electron beams and δ rays
Phys. Review 170(2), 1968

[KRA88] K. S. Krane
Introductory nuclear physics
Wiley & Sons, New York, 1988

[LEA86] J.A. Leavitt et al.
Cross sections for 170° backscattering of ^{4}He from oxygen, aluminum and argon for ^{4}He enrgies between 1.8 and 5.0 MeV
Nucl. Instr. and Meth. B15, 1986

[LEA89] J.A. Leavitt et al.
Cross sections for 170.5° backscattering of ^{4}He from carbon for ^{4}He energies between 1.6 and 5.0 MeV
Nucl. Instr. and Meth. B40/41, 1989

[MAR96] C.H.M. Marée
Ion beam studies of organic solar cell structures
Ph.D. thesis, Utrecht University, 1996

[MAT95] R.J. Mathar and M. Passelt
Effective-charge theory for the electronic stopping of heavy ions in solids: stripping criteria ans target-electron models
Phys. Review B51(1), 1995

[SIM94] D.P.L. Simons
Pulse shape discrimination with a multi-parameter data-aquisition system
Master of Science thesis, EUT, 1994

[TOU92] M. Toulemonde and C. Dufour
Transient thermal process after a high-energy heavy-ion irradiation of amorphous metals and semiconductors
Phys. Review B46(22), 1992

[WAL86] M.P.R. Waligórsky, R.N. Hamm and R. Katz
The radial distribution of dose around the path of a heavy ion in liquid water
Nucl. Tracks Radiat. Meas. 11(6), 1986

[WIL87] Ch. Wild and P. Koidl
Thermal gas effusion from hydrogenated amorphous carbon films
Appl. Phys. Lett. 51(19), 1987

[YON94] H. Yonezawa, K. Shikano and T. Shigematsu
Backscattering cross section of 5.5 to 8 MeV alpha particles from carbon, oxygen and silicon
Nucl. Instr. and Meth. B88, 1994

[ZIE85] J.F. Ziegler, J.P. Biersack and U. Littmark
The stopping and range of ions in solids
Pergamon Press, New York, 1985

Appendix 1: Beamspot area measurements

A microscope equipped with an x-y table was used for visual inspection of the darkened spot that appears on the porphyrin samples as a result of ion irradiation. By adjusting the position of the x-y table, the sample could be moved relative to the microscope's lense with an accuracy of 0.01 mm. The relative coordinates of a certain point on the sample could be obtained by positioning the sample such that the point coincided with a marker in the optics of the microscope. The area of the spot could be obtained from a "contour scan": the coordinates of a number of points on the edge of the spot were determined and the enclosed area was calculated by means of numerical integration. Figure A1.1 shows an example of a contour obtained in the manner described above.

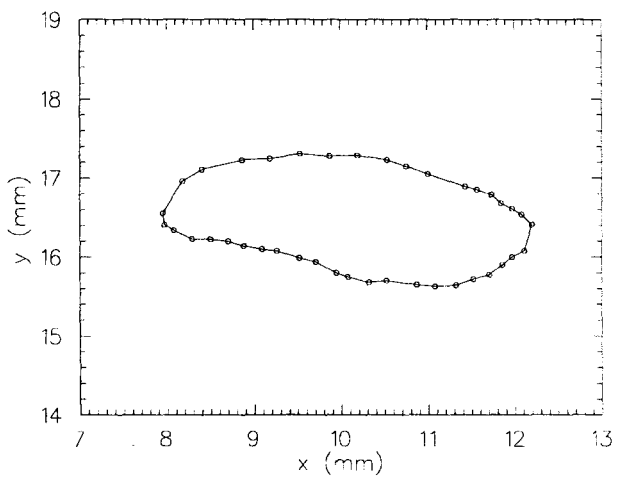

Figure A1.1: *contour scan of the blackened spot on an irradiated porphyrin sample, x and y are relative coordinates w.r.t. the position of the middle of the microscope's lense.*

The beamspot is stretched in the horizontal (x) direction due to the glancing angle of incidence. Since the exact processes that lead to the blackening of the porphyrin films under ion irradiation are unknown, the area of the blackened spot cannot immediatly be assumed to be equal to the beamspot area. Therefore, an alternative measurement was performed to determine the dimensions of the beam.
Various slits with different dimensions were milled in small metal plates that could be placed in the sample holder of the RBS/ERDA/CERDA-TOF setup. By adjusting the settings of the bending magnets closest to the setup, the beam could be moved over these slits. Measuring the current on the sample holder and the Faraday cup provided a way to determine the fraction of the beam that was transmitted through the slits. The results of two of these measurements are shown in figures A1.2 and A1.3.

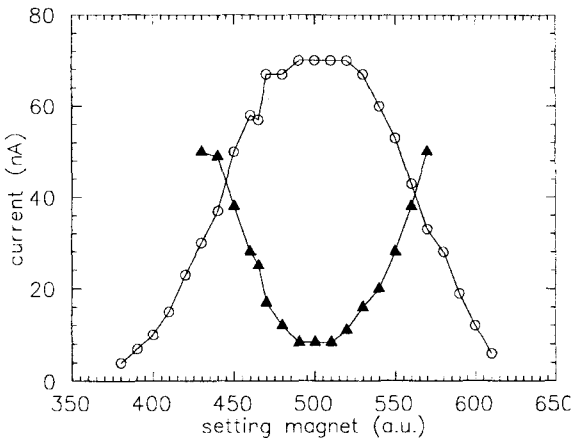

Figure A1.2: *the current on the sample holder (▲) and the Faraday cup (O) as a function of bending magnet potentiometer setting for scanning over a 2 mm horizontal slit.*

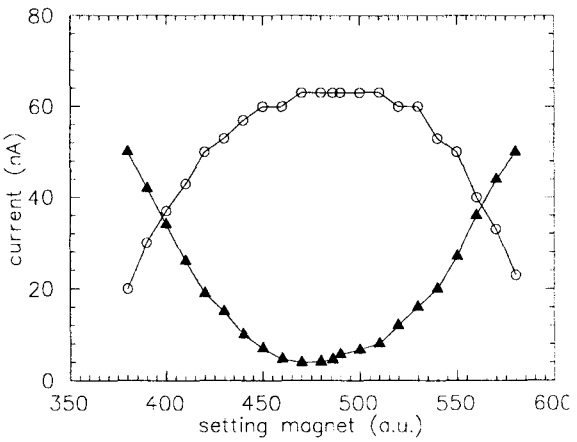

Figure A1.3: *the current on the sample holder (▲) and the Faraday cup as a function of bending magnet potentiometer setting for scanning over a 3 mm horizontal slit.*

The current through the bending magnet was adjusted by means of a potentiometer, the settings of which are referred to in figures A1.2 and A1.3. The position of the beam is directly proportional to these settings.

A comparison of the distances between the two intersection points of the curves in figures A1.2 (2 mm slit) and A1.3 (3 mm slit) gives the relation between the potentiometer settings and the relative position of the beam, since the difference between both distances (which are 117 and 162 a.u. for the 2 and 3 mm slits respectively) coresponds to 1 mm. Adjusting the potentiometer settings by 45 a.u. thus means that the beam has moved over a distance of 1 mm.

If the current on both sample holder and Faraday cup remains approximately constant when the potentiometer settings are adjusted, the beam must be within the boundaries of the slit. Hence the beam width w_b follows from: $w_b=w_s-d$, where w_s is the width of the slit and d is the distance over which the beam can be moved without changing the current measurements. We find a beam width of 1.7±0.4 mm, which is in good agreement with the beamspot size that is typically obtained in the previously described measurements of the blackened spot area.

Appendix 2: Beam current measurements

All beam current measurements were performed using the Faraday cup in the RBS/ERDA/CERDA-TOF setup (see paragraph 4.2.2), which is depicted schematically in figure A2.1.

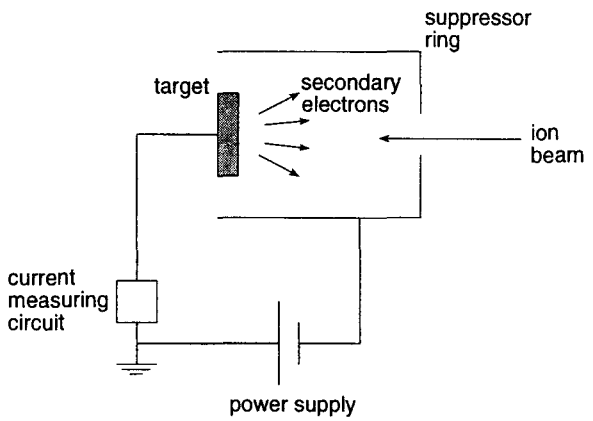

Figure A2.1: *schematic representation of the Faraday cup.*

Numerous low energy secondary electrons are emitted when the ion beam strikes the Faraday cup's target. A negatively charged metal cylinder (suppressor ring) surrounds the target to prevent the escape of these secondary electrons from the Faraday cup, which would result in an overestimation of the true beam current.
The effect of varying the applied suppressor voltage on the current measurements was investigated systematically. Raising the potential on the suppressor ring from 0 to about 20 V resulted in a dramatic decrease of the measured beam current from 90 to 55 nA (≈60% !). Increasing the voltage further had no effect on the current measurements. Moreover, disconnecting the power supply led to a similar decrease in the measured current. From this observations we conclude that an electrically isolated suppressor ring suffices to confine secondary electrons to the Faraday cup, due to the build-up of negative charge on the ring. Connecting the power supply with zero output voltage (or turned off) enables emitted secondary electrons to leak away to earth, due to the finite electrical resistance of the power supply unit.

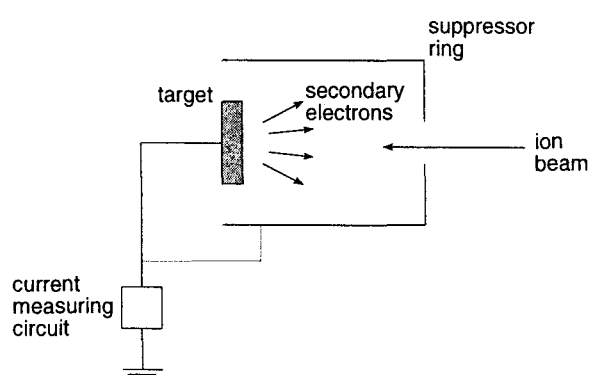

Figure A2.2: *Faraday cup configuration in which the current on both the target and the suppressor ring are measured.*

As an extra check, current measurements were performed using the configuration shown in figure A2.2. Measuring the total current on both target and suppressor ring led to a similar result as obtained in measurements performed with an isolated ring.
Two analog meters A and B are used to read the beam current, the measuring range of these meters can be adjusted to 50, 167 and 500 nA (1:3⅓:10) full scale. The consistency of the indicated beam current when measuring in different full scale modes was checked. A power supply was connected to the measuring circuit, by means of which an adjustable current could be applied. Measuring the current in the various full scale modes at different values of the applied current resulted in figures A2.3 and A2.4.

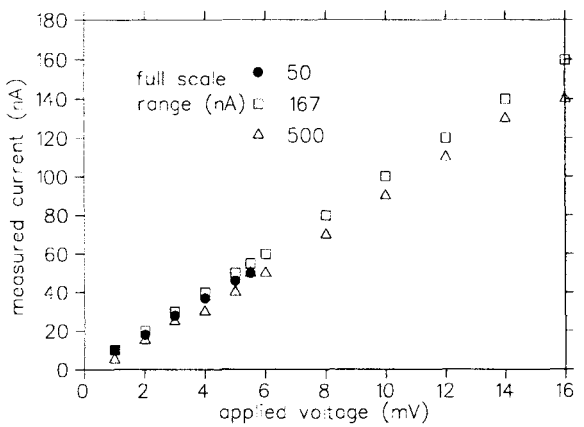

Figure A2.3: *current measurements in the various full scale modes of meter A.*

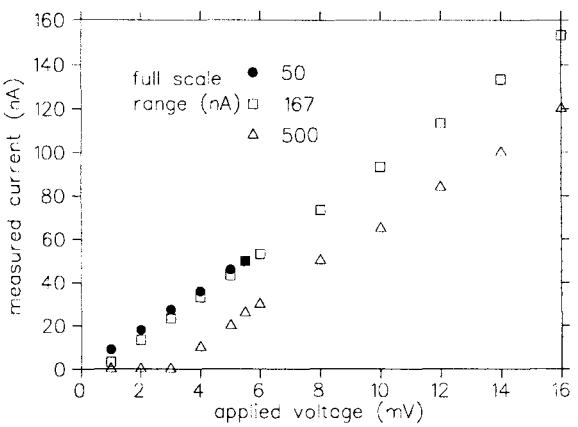

Figure A2.4: *current measurements in the various full scale modes of meter B.*

Current measurements in 50 and 167 nA full scale modes agree within approximately 10% for both meters in the range 30-50 nA. For meter A, measuring in 500 nA full scale mode results in a slightly lower (≈10%) indicated current whereas for meter B this mode suffers from a rather large negative offset (≈20 nA !).

Appendix 3: Fitting with the hydrogen loss formula

The theoretical hydrogen loss formula (see equations 3.5.14 and 3.5.15) has the form:

$$\rho(\varphi) = \frac{1}{V + a + (1 - V - a)e^{-b\varphi}} \qquad \rho V > 1 \tag{A3.1}$$

$$\rho(\varphi) = \frac{1}{ab\varphi + V - a\ln\left(\frac{V + a - 1}{a}\right)} \qquad \rho V \leq 1 \tag{A3.2}$$

where $a=k_1/k_2$, $b=\xi^2 A$ and $\rho(0)=1$ (normalization of the hydrogen density). Fitting with this formula is not straightforward: A3.1 is valid for a hydrogen density ρ larger than 1/V (i.e. more than one hydrogen atom in the combination volume V), whereas when $\rho \leq 1/V$ A3.2 applies. The condition $\rho > 1/V$ corresponds to a fluence region given by $\varphi < 1/b*\ln((V+a-1)/a)$, so the fluence for which A3.1 transforms to A3.2 depends on the fit parameters a, b and V.
The simplest solution to the problem would be to construct a function $f(\varphi)$ that is equal to 0 when $\varphi < 1/b*\ln((V+a-1)/a)$ and 1 otherwise. This function can then be used as an "on/off switch" for A3.1 and A3.2 respectively.
First, the fluence φ is normalized by division by its final value: $\varphi_n = \varphi/\varphi_{final}$. A function $f(\varphi_n)$ that fulfills the above described conditions is then given by:

$$f(\varphi_n) = \mathrm{int}\left(1 + \varphi_n - \frac{1}{b}\ln\left(\frac{V + a - 1}{a}\right)\right) = 0 \qquad \varphi_n < \frac{1}{b}\ln\left(\frac{V + a - 1}{a}\right)$$

(A3.2)

$$f(\varphi_n) = \mathrm{int}\left(1 + \varphi_n - \frac{1}{b}\ln\left(\frac{V + a - 1}{a}\right)\right) = 1 \qquad \varphi_n \geq \frac{1}{b}\ln\left(\frac{V + a - 1}{a}\right)$$

We can now fit the data using the expression:

$$g(\varphi_n) = \frac{1 - f(\varphi_n)}{V + a + (1 - V - a)e^{-b\varphi_n}} + \frac{f(\varphi_n)}{ab\varphi_n + V - a\ln\left(\frac{V + a - 1}{a}\right)} \tag{A3.3}$$